NUMERICAL SIMULATION OF WIND MICROCLIMATE AND AIR QUALITY IN URBAN ENVIRONMENTS WITH VEGETATION

A DISSERTATION SUBMITTED TO THE UNIVERSITY OF MANCHESTER
FOR THE DEGREE OF DOCTOR OF PHILOSOPHY
IN THE FACULTY OF SCIENCE AND ENGINEERING

2022

AZIN HOSSEINZADEH

Department of Mechanical, Aerospace and Civil Engineering

Contents

List of Tables

List of Figures

Abstract

A rapid increase in urbanisation and rising populations living in urban areas lead to major problems including increased rate of air pollution and global warming. Assessing the impact of buildings on wind flow, air temperature and pollution dispersion on people at the pedestrian level in the urban design is therefore of crucial importance. In this study, Computational Fluid Dynamics (CFD) simulations are carried out for a case study, representing the East Village in the London Olympic park. Simulations are conducted by the commercial software, STARCCM+ under steady state conditions with the Reynolds Average Navier-Stokes (RANS) method. Following the determination of areas of high velocity, appropriate tree planting is proposed to overcome the effect of corner and downwash acceleration. Afterwards, improving the thermal environment and air quality is evaluated using different forms of urban vegetation including green roofs, green walls and trees. Thermal simulations using CFD are carried out for a selected area of the East Village. This study indicates that adding a building increases air temperature, pollution concentration, and velocity at the pedestrian level. A parametric analysis is conducted to assess the impact of various key parameters on air temperature, pollution, and velocity at the pedestrian level. These variables include wind speed which ranges from 4-8 m/s at a reference height of 10m, and vegetation cooling intensity which varies from 250-500 W m^{-3}. Three scenarios are tested in which the streets have no bottom heating, 2 °C bottom heating, and 10 °C bottom heating. Pollution is simulated as a form of passive scalar with an emission rate of 100 ppb s^{-1}, considering NO_2 as the pollutant. In all cases, vegetation is found to reduce air velocity and temperature, however, the presence of vegetation in various forms alter the pattern of pollution dispersion differently. More specifically, the results indicate that planting trees close to the edge of buildings can decrease the air temperature by up to 2-3 °C at the pedestrian level. Increasing the cooling intensity of the vegetation from 250 to 500 W m^{-3} results in significantly lower air temperature. In addition, lower wind speeds result in increased pollution concentrations at the pedestrian level. Furthermore, it was found that combining green walls and trees is the most effective strategy to improve thermal environment and air quality. The results of this thesis provide useful clues for the design of green solutions for improving air quality, outdoor pedestrian comfort, and thermal environment.

Declaration

No portion of the work referred to in this dissertation has been submitted in support of an application for another degree or qualification of this or any other university or other institute of learning.

Copyright

and/or Reproductions described in it may take place is available in the University IP Policy (see http://documents.manchester.ac.uk/DocuInfo.aspx?DocID=24420), in any relevant Thesis restriction declarations deposited in the University Library, The University Library's regulations (see http://www.library.manchester.ac.uk/about/regulations/) and in The University's policy on presentation of Theses

Acknowledgements

I would like to express my sincere gratitude to my supervisors, Dr. Amir Keshmiri and Dr. Andrea Bottacin-Busolin for their encouragement, patience and guidance. This journey would not have been possible if it was not for their continuous support, critical reviews, constructive feedback, immense knowledge and constant motivation.

I would like to thank my parents for their endless love, support and encouragement during my PhD and my life in general.

I am also very grateful to my friends in the department of Mechanical, Aerospace and Civil Engineering. It was great sharing the study area and happy moments to all of you during my PhD.

Finally, I would like to thank the rest of my thesis committee for their insightful comments and encouragement and for the hard question which encouraged me to widen my research from various perspectives.

Nomenclature

a	Leaf area density, m^2m^{-3}
A	Constant in urban heat island intensity for North America and Europe: 2.96 and 2.06
b_0	Input parameter for tree model
b_1	Input parameter for tree model
b_2	Input parameter for tree model
b_3	Input parameter for tree model
B	Constant in urban heat island intensity for North America and Europe: 6.41 and 4.01
c_0	Input parameter for tree model
c_1	Input parameter for tree model
c_2	Input parameter for tree model
c_p	Specific heat capacity
$c_{\varepsilon 4}$	Input parameter for turbulent dissipation energy source term
$c_{\varepsilon 5}$	Input parameter for turbulent dissipation energy source term
C_1	Constant parameter for k-ε model
C_2	Constant parameter for k-ε model
C_D	Drag coefficient
$C\mu$	Constant parameter for k-ε model
E	Constant parameter in wall function for rough surfaces
$\overline{f}$	Filtered quantity
g	Gravitational acceleration, ms^{-2}
$\overline{G}$	Filter function
H	Height of building, m
k	von Karman constant
K	Turbulent kinetic energy, m^2s^{-2}
$\dot{m}$	Mass flow rate, kg s^{-1}

r	Roughness height, m
$\widetilde{p}$	Filtered pressure, kg m^{-1} s^{-2}
p	Pressure field, kg m^{-1} s^{-2}
P	Mean pressure field, kg m^{-1} s^{-2}
Po	Population in urban heat island intensity formulation
P_c	Cooling power, W m^{-2}
P_k	Turbulent production term, W m^{-2}
P_ω	Turbulent production term, W m^{-2}
q_{cond}	Conductive heat transfer, W m^{-2}
q_{conv}	Convective heat transfer, W m^{-2}
q_{rad}	Radiative heat transfer, W m^{-2}
Q_E	Latent heat heat, W m^{-2}
Q_F	Anthropogenic heat, W m^{-2}
Q_H	Sensible heat, W m^{-2}
Q^*	NEt all-wave radiation, W m^{-2}
r	Constant parameter in wall function for rough surfaces
R_{ij}	Reynolds stress tensor
S	Strain tensor
Sc_t	Turbulent Schmidt number
S_ϕ	Pollutant source term, kg m^{-3} s^{-1}
τ_{ij}	Residual stress tensor
T_{sext}	Temperature in the outer surface of buildings, K
T_{sin}	Temperature in the inner surface of buildings, K
T_∞	Ambient temperature, K
$\|u\|$	Velocity magnitude, ms^{-1}
u_0	Reference velocity at height 2 and 10 m, ms^{-1}
$\widetilde{u}$	Filtered velocity, ms^{-1}
u^*	Friction free velocity, ms^{-1}
$u^{'}$	Mean (Fluctuating velocity), ms^{-1}

$\overline{u}$ Mean (time-averaged velocity), ms^{-1}

W Width of building, m

y The normal distance from the wall to the centroid of the wall cell, m

y_p The normal distance from the wall to the centroid of the wall cell, m

Y^+ The prism layer's initial height

z_0 Aerodynamic roughness length, m

Greek Symbols

β Input parameter for tree model

β_d Input parameter for turbulent kinetic energy source term

β_p Input parameter for turbulent kinetic energy source term

β_{pt} Input parameter for tree model

γ Input parameter for tree model

γ_{pt} Input parameter for tree model

ΔQA Heat storage, Wm^{-2}

ΔQs Heat advection, Wm^{-2}

ε Turbulent dissipation energy, m^2s^{-3}

μ_t Turbulent viscosity, $kgms^{-1}$

ν kinematic viscosity, m_2s^{-1}

ρ Density, kgm^{-3}

σ Molecular Schmidt number

σ_k Model coefficient for k-ε model

σ_ω Model coeffcient for k-ω model

τ_w Wall shear stress, kgm^{-2}

Φ Passive scalar

ω Turbulent dissipation rate, m^2s^{-3}

Subscripts

i,j Scalar node position

Acronyms

ANN	Artificial neural network
BHD	Breast height diameter, m
CFD	Computational fluid dynamics
DNS	Direct numerical simulation
HG	Height growth
LAD	Lef area density
LES	Large eddy simulation
LRNM	Low Reynolds number modelling
RNG	Renormalisation group
RANS	Reynolds-averaged Navier-Stokes
Re	Reynolds
SGS	Subgrid scale
SST	Shear stress transport
SW	South west
UHI	Urban heat island
WRF	Weather research forecast

Chapter 1

Introduction

1.1 Background

The majority of the world's population currently lives in cities, and the trend toward urbanisation continues to grow year after year. An increase in the number of people living in urban areas causes severe issues such as pedestrian discomfort as a result of high-rise building constructions, global warming, urban heat islands (UHI) due to a lack of greenery, and pollution, particularly of water, air, and noise, due to the high welfare of big cities [1, 2]. These are unavoidable changes, so steps must be taken to eliminate or at least lessen their consequences for the sake of people's comfort. Three significant topics are discussed in the following sections, which are the study's main focus.

1.1.1 Wind assessment and pedestrian discomfort

Evaluating wind flows around buildings is part of the planning application during the design of new developments. Determination of wind flow pattern and wind speed at the pedestrian level are conducted for pedestrian comfort to create a relaxing environment for human beings. Wind microclimate assessment refers to combining the local wind data with various techniques (e.g. CFD in this study) to predict the wind speeds at the pedestrian level and assess the comfort based on the Lawson comfort scale [3, 4]. Following the determination of high velocity

areas which cause pedestrian discomfort, mitigation techniques are introduced to decrease the wind speed. Various techniques have been used so far and planting vegetation is one that is investigated in this study.

1.1.2 Urban Heat island effect (UHI)

The term "urban heat island" refers to a situation in which the temperature in a city is much higher than in nearby rural areas. The first UHI study was carried out in 1800 by Yong et al. [5]. The figure below depicts the usual profile of urban heat island.

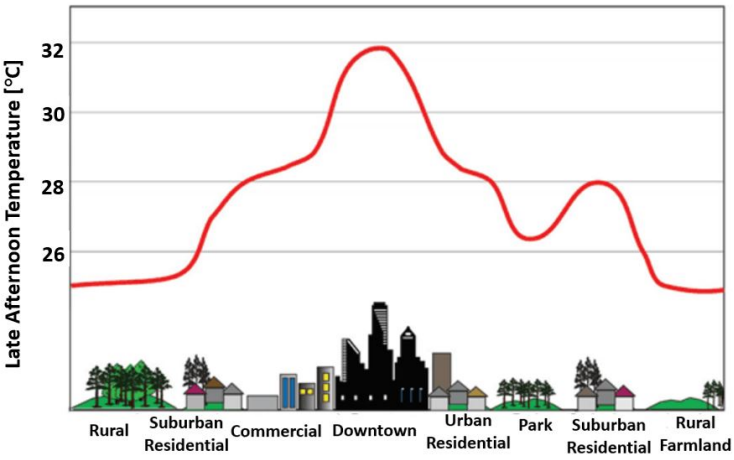

Figure 1.1: Typical profiles of UHI. Image Adapted from [6].

According to Oke et al. [7], urban heat islands can raise city temperatures by 2 to 8 ºC. According to a 2013 study by Mohajerani et al. [8], the temperature rise will be between 5 and 15 ºC. A survey conducted by Grimmond et al. [9] has shown that, by 2030, 61% of the world's population would be living in cities. This suggests that UHI will become more intense as a result of deforestation and global warming. Appropriate actions must therefore be taken ahead of time to prevent these issues.

Many factors contribute to these phenomena, including a lack of vegetation in cities, increased anthropogenic heat, and the use of dark, low-albedo construction materials. This phenomena

has a negative impact on people's health, leading to an increase in morbidity and mortality. The vast bulk of research in this area has been done to explain the phenomena, the methodology for evaluating UHI (e.g. experimental, numerical works), and the mitigation strategies that have been examined so far. The following chapter will go through these issues in greater depth.

1.1.3 Urban air pollution

One of the most critical environmental issues affecting urban environments is air pollution. Pollution comes from a variety of sources, including cars, houses and industry. There are two types of air pollutants: primary air pollutants and secondary air pollutants. Nitrogen oxides (NO_x), volatile organic compounds (VOCs) and carbon monoxide (CO) are the most common primary air pollutants discharged directly into the atmosphere from emission sources [10]. In urban areas, road transport is the primary source of NO_x. The majority of NO_x generated by cars is in the form of nitric oxide (NO), with a little amount of nitrogen dioxide (NO_2) [11]. NO_2 in excessive concentration can have negative consequences for human health, such as cardiovascular disease, lung problems, respiratory symptoms, and allergies. High levels of NO_x may have negative effects on plants and habitats leading to loss of biodiversity [12].
To protect human health, air quality standards and guidelines have been established. The air quality limit and objective values that must be fulfilled by the UK National Air Quality Objectives can be found by department for environment food & rural affairs in Ref. [13].

1.2 Study objectives

The major goal of this thesis is to provide methods for improving pedestrian comfort in urban environments while minimizing UHI and pollution. Human health, air quality, and temperature are all affected by dense populations in urban regions with high-rise structures. Buildings in metropolitan areas obstruct the atmospheric flow and create high-velocity areas which is uncomfortable for pedestrians. As a result, steps must be taken to address the challenges and build pedestrian-friendly residential zones. One of the strategies considered in this study that

can lead to pedestrian comfort is planting greenery in various types. In addition to reducing wind speed through vegetation, which modifies the flow pattern and speed, the impact of greenery on air temperature and pollution at the pedestrian level must be assessed. To do so, a case study was developed that represents the East Village in the London Olympic Park and depicts a small part of the urban environment. This case study is subjected to CFD simulations. The results consist of pedestrian velocity contours, which are followed by a new configuration with the addition of trees. In each high-velocity zone, different tree configurations are planted, and the optimal layout is chosen based on the reduction in wind speed magnitude. In addition to the wind speed reduction, the impact of various forms of vegetation (e.g. green roofs, green walls and trees) on air temperature and pollution are evaluated. For this part, the selected areas of East Village is taken as a case study. The finding demonstrates how constructing a high-rise building in the direction of the wind speed can increase UHI and degrade air quality. It also shows how vegetation can help to mitigate the negative effects of high-rise structures. The favourable effects of various vegetation scenarios are confirmed by contours of air temperature, pollution concentration, and velocity at the pedestrian level. The contours indicate the magnitude of the reduction of air temperature, pollution and velocity as well as the radius of the reductions to the buildings.

This study demonstrates a step-by-step approach to environmental design. This work contains implications for the prediction of wind speed at the pedestrian level, practical guidance for urban designers to achieve pedestrian comfort as well as sustainable cities with lower pollution and temperature. Incorporating the present findings at the design stage of large developments will allow engineers to create environmentally sustainable buildings, providing direct social benefits to the local communities.

1.3 Outline of thesis

This thesis consists of 7 chapters. In chapter 1, the main aim of this project and the summary of this work are explained. Chapter 2 of this work provides a comprehensive review of the

UHI effect, pollution dispersion in urban environment and wind microclimate assessment. Details are given about the causes and effect of UHI on the environment, existing approaches for determining UHI, methods of abatement for pollution dispersion and wind speed mitigation strategies. In chapter 3, the mathematical modelling models used to represent the thermal environment with pollution are classified into four sections: Turbulence, heat transfer, vegetation and modelling of the pollution. The applicability of various turbulence models in urban design, different modes of heat transfer available to model the thermal environment, and the simplified method that was used in this study, as well as the required equations in case of adding vegetations in urban design, are discussed in this section. Furthermore, the model used for pollutant dispersion is thoroughly described. Chapter 4 deals with the numerical procedure in more detail. Two case studies are introduced in this chapter. Test case 2 is the main case study, representing the East Village in London Olympic park which is followed by a validation test (Test case 1) against an experimental data for a simpler urban configuration. Each test case includes the information regarding the geometry, mesh, governing equations and the boundary conditions. The evaluation of wind speed at the pedestrian level is the subject of Chapter 5. Following the determination of high-velocity zones for Test case 2 in section 4.3.1, the use of vegetation to reduce wind speed is proposed. In this chapter, Test case 3 is essentially Test case 2 with vegetation. This section contains a variety of tree arrangements. The mitigation of wind speed for various designs has been compared. Chapter 6 which investigates the effect of vegetation in different forms (e.g. green roof, green walls and trees) on air temperature and pollution at the pedestrian level. This chapter includes 4 test cases that are numbered from 4 to 7. Test case 4 and Test case 5 are the validation case studies. Test case 4, consists of several street canyons to validate the effect of heat (namely bottom heating) on the air temperature in the targeted street canyon. Test case 5 consists of 2 buildings and is validated against a numerical work to see the effect of pollution dispersion. Test case 6 is the selected area of East village which includes 7 buildings and the Test case 7 is the extension of Test case 6 with one building more. The differences between Test Cases 6 and 7 show how adding a building affects velocity, air temperature, and air quality. Test case 7 incorporates several types of vegetation

under various conditions, and their impact on air quality, temperature, and wind speed has been evaluated. The impact of wind speed, vegetation cooling intensity, and bottom heating on greenery effectiveness in terms of velocity, air temperature, and pollution concentration was analysed. Concluding remarks and recommendations for future work are included in the last chapter. Figure 1.2 depicts the Beyer building at the University of Manchester as an example of a sustainable architecture with green walls and trees surrounding it, which is this study's main focus.

Figure 1.2: Beyer building: an example of sustainable building [14].

Chapter 2

Literature review

2.1 Preliminary remark

In this chapter, the outline of the key analysis of UHI, pollution dispersion and wind microclimate assessment is explained. This includes the main causes of UHI as well as its impact on human's health. In the following section, the main studies to determine UHI intensity are described. Thereafter, the main mitigation methods are identified. Afterwards, Pollution dispersion analysis in urban environments is evaluated and followed by suggesting methods of pollution reduction in urban areas. In the last section of this chapter, wind microclimate assessment is discussed which is an essential step for pedestrian comfort in an urban areas.

2.2 The causes and impact of urban heat island effect on the environment

As a result of local and global climate change, ambient temperatures are rising by several degrees, with significant implications for energy use, health, and the economy. Increased urban air temperatures have a wide range of impacts for people's lives, including the following:

- Significant decline in city air quality. Increased urban temperature values contribute

to higher levels of primary and secondary regional pollutants, such as nitrogen oxides (NO_x) and ozone (O_3) as reported by Sarrat et al [15]. Furthermore, high wind speeds can trap pollutants inside cities, providing a health risk to residents. [16].

- Detrimental effect on people's health and well-being which increases the rate of death and mortality significantly.
- The lack of indoor and outdoor thermal comfort: Numerous studies have linked an increase in ambient urban temperature to a decrease in pedestrians' summer outdoor thermal comfort [17, 18]
- Raising the cooling and heating requirements of the building where the cooling and heating load is determined by the intensity of urban warming and the number of buildings in the area.[19–21]

The causes of UHI are divided into several groups. Urbanisation and the construction of high-rise buildings, which store more heat during the day and release it at night, are the main and primary drivers of UHI. In addition, a lack of vegetation and deforestation as a result of human activities, as well as the use of land for building construction contribute to the rise in city temperatures. Moreover, pavements and roofs with low albedo, anthropogenic activities (e.g. traffic, industry) aggravate the UHI effect [8] . Possible causes of UHI have been shown schematically in Figure 2.1.

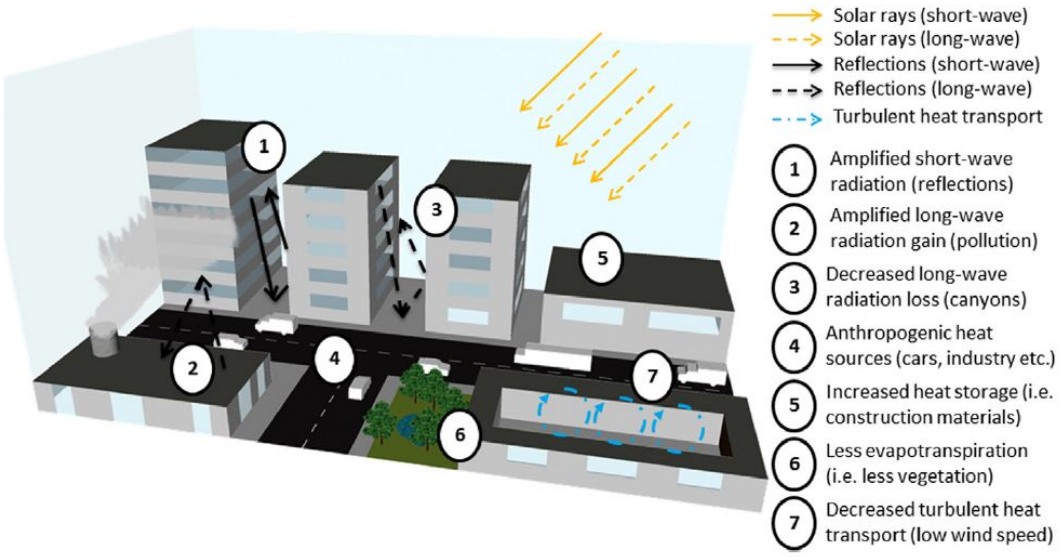

Figure 2.1: Illustration of possible causes of UHI. Image taken from [22].

2.3 Approaches for urban heat island evaluation

The vast majority of work has been done to combat UHI. Urban materials, urban geometry, air pollution, and anthropogenic heat, which is released by humans (e.g. traffic, industry), are the key characteristics of the urban region that distinguish it from its surrounding and rural surroundings.

The intensity of the urban heat island is influenced by a variety of factors [23]. Climate features, surface morphology, proximity to water, proximity to industrial site, urbanisation, vegetation ratio in area, land use, street canyon structure, building density, heating and cooling energy consumption, traffic, and air pollution are all aspects to consider.

The majority of the UHI investigations were done as part of a case study, and some of them were validated locally. However, they all show a similar pattern, indicating that both urban and rural temperatures are rising.

At different times of the day, the intensity of UHI varies. The effects of UHI are amplified

at night can however, be seen during the day. During the night, the building's stored heat is released. In addition, There are a few days each year when the temperature is much higher than other days, referred to as a heat wave, during which UHI is exacerbated in this period [24]. According to Meehi and Tebaldi [25], the urban region will be subjected to more heat waves in the future, with the intensity of these waves increasing as a result of global warming. This issue is exacerbated in regions where UHI is already present.

There are several ways to model UHI. Observational and numerical methods are the two technical solutions. Computational fluid dynamics (CFD) and urban canopy modelling (UCM) are two approaches to numerical analysis. The next sections discuss these strategies in further depth.

2.3.1 Observational techniques

Observational techniques refers to the techniques which are conducted through measurements including field measurement, thermal remote sensing such as using satellite imagery or small-scale physical modelling such as wind tunnel testing [26]. Measurements can be used to forecast UHI intensity by estimating thermal and airflow parameters [27]. The temporal and spatial variance of UHI can be assessed using these methods. Stochastic techniques such as regression modelling and neural network modelling can be used to represent data obtained through field measurement.

Due to UHI, temperature in urban areas can fluctuate dramatically in different places. Regardless of this heterogeneity, there is a simplified model in the literature that indicates the relationship between UHI intensity and population, sky view factor, building aspect ratio, and other factors. These models are used traditionally to estimate the UHI intensity. For instance, Oke et al. [28] in the year 1973 developed a model that shows the relation of maximum temperature to population. This relation is shown in Equation 2.1.

$$\Delta T_{(u-r)max} = AlogPo - B \tag{2.1}$$

where *Po* stands for population for ideal calm and clear conditions. In North America and Europe, the constants *A* and *B* in the equation above differ. To derive the equation above, Oke measured the temperature with a thermistor probe mounted on one side of a car . Finally, this equation was developed using regression modelling. Oke et al. [29] established another model that shows the relationship between UHI intensity and the aspect ratio of buildings in his other research. Equation 2.2 demonstrates this relationship.

$$\Delta T_{(u-r)max} = 7.45 + 3.97 + ln\frac{H}{W} \tag{2.2}$$

Another equation that describes the relationship between UHI intensity and sky view factor is as follows:

$$\Delta T_{(u-r)max} = 15.27 - 13.88\psi_S \tag{2.3}$$

The sky view factor is denoted by ψ_S . Building height and width are represented by H and W, respectively.

These types of models, as described above, are for the entire city, and one value cannot be used to accurately assess the urban heat island for a single area. Artificial Neural Networks (ANN) is another method of predicting UHI in this area . In this approach, different elements that cause UHI will be used as inputs, and the air temperature will be evaluated using different neural network designs. Based on the work of Gabokis et al. [30], time, ambient temperature, global solar radiation were regarded as an input to the model and these variables were utilised to train and evaluate different topologies of neural network. The input data for developing such a model comes from the measurement. The ambient temperature is monitored at numerous experimental sites, whereas global sun radiation is measured at the national observatory in this study. There are several types of neural network structures, including feed forward, Elman, and cascade neural networks. According to the findings of the study mentioned above, the intensity of the urban heat island can be anticipated for a 24-hour period. This calculation is useful for forecasting energy use during heat waves. In this context, another work conducted by Sherafati et al. [31] shows a use of spatial variables such as: neighborhood development, distance to

nearest road, digital elevation model, slope and aspect to anticipate the surface temperature.

Aside from these methods, wind tunnel testing can be used to assess airflow and temperature around buildings. To apply this strategy, a scaled model of the genuine situation needs to be created. The wind tunnel test conditions must resemble the actual site circumstances in an urban region. This can be accomplished by employing the similarity law. Validation of numerical simulation results is frequently done in a wind tunnel [26].

Following the introduction of the numerical system, the next section compares experimental and numerical approaches.

2.3.2 Computational Fluid Dynamics(CFD)

With the advancement of computer capabilities in recent years, numerical simulation approaches have received a lot of attention and are now widely employed at various scales. Nowadays, computational fluid dynamics (CFD) is widely used as a numerical technique in a variety of domains. CFD can resolve airflow, heat transfer, and their interactions with buildings and other impediments in order to describe the thermal environment. The equations describing fluid flow can be solved using CFD are: mass, energy, and momentum conservation [32].

The two scales of CFD analysis for the urban environment are meso-scale and micro-scale. The mesoscale CFD analysis is valid for heights of 200 m to 2 km. These models are utilised for parts of the planetary boundary layer, and they treat the urban area as a roughness layer, whereas CFD at the microscale stays inside the surface layer. These layers, as well as various scales, are depicted schematically in Figure 2.2 and 2.3.

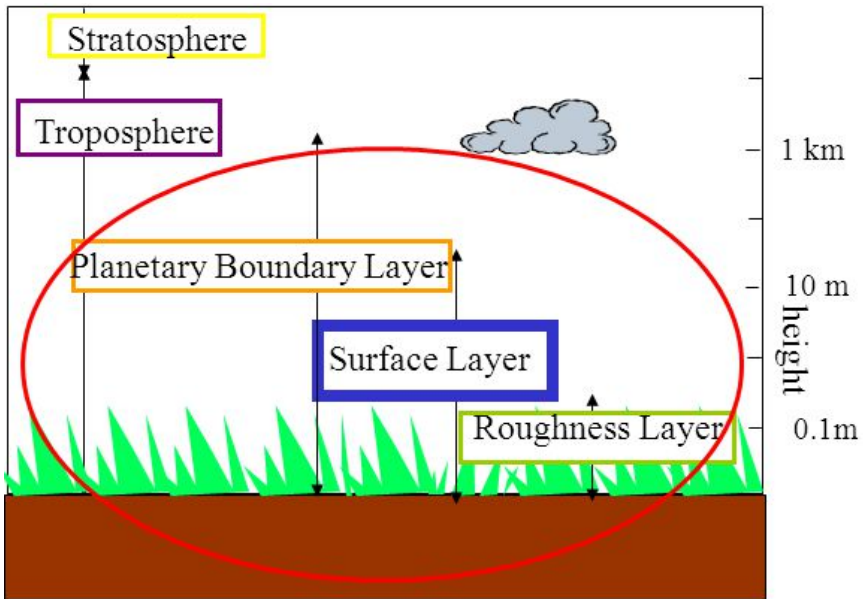

Figure 2.2: Atmospheric boundary layer. Image taken from [33].

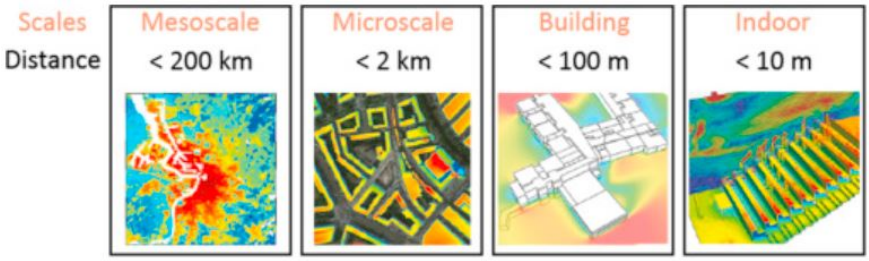

Figure 2.3: Representation of various scales in urban climate modelling. Image taken from [32].

There are some advantages and disadvantages of using CFD for thermal environment studies. It should be noted that with measurement, all places in space cannot be measured, and it depends on where the sensor is positioned, according to the observational techniques described in section 2.3.1. Besides, all points and variables in defined computational domains will be evaluated using numerical simulation, whether CFD or UCM is used. (see section 2.3.3). At the same time, all variables such as velocity, pressure, and temperature will be determined. Furthermore, the measurement method is limited to a small area. Sensors are generally expensive, and have

limited number of points in space, therefore, it is not possible to estimate future airflow or temperature using experimental methods, but it is possible using numerical approaches [34].

2.3.3 Urban canopy modelling (UCM)

The urban canopy layer (UCL) is a layer that exists between the ground and the average height of buildings and trees. Energy and mass exchange between specific surfaces and canyon air determine its properties [35, 36]. Various computational models have been designed to examine the energy exchange above cities, as well as the transfer of momentum and moisture between the UCL and the overlying atmosphere. These models considers the effects of urban building typology when computing the surface energy balance.

In the urban canopy model, CFD is separated from the energy balance modelling. In this numerical method, energy balance equations are derived for a control volume which contains at least two adjacent buildings. The model assumes the energy exchanges between surfaces and the surrounding air is in urban canopy as it has been illustrated in Figure 2.4. This model predicts air temperature, building surface temperatures, pavement temperatures, and street temperatures. Airflow is an external input to the model that is decoupled from CFD. WRF (Weather Research and Forecast), a mesoscale weather prediction model, can be combined with UCM. This approach has been used in a variety of studies, including [36–40].

When comparing UCM to CFD, it is evident that CFD is capable of evaluating both flow and heat transfer using an explicit mechanism for velocity and temperature coupling. However, if a more detailed building simulation is necessary, CFD can be combined with building energy simulation. In addition, this method can be used to assess humidity and pollution, whilst UCM does not assess flow analysis in the vicinity of buildings [32, 41]. Furthermore, CFD analysis may be used to analyse scales ranging from mesoscale to building and relatively smaller scales such as human scale. Aside from the benefits of CFD over UCM and observational approaches, there are several disadvantages to implementing it. One of the disadvantages of employing CFD is the requirement for high resolution urban geometry, as well as adequate boundary constraints

imposed on the calculation domain, such as velocity input or pressure outlet. To summarise, CFD analysis is incorporated in this work while comparing different approaches because flow analysis around buildings is important. In the following chapters, the numerical technique and governing equations will be discussed in greater depth.

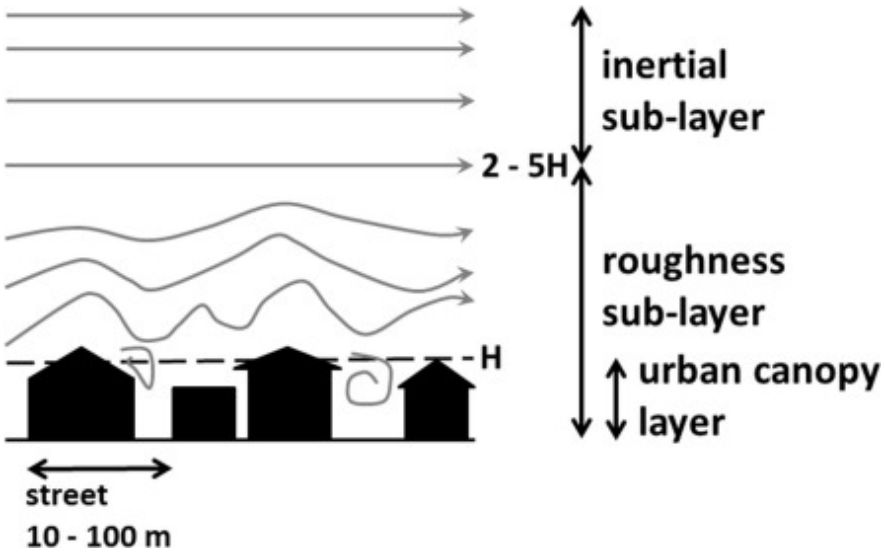

Figure 2.4: Schematic diagram of urban canopy layer. Image taken from [41].

2.4 Approaches for mitigating urban heat island effect

2.4.1 Introduction

Advanced urban mitigation techniques help to reduce ambient temperatures and mitigate urban heat islands. UHI is an unavoidable consequence of rising population and urbanisation. As a result, major steps must be taken to address this problem and lessen its impact. Many studies have been conducted on various mitigating measures. The effectiveness of these strategies is determined by the weather and the geometry of the urban area. The following are the most prevalent methodologies that have been used. The measurement steps based on the most recent review in 2017 are schematically shown in Figure 2.5. The next sections will go over some of the most frequent measurements in further depth including:

- Planting and vegetation
- Green roof and cool roof
- Vertical greenery
- Cooling pavements
- Water mitigation methods
- Improving in building design
- Roof pond
- Anthropogenic heat reduction
- Proper ventilation of the buildings

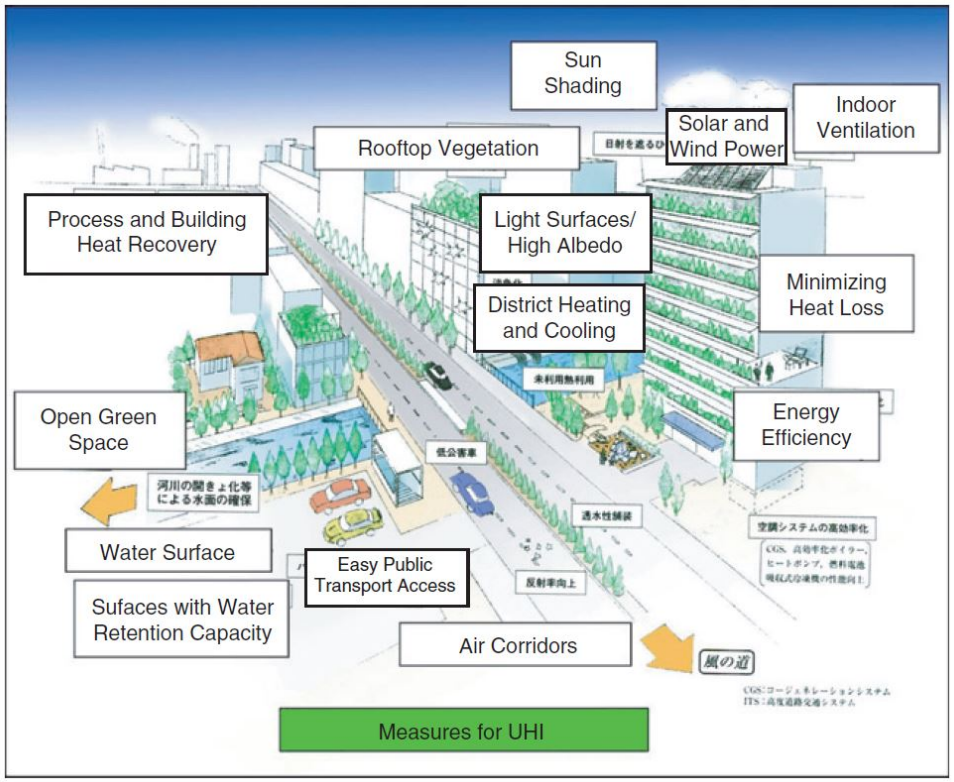

Figure 2.5: Illustration of mitigation strategies. Image taken from [42].

2.4.2 Planting and vegetation

Urban vegetation is the most widely used UHI mitigation strategy among the UHI mitigation approaches, which can take the shape of trees and hedges, green roofs, grass, or a combination of these [43]. According to Santamouris' review report [44], urban trees have the greatest potential for mitigation, followed by grass and green roofs.

Increasing the portion of green spaces can help to mitigate the rising temperature trend by providing a cooling effect. This procedure has been tested for a long time [45]. Urban green spaces can either be part of the city landscape in the form of parks, trees, grass or can be incorporated onto the outer surface of buildings as green roofs or vertical green façades [44].

According to a mobile survey conducted by Wong and Yu [46] in Singapore to assess the influence of green areas in tropical cities, there is a direct link between temperature reductions and the appearance of green areas in cities. Temperatures for various land uses (e.g., industrial, residential, forest, and airport) were measured in this study. The thermal and airflow conditions were calculated based on the size of the green space, the vegetation species, the sky view factor, and the density of urban texture. According to their study, the maximum temperature difference between urban and rural areas in Singapore was 4.01 °C. In addition, the mapping of temperature has shown a clear variation of temperature in green areas which confirms the cooling effect of vegetation to diminish the UHI effect.

CFD modelling, in addition to observational methodologies, can analyse vegetation in UHI intensity. In Chapter 3, the main governing equations of this method are explained. The vast majority of microclimate simulation studies that assess the cooling capability of plant techniques focus on the performance of street trees and green roofs, or their combined use [34, 47–49]. The vegetation scenarios under consideration are based on different urban green coverage or green elements with varying plant features, such as height, foliage density, and so on. Dimoudi and Nikolopoulou [50] used numerical modelling to examine the influence of vegetation and

demonstrated the thermal impact of vegetation in Athens. According to this study, vegetation can greatly influence the thermal microclimate in the urban texture which affects the area within the park as well as the surrounding area, particularly at the leeward side of the green area. Shashua [51] examined the impact of different tree species in different urban morphologies. His findings reveal that the cooling effect of trees on the urban microclimate is heavily controlled by urban street geometry; the higher the aspect ratio of the streets, the greater the relevance of shadowing by building volumes, and therefore the lower the cooling effect of trees. As a result, increasing urban green covering and/or leaf area density (LAD) values is not necessarily the optimal strategy for ambient air cooling. According to previous modelling studies [52, 53], extra trees will act as additional obstacles to incoming longwave radiation, wind, and wind movement, as well as increase shadowing. As a result, both longwave radiation loss and heat removal via convection can be significantly inhibited, ultimately resulting in a rise of the ambient air temperature. Wang and Akbari [54] employed ENVI-met (a spatial and temporal resolution micro-climate model) and three tree species with varying crown width, height, and LAD in his research, and found that the greatest daily temperature drop ranged from 2 to 5.1 °C. Wu and Chen [55] also used ENVI-met to investigate the relationship between green coverage ratio (e.g. tree and grass) and air temperature in high-solar-radiation locations. The importance of various tree arrangements was investigated in this study, as well as their cooling effects. Their findings demonstrate how different tree arrangements in urban environments have different effects on sensible heat reduction and air temperature variation. According to their finding, various tree configurations in Beijing with high-rise buildings resulted in a maximum difference of 14.84×108 J/ha in sensible heat reduction among the different scenarios. This study shows that an optimized spatial design of greenspaces can both improve thermal environments and minimize UHI magnitude by reducing air temperature and sensible heat fluxes into the atmosphere.

2.4.3 Green roofs

The roof of any building receives the greatest amount of radiation. As a result, the roof is the most significant portion of the building's surface. A green roof is made up of a waterproofing membrane, a growing medium, and a vegetation layer that covers the roof of a building in various ratios [56]. By planting on the roof, a green roof enhances the rate of Evatranspiration. The energy balance for a thin layer of roof at the roof-air interface is written with Equation 2.4 and 2.5 to fully comprehend the fundamental cause for minimising UHI intensity utilising green roof [57].

$$R_n = SW_{in}(1-\alpha) + LW_{in} - LW_{out} \tag{2.4}$$

$$R_n = H + LE + G \tag{2.5}$$

R_n stands for net radiation, H refers to sensible heat flux, LE is the latent heat flux from soil evaporation and plant transpiration, G refers to the heat flux to the building. Short wave and long wave radiation are denoted by SW and LW respectively and albedo is denoted by α. According to the equations above, a green roof enhances LE while lowering sensible heat for a given net radiation.

CFD approaches play an important role in examining the impact of green roofs on the thermal environment for indoor and outdoor comfort. The impact of a green roof on the indoor environment has been assessed based on Himanshu's work [56] in India. The results show a decrease in heat movement through the roof, as seen by a drop in room temperature. The benefits of utilising a green roof based on this work are shown in the Figure 2.6.

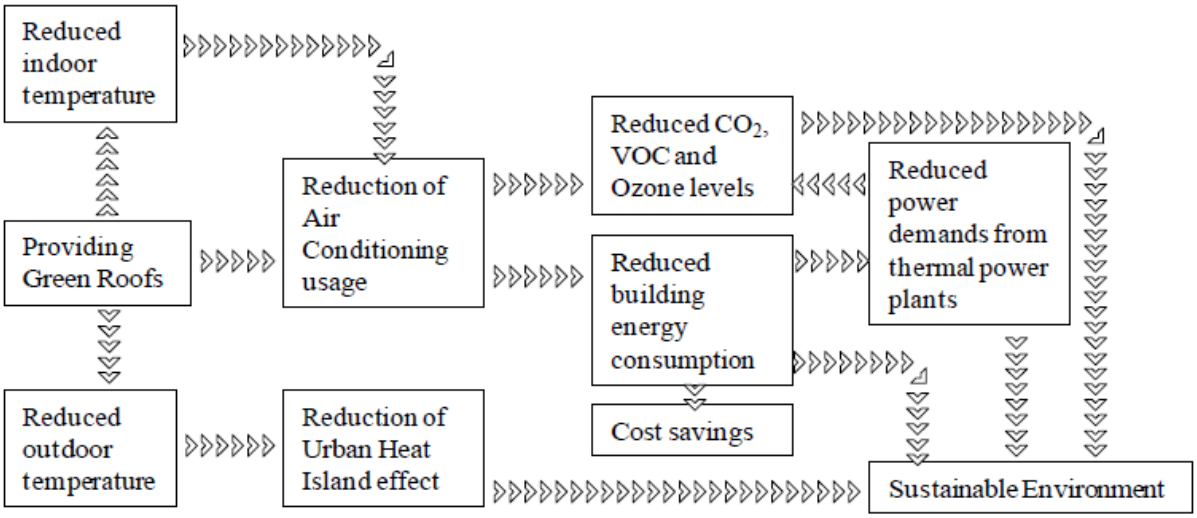

Figure 2.6: Advantages of using green roof. Image taken from [56].

Other studies have looked at the impact of green façades on the surrounding environment for outdoor thermal comfort [58]. Huang et al. [59] found the average drop in ambient air temperature produced by green roofs in Tokyo is 0.3 °C whereas Chen et al. [60] gave an estimate of 0.1 °C. Liu and Baskaran [61] conducted an experimental investigation to determine the effect of a garden roof on air temperature reduction. According to their findings, garden roofs are more effective in reducing heat gain in the summer than heat loss in the winter. Lin et al. [62] investigated the effect of Seven models of different forms of green façades on the thermal environment in their study and validated their model with field measurements. Green façade application strategies and accompanying optimizations for thermal comfort in a hot-humid climate transitional location were the focus of their study. The results of field data show that the green façades reduces average temperature by 2.54 °C and that three typologies among the evaluated cases are more effective in regulating the thermal environment in the summer.

The ability of green roofs to mitigate climate change is found to diminish dramatically as a function of building height [44]. As a result, green roof systems on high-rise buildings have a minor influence on reducing UHI.

In addition to the influence of various varieties of vegetation on UHI, several studies have investigate the effect of combining such methods [63]. Srivanit and Hokao [64] and Sodoudi et al. [53] used numerical models to analyse the combined deployment of green roofs with extra trees in Saga, Japan, and Tehran, Iran, respectively. In both investigations, the obtained simulation results suggested a maximum air temperature reduction in a summer day near 2.30°C. In contrast, Chen and Ng [17] discovered a smaller effect of combining green roofs and trees in an urban area of Hong Kong, China, with a maximum air temperature reduction of 0.45 °C.

The maximum cooling effects of green roofs in various studies are represented in Table 2.1. Some of these investigations are based on numerical simulations, while others are based on measurement data. These studies differ in terms of location, urban morphology, vegetation type, and green roof coverage. The findings indicate that green roofs can reduce average air temperature from 0.5 °C in Germany [65] to 4 °C in Singapore [66].

Table 2.1: Cooling effects of green roofs.

Author	Maximum reduction in average air temperature [°C]	Location
Niachou et al. [67]	2	Loutraki, Greece
Pompeii et al. [68]	1.8	Chicago, USA
Wong et al. [66]	4	Singapore
Wong et al. [66]	0.8	Tokyo, Japan
Wu et al. [69]	1.32	Xingtai, China
Susca et al. [70]	2	New York, USA
Bass et al. [71]	2	Toronto, Canada
Meek et al. [72]	0.9	Melbourne, Australia
Chen et al. [73]	0.5	Melbourne, Australia
Sharma et al. [74]	0.6	Chicago, USA
Zölch et al. [75]	0.5	Munich, Germany
Alcazar et al. [65]	1	Madrid, Spain

2.4.4 Cool roofs

Considerable research has been conducted in the literature to determine the impact of cool roofs on reducing UHI. Research conducted by Li et al. [57] on the effectiveness of cool roofs using UCM has been well documented. According to the Equations 2.4 and 2.5, a cool roof reduces UHI by increasing albedo and decreasing sensible heat. According to previous research, the distinctive and well-designed application of cool materials on building roofs may greatly reduce air temperature above the roof surfaces, but only has a moderate cooling capacity at the pedestrian level [76–79]. Huang et al. [59] used CFD methods to examine the influence of cool roofs on reducing maximum air temperature in Tokyo, which resulted in a 0.4 °C reduction in air temperature. In the work of Georgakis et al. [80] for a case study in

Athens, Greece, this value reaches 1 °C. However, in Zoras' work [81] in Florina, Greece, the maximum temperature reduction is 1.4 °C .

2.4.5 Cooling pavements

Cool materials have been extensively investigated as a means of enhancing the microclimate of urban environments. Cool pavement applications involve the replacement of traditional asphalt and concrete pavements with cool pavements on the ground.

Asphalt concrete is one of the most well-known pavement materials, and its low albedo and high heat capacity contribute significantly to UHI reduction. As a result, one of the options for mitigating UHI is to cool the pavement and use a lighter colour [42]. On the road, replacing dark pavement with reflecting ones will improve solar radiation reflection as well as the emissivity factor. This improvement will result in a decrease in surface temperature [34]. In comparison to asphalt concrete, cool pavement refers to a pavement that is capable of overcoming the maximum surface temperature. Based on the Equation 2.6, this definition is easily understood.

$$T_{smax} = \Gamma \frac{(1-R)I_0}{P\sqrt{\omega}} \tag{2.6}$$

where Γ is the ratio of thermal absorption to thermal conduction, R is the albedo, I_0 refers to solar irradiation, P is the thermal inertia of the pavement and ω is the angular frequency. According to this equation, the maximum surface temperature can be lowered by reducing the ratio of absorption to thermal conduction and increasing the thermal inertia of the pavement. According to a CFD simulation conducted by Santamouris [82] in Athens using non-aged asphalt, the ambient temperature and maximum surface temperature are reduced by 1.5 °C and 11.5 °C respectively and thermal comfort is increased considerably. Other cool material applications can be found in Tsoka's review paper [63].

2.4.6 Water mitigation methods

Pools and ponds are the most common and well-known water mitigation solutions. The ambient temperature is lowered by two independent heat transfer mechanisms: evaporation of the water through the pond surface and convective heat transfer between the ambient environment and the pond [44]. Roof spray cooling is another means of reducing UHI, in addition to putting pools and ponds around the structures. Roof modification is critical since buildings receive the most radiation through their roofs. Roof spray cooling is a method of reducing heat flux through a building's roof by spraying a fine mist of water on the roof surface. This strategy necessitates the use of periodic boundary conditions [83]. Experimental studies was conducted using this concept are outlined n the work of Jain and Rao [84]. The results show that roof spray cooling can successfully lower ceiling and indoor air temperatures.

2.4.7 Improving building design

To reduce UHI intensity, changes to the building design, such as the width-to-height ratio and the sky view factor, can be made. There have been various studies done in this sector to see how changing the building design affects UHI. According to the research of Urano et al. [85], changing the width and height of buildings in combination with drag effects can change the environment near the ground. The findings of this research reveal that the smaller the building width, the lower the building drag. Furthermore, reducing the width of buildings will result in an increase in temperature and a decrease in wind speed. Memon et al. [86] assessed the effect of building aspect ratio and wind speed on air temperature. The improvement of the sky view factor can also be considered as part of the design process. Experimentation will be integrated with parametric modelling, programming, and optimization methods in this sector. Hue et al. [87] published a paper on this method. In this study, the experiment took the following structure: there was a predetermined total building gross floor area to be modelled as physical urban geometry for a given urban area. The experiment's goal was to determine the urban design with the optimum sky view factor value (maximum or least) for a given total building area constraint. The value of the maximum and minimum sky view factor defines the

dimension of the heat island's optimizable space.

2.5 Pollution dispersion in urban environment

2.5.1 Introduction

Pollution dispersion in street canyons can be influenced by both geometrical and meteorological approaches [88]. Numerous factors including urban morphology modification and changing the flow pattern affect the air quality in urban areas.

Two typical approaches of pollution modelling in urban design, namely reactive pollutant modelling and non-reactive pollutant modelling, also known as passive scalar will be discussed in the following sections. Furthermore, pollution dispersion mitigating measures will be presented.

2.5.2 Reactive pollutant

As mentioned in section 1.1.3, the reactive pollutant NO and NO_2 are taken into account while modelling pollution dispersion emitted by cars. As a result, the chemical reactions in the presence of ozone (O_3) are as follows:

$$NO_2 + h\nu \rightarrow NO + O \tag{2.7}$$

$$O + O_2 + M \rightarrow O_3 + O \tag{2.8}$$

$$NO + O_3 \rightarrow NO_2 + O_2 \tag{2.9}$$

where M (N_2 or O_2) is a molecule that absorbs surplus energy and so stabilises the O_3 molecule. In photochemical reactions, $h\nu$ stands for sunlight [89]. The transport equation of NO-NO_2-O_3 is integrated with CFD methods to model reactive pollutant dispersion in metropolitan areas. The reader is referred to [90] to learn more about these transport equations.

Many studies, including field measurements, wind tunnel experiments, and numerical simulations, have been conducted to model pollution in street canyons and urban environments. Baik et al. [90] , for example, used CFD methods to model reactive pollution dispersion in an urban street canyon with aspect ratio of one incorporating simple NO–NO_2–O_3 photochemistry. The findings of his research reveal that the magnitude of the advection or turbulent diffusion term is much larger than that of the chemical reaction term and that the advection term is largely balanced by the turbulent diffusion term. On the other hand, the budget analysis of O_3 concentration shows that the magnitude of the chemical reaction term is comparable to that of the advection or turbulent diffusion term. Baker et al. [91] employed CFD simulations using large eddy techniques to examine the effect of dispersion and transport of reactive pollutants in and above street canyons, in contrast to Baik's work[90], which used RANS techniques. According to this study, Spatial variation of pollutants within the canyon was found to be significant. The impact of vegetation on reactive air pollutant dispersion in street canyons has been studied by Moradpour et al. [92]. In this work, the photochemistry of NO-NO_2-O_3 is combined with CFD. The features of temperature and flow fields for various aspect ratios and leaf area densities of trees were investigated in this study. In addition, the properties of reactive pollutant flow and dispersion on street canyons in the presence of building-roof cooling were investigated. The results reveal that the flow pattern has an impact on nitrogen oxide dispersion. Moradpour's other research [93] looks at the impact of green roofs on pollution dispersion in street canyons with different aspect ratios, taking into account that pollutants are reactive. According to their findings, roof greening caused the distribution of pollutants to vary for aspect ratios of 0.5 and 1, and averaged concentrations showed slight variations as LAD changed. Their findings show that roof greening is a viable method for improving air quality and the thermal environment, particularly in deep street canyons. Kotake and Sano [94] predicted air pollution in a complex arrangement in their paper. Their findings display the relationship between street geometrical configuration and non-linear dispersion behaviour of chemically reactive pollutants. The effect of building-roof cooling on the flow and dispersion of reactive pollutants in an idealised urban street canyon was investigated in a study undertaken by Park et al. [95]. According to the

findings of this study, building-roof cooling reduces primary pollutant concentrations by about 2.4% when compared to non-cooling conditions. Building-roof cooling, on the other hand, raises ozone concentrations by around 1.1% by lowering nitrogen oxide concentrations in the street canyon as compared to non-cooling conditions.

2.5.3 Non-reactive pollutant

Despite the fact that vehicle emissions are chemically reactive, the majority of studies solely looked at passive pollutants (i.e., non-reactive scalars). Together with experimental investigations, computational fluid dynamics (CFD) are also employed to simulate scalar transport mechanisms. For instance, in the work of Ouro et al. [96], pollution dispersion is described as a passive scalar, which is an idealised non-reactive pollutants that is transported across a fluid volume. The movement of active and passive scalar values within a flow domain is driven by advective and diffusive processes, with turbulence playing a key role in their mixing and dispersion. In Chapter 3 section 3.6, the mathematical modelling of this approach, which is the primary emphasis of this work, will be discussed in greater depth. Most of these models that were developed uses the Reynolds Averaged Navier–Stokes (RANS) equations, with k-ε and k-ω as eddy viscoity variants for closure to the calculate Reynolds stress [97–100], as detailed in detail in section 3.2.1. Other studies that used CFD methods to investigate the effect of pollution dispersion as a passive model include the study of Baik et al. [101] where the impact of buildings with green roofs on air quality in street canyons was evaluated. In another study, Kim and Baik[88] investigated how ambient wind direction affects flow and dispersion in urban street canyons. In this study a renormalized k-ε turbulence model was employed and varied flow patterns depending on the ambient wind direction were demonstrated. The other work of Baik et al. [102] models urban flow and dispersion for three alternative building configurations: infinitely long canyon, finitely long canyon, and orthogonality junction canyons.

2.6 Approaches for mitigating pollution dispersion in urban modelling

2.6.1 Introduction

Air quality is a serious health concern in cities, where the majority of people live [103]. Improvements in air quality are linked to the adsorption of pollution from the air by numerous techniques, including diverse types of vegetation. Based on various research, different forms of vegetation can alter the mean flow and turbulence in the vicinity of the buildings which can deteriorate or improve the pollution dispersion at the pedestrian level [103–105]. Green spots include street trees, green façades, living walls, green roof, grass and bushes. Vegetations act as porous bodies that influence local dispersion patterns and aid in the deposition and removal of pollutants in the air. Aside from the possible reduction in air pollution, urban green space has other benefits, such as reducing urban heat islands, as addressed earlier in this chapter. It also benefits the health and well-being of the people.

Apart from the impact of vegetation on pollution dispersion in cities, additional factors such as urban morphology (e.g. building aspect ratios) and mechanical elements such as airflow and wind speed (e.g. The magnitude of the wind speed, flows incoming turbulent structure) are critical. Li et al. [104] summarise the effects of mechanical elements and urban morphology on pollution dispersion.

Among different methods of pollution abatement, the works that have investigated the influence of vegetations will be reviewed in the following sections, as the main focus of this study is analysing the effect of green spaces on velocity, UHI, and pollutant dispersion.

2.6.2 Trees

Increasing the percentage of green infrastructures in cities in one of the methods of reducing city air pollution. Trees are a type of vegetation that can be planted adjacent to traffic sources

or buildings. The air quality can be influenced by a variety of elements in trees. Tree species (e.g., evergreen or deciduous), tree age, tree height, tree location, and so on. Furthermore, whether the vegetation is tall or short, dense or sparse has an impact on air pollution from various sources and particle sizes. Moreover, the movement of pollutants is influenced by the direction of the wind and the structure of the landscape. As a result, urban tree design and selection are crucial [105]. Trees reduce pollutant dispersion by two mechanisms: first, they provide shade, and second, they reduce heat and are well-known for their abilities to absorb and deposit pollutants on their leaf surfaces [106]. When concentrated pollutants clash with trees, they are dispersed out and diluted by the air. This is known as dispersion and deposition occurs when contaminants are trapped in the leaves of trees. However, in this study the main focus is on dispersion as the leaves of the trees are neglected in the modelling.

To model the pollution dispersion, CFD modelling is used to simulate the aerodynamic and dispersion impacts of trees. The work of Abhijith et al. [103] examines the vegetation types including trees in open-road and built-up street canyon situations in decreasing air pollution. More complicated models, such as the work of Salmond et al. [107] on the effect of vegetation on the horizontal and vertical dispersion of pollutants in a roadway canyon, looked at the impact of vegetation at different seasons by simulating trees with and without leaves. During the summer, they discovered a huge variation in concentration, indicating that there was less mixing among the foliated tree crowns.

Although many studies suggest that vegetation can reduce pollution dispersion, others show that pollution dispersion can worsen owing to a variety of factors such as tree size, location, building design, street's aspect ratio, and so on [105]. According to BBC future team [108], planting tall trees with wide canopies on tiny streets surrounded by tall structures can exacerbate the problem by preventing pollution from dissipating. Hedges or green walls are frequently preferred to trees in this scenario. However, where there are broad highways surrounded by low-rise structures, air may travel more easily and pollutants are less likely to be trapped, making trees and hedges viable options.

It's worth noting that most street canyon models treat vegetation as a sink for turbulence and

momentum (see section 3.5), but they don't consider deposition. However, the effect of deposition has been evaluated in two simulations by Vos et al. [109] and Wania et al. [110] where higher pollutant concentrations were found due to vegetation in street canyons and between buildings accounting for the effect of deposition using Envi-met. ENVI-met is a microclimate and local air quality model based on CFD. It predicts the wind speed, air temperature, and thermal comfort. Validating Envi-MET models is difficult due to the vast number of variables and calculations required [111, 112]. Wania et al. [110] discovered that larger and denser trees had a significant impact on dispersion, whereas smaller and sparser trees had a minor impact. According to Vos et al. [109], planting vegetation near the source of traffic reduces pollution transport and enhances deposition.

Wind tunnel tests, in addition to simulation, can provide a lot of information about pollutant dispersion. However, downscaling of the vegetation adds a lot of ambiguity to these studies. As a result, such investigations should be linked to on-site measurements [113].

2.6.3 Green Façades

Green walls and green roofs are currently employed for sustainability reasons, although green walls were once only used for ornamental purposes [114]. This section provides an overview of green façades and their behaviour in relation to air quality improvement and social effects. Generally, Green façades are the addition of greenery to a building's exterior surface, which might take the shape of a green roof or a green wall (the traditional use of climbing plants against a façade from the ground) [43, 115]. As described earlier in this chapter, the lack of vegetation in urban areas contributes to the accumulation of carbon dioxide and other harmful pollutants [116]. Plants have the potential to absorb pollutants and exhale oxygen, improving air quality and providing environmental advantages [115]. Aside from pollutant absorption, green façade on buildings attract birds, insects, and other species, promoting diversity.

Green roofs can be divided into three categories: extensive, intensive, and semi-intensive roofs, as indicated in Figure 2.7. Extensive roofs are light, thin roof systems with a planting media

that is typically 6 to 20 cm deep, whereas intensive roofs are heavier, thicker green roofs with a growth media that is 20 cm to 100 cm thick. Semi-intensive green roofs are a hybrid of the two types of green roofs listed above. They have a thinner planting media than an intense roof but a thicker planting media than an extensive roof, and the entire system is between 120 and 250 mm [117]. Intensive roofs are the most expensive of the three methods, whereas extensive roofs are the least expensive. The report [115] presents further information on various types and costs. It must be noted that different layers of green roofs (e.g., water proofing membrane, growth substrate, and so on) are not taken into account in this study, and only the vegetation layer is simulated as a cubical green area.

(**a**) (**b**) (**c**)

Figure 2.7: Green roofs categories: (**a**) Extensive green roof; (**b**) Intensive green roof; (**c**) Semi-intensive green roof.

Green façades and living walls are two different types of vertical greenery systems. The structures of living walls are more intricate. Living walls differ from green façades in that they support vegetation that is planted in a substrate attached to the wall itself, rather than at the base of the wall. More information on living walls can be found in the study of Manso et al. [118]. Vertical greenery system can be classified into 4 groups including, tree against wall, wall climbing, hanging down and module type which are represented schematically in Figure 2.8. The reports [66, 119] present further information on various types and layers.

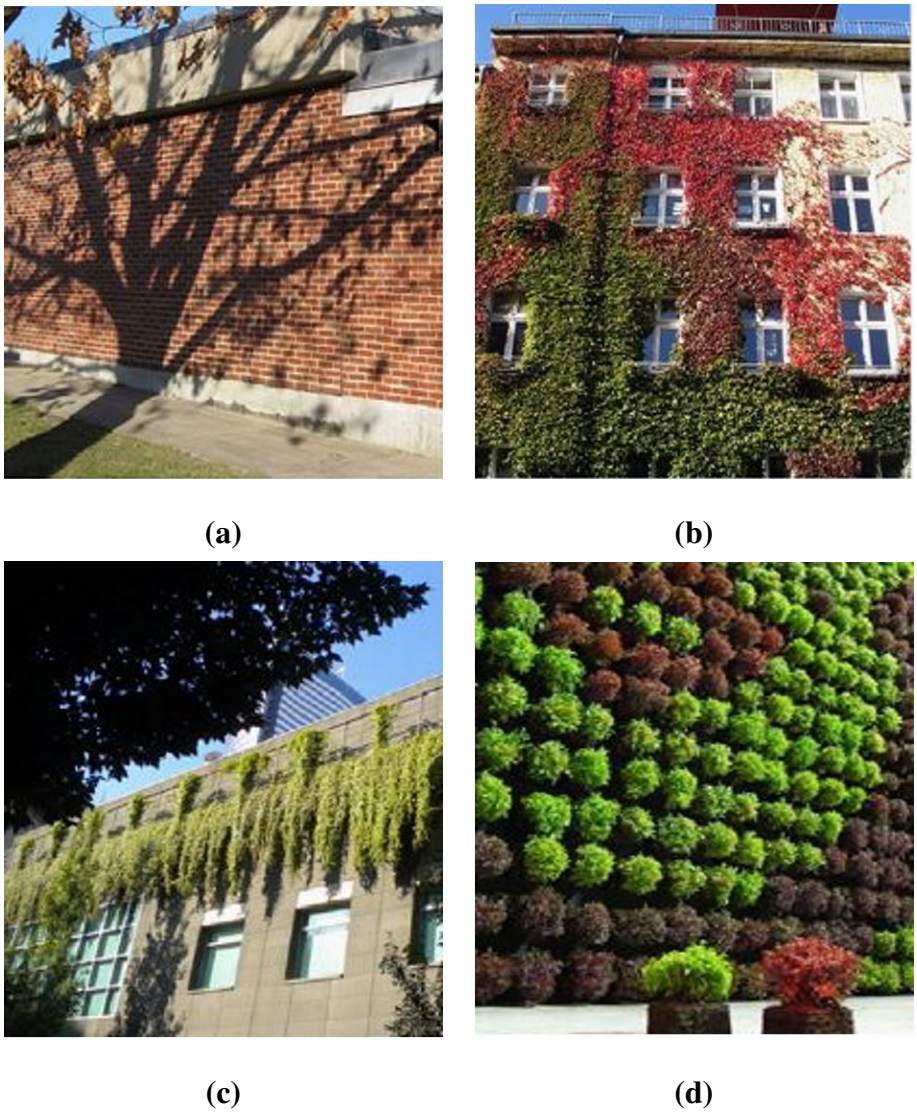

Figure 2.8: Green wall categories: **a**) Tree-against wall; (**b**) Wall-Climbing; (**c**) Hanging-wall; (**d**) Module-type. Images taken from [120].

There are numerous publications in the literature on the benefits of green façade in terms of air quality improvement. A state-of-the-art review [121] is a comprehensive research that assesses the environmental benefits of green roofs that are dedicated to reducing air pollution in a small area. This study shows how green roofs can help to make buildings and towns more sustainable by lowering energy consumption, reducing the urban heat island effect, improving air pollution,

water management and preserving the environment. Raji et al. [117] evaluated the effect of green roofs, green walls, green balconies on temperature, heat flux and on HVAC systems where the main aim of his work was providing a literature review for all different greening systems with respect to their energy impact. In addition the effect of indoor planting on indoor air quality was discussed. According to his findings, the maximum efficiency of greenery systems is reported during summer. Furthermore, the efficiency of greenery concepts depends strongly on the climate factors such as temperature, relative humidity, solar radiation (sky clearness and radiation angular distribution) and wind velocity. The effect of green roofs on air pollution reduction was quantified using a dry deposition model by Yang et al. [122]. According to the research, green roofs in Chicago may be able to remove a considerable amount of pollutants from the air. Theodosiou et al. [123] assessed major benefits of green roofs on UHI mitigation and air quality improvement. According to this study, the reduction in surface temperature caused by green roofs can result in reduced ozone pollution in the atmosphere. Qin et al. [124] investigated the impact of green roofs and green walls on the reduction of coarse PM_{10} pollutants in urban street canyons. In this work a series of models were created for various building aspect ratios, greenery coverage areas, and leaf area densities. According to this study, Particle concentrations in green walls are lower than those in green roofs across the entire spatial domain with equal greenery coverage area and aspect ratio.

Green walls and green roofs can be compared depending on how effective they are at reducing UHI and improving air quality. A building's vertical area is usually greater than its roof area. This observation emphasizes the importance of vertical greening systems, especially for taller structures. However, maintenance and installation costs, as well as operational costs of green façades, are critical. Green façades cannot yet be used as a stand-alone solution in air pollution control due to their high cost. However, a close evaluation of its environmental benefits suggests that it could be a feasible option for lowering air pollution and other environmental problems [125, 126]. The cost of any vertical garden is determined by a variety of criteria, including the location, plant species, height, irrigation requirements and so on. Green façades, in whatever form, necessitate ongoing and long-term care. The benefits of green façades and

their costs are summarised in Table 2.2 [118].

Table 2.2: Urban benefits and costs. Taken from [118].

				Green roofs			Green walls	
				Extensive	**Semi-intensive**	**Intensive**	**Green façades**	**Living walls**
Ecosystem services	**Measurable**	**Building/ local**	**Energy savings (Maximum values)**	100% Cooling (Cfb N-Ins.) 73% Heating (Csa Ins.)	67% Cooling (Csa N-Ins.) 68% Heating (Csa N-Ins.)	84% Cooling (Csa N-Ins.) 71% Heating (Csa N-Ins.)	34% Cooling (Csa)	66% Cooling (Csa)
			PV performance	1.35%–3.35% increase	(Avg = 2.6%)		No data available	
			Sound transmission	<5 dB–20 dB	No data available			
			Greywater treatment	No data available				<80%–90% TSS <90% BOD <30–50% TN <15–30% TP <30–70% COD <20–80% E. coli
			In service life	28 years–47 years (Avg = 40 years)			Avg = 50 years	
			Property value	16,2% (Avg = 8.24%)			Avg = 50 years	
			Risk of fire	No data available				
			Incentive policies	No data available				
		Urban	UHIE	0.97 ∘C – 2.29 ∘C (Avg = 1.34 ∘C)			Avg = 1.37 ∘C	
			Urban noise	≈10 dB	No data available			0 dB–10 dB Avg = 5.5 dB
		Air quality (Maximum values)	Water management Storm water Runoff Rainwater Retention	<33% - <81% (Avg <57%) Avg = 8% Cd Avg = 5% Pb Avg = 80% NO3 Avg = 68% PO4 <49% - <90% (Avg <71%)	No data available		<40% O3a <11,7–40% NO2 <42%–60% PM10 <3,5% SO2a <1,34% COa <1,34% PM2.5a	
			Peak runoff	Avg <20% O3 Avg <29% NO2 Avg <79% PM10 Avg >37% SO2				
		Urban farming	No data available					
	Intangible		Health/well-being Biodiversity Aesthetic value Recreational value	Use alternative methodologies of measurement as enquiries, multicriteria analysis, etc.				
Costs			Installation (€/m^2)	67 - 128 (Avg = 99)	112 - 148 (Avg = 130)	156 - 627 (Avg = 362)	114 - 266 (Avg = 190)	408 - 1091 (Avg = 750)
			Operation/Maintenance (/ year)	0,84–9,16 (Avg = 4.28)	Avg = 7.77	0.72–12.75 (Avg = 5.64)	2.06–9.07 (Avg = 5.57)	Avg = 18.98
			Disposal (€/m^2)	Avg = 12	No data available	Avg = 26	44 - 146 (Avg = 95)	Avg = 239

2.7 Wind micro-climate assessment

2.7.1 Introduction

Wind microclimate is a predictive approach to assess the air flow patterns around the buildings. CFD techniques are integrated with the local wind data in this assessment to determine wind speed at the pedestrian level [127]. Understanding building aerodynamics and pedestrian-level wind conditions is crucial in the design of new developments since high-rise buildings can significantly increase pedestrian-level wind velocity [128]. Increased pedestrian-level wind speed can be uncomfortable and should be minimised. As a result, the first step in addressing this issue is measuring the flow around the buildings, followed by reducing the unfavourable wind speed using the mitigation methods outlined in the next section. To do this, experimental and numerical analyses of wind patterns in the surrounding area can be carried out. Wind tunnel testing is one of the most widely used experimental procedures for determining wind flow patterns in urban environments. To do so, a scaled-down model of the site is fitted inside a wind tunnel. Wind tunnels must be used to recreate the turbulence typical of the wind. [129]. The numerical approach assesses the wind pattern at the pedestrian level (2 m) using CFD techniques. The wind patterns around buildings are defined by the corner effect, downwash effect, speed effect, flow separation and so on [130–136]. Some of the researches in microclimate assessment study including the work of Van et al. [128] where he compared different building geometry adjustments for lowering pedestrian-level wind speed around a single high-rise building. Wang et al. [137] estimated the wind speed in urban areas based on the correlations between background wind speeds and morphological factors. These parameters include: volume fraction of buildings, plane-area fraction of buildings and the average height of the buildings. According to this study, the wind speeds and morphological parameters could be used to estimate 2D wind speed distributions, and that the wind speeds estimated in the centre of the numerical domains were influenced by the surrounding morphological parameters as well as the background wind directions. The model in their work was created by performing CFD simulations for 32 inflow directions to determine the rate of change in wind speed between the inflow boundary and the

location of the weather station measurement. Multiple regression was used to examine the relationships between the rate of change in wind speed and the morphological factors for 32 inflow directions in each target area. Arkon and Özkol [138] investigated the impact of building geometry on pedestrian level wind speed. The effect of variables such as building height, various building configurations (e.g. parallel, cross, t-shape, t-cross), upwind direction, and velocity configurations on pedestrian-level wind speed was investigated in this work. The following are some of the findings of the studies: When the aspect ratio is between 0 and 1, the canyon effect can be perceived as reduced pedestrian-level wind speeds, while when the aspect ratio is 1, the canyon effect can be seen as increased pedestrian-level wind speeds has a negative impact on pedestrian wind speed. Furthermore, when the upwind is perpendicular to the canyon axis, the angle of the upwind plays an important role.

2.7.2 Adaption measures for pedestrian level wind speed mitigation

Creating comfortable and functional outdoor areas is more vital now than it has ever been. This necessitates the development of wind mitigating methods. Following the wind microclimate assessment, the areas of high velocities due to high-rise buildings are identified. This can be inconvenient for pedestrians, so positive measures must be taken to counteract the negative effects of wind. Wind speed, wind direction, building morphology, street aspect ratio, building aspect ratio, and many other elements influence wind speed at pedestrian levels, as mentioned in the previous section. Wind speed can be reduced by modifying and optimising these factors. There are also external objects, which are frequent strategies for reducing wind speed, which are described below [63, 139, 140].

- Vegetations
- Canopy
- Porous screen

Planting vegetation in urban areas contributes to urban heat island reduction, lower energy consumption, wind speed mitigation, and air pollution mitigation, as indicated in sections 2.4.2 and 2.6.2. Trees and greenery systems, which mostly consist of green roofs and green walls, are examples of vegetation. As a result, integrating greenery systems into buildings in urban areas offers a lot of potential to improve urban environment quality. The review papers [63, 139] are extensive studies that explain the research that has been undertaken so far to evaluate the influence of important methods such as the effect of trees in wind speed reduction. Additionally, Salim et al. [141] analyses the dynamic effect of trees in numerical simulations of wind flow in urban areas. It was found in this study that wind direction, leaf density, and urban configuration all play a role in the efficiency of trees in reducing wind speed.

Canopies are solid materials that are effective at reducing down draught wind effects. The influence of canopies and podiums on wind mitigation around a single building is investigated in the study of Van et al. [128]. It has been discovered that a canopy can dramatically lower pedestrian wind speed by up to 29%. It should be noted that the size and location of the canopy will be influenced by the building's location and size. They are usually unsuitable for direct wind exposure, wind funnelling between buildings, or wind acceleration around corners [142].

Porous screens are most effective when they are located near building corners and entrance. They provide protection by absorbing wind energy and are typically used for small, localised areas [140]. Direct wind exposure and wind funnelling between buildings can both be reduced by porous screening. When compared to solid screens, porous screens have been shown to prolong the distance for which shelter is provided [143].

Other methods of lowering wind speed include the use of permeable intermediate floor which allows upper-level wind to pass through the building before reaching ground level as it's been discussed in the work of Lam et al. [144]. The efficiency of corner modification of buildings on wind speed reduction was studied by Uematsu et al. [145]. Four different corner shapes including tapering and rounding corner were tested in this investigation. The findings of this study showed that rounding corner improve the wind environment by limiting the extent of

high wind speed zone near building corners due to less deviation of isolated flow. The effect of various building heights and wind direction that provide the most critical wind velocity condition was studied by Sathappoulos and Storms [146]. According to the findings of this experiment, increasing building height results in increasing the wind velocity amplification between passages. It's also worth noting that for the azimuth of -90°, the velocity reduces and turbulence increases substantially more than for the azimuth of 90°.

Apart from the measures listed above, windtech experts [142] suggest other options including: baffle screens, balcony end screens, artwork, overhang shade, localised screening, public art, and so on to lessen the influence of wind impacts. some popular mitigating approaches are schematically shown in Figure 2.9.

2.8 Summary

The methods of UHI modelling, pollution dispersion, and wind-microclimate have all been reviewed in this chapter. Considering the advantages and limitation of various techniques, such as observational technique, UCM, and CFD, CFD is thought to be capable of predicting wind speed, air temperature and pollution concentration in urban areas. As a result, all simulations in this thesis are based on CFD methods. In addition to introduction of the method of numerical modelling of urban environments, several strategies for reducing UHI, air pollution, and wind speed were also discussed. The comprehensive overview of these methods suggest that vegetation, whether in the form of green façades or trees, is capable of providing pedestrian comfort, lowering pollution levels, and air temperature in urban areas. Numerous research have assessed and discussed the effectiveness of these strategies, which are discussed in this chapter. However, a number of factors influence their effectiveness, including location, vegetation type, green coverage ratio, urban morphology, and building height. The location and height of the building however, are fixed in this study. The effects of the aforementioned strategies are investigated in further depth in Chapters 5 and 6 of this thesis.

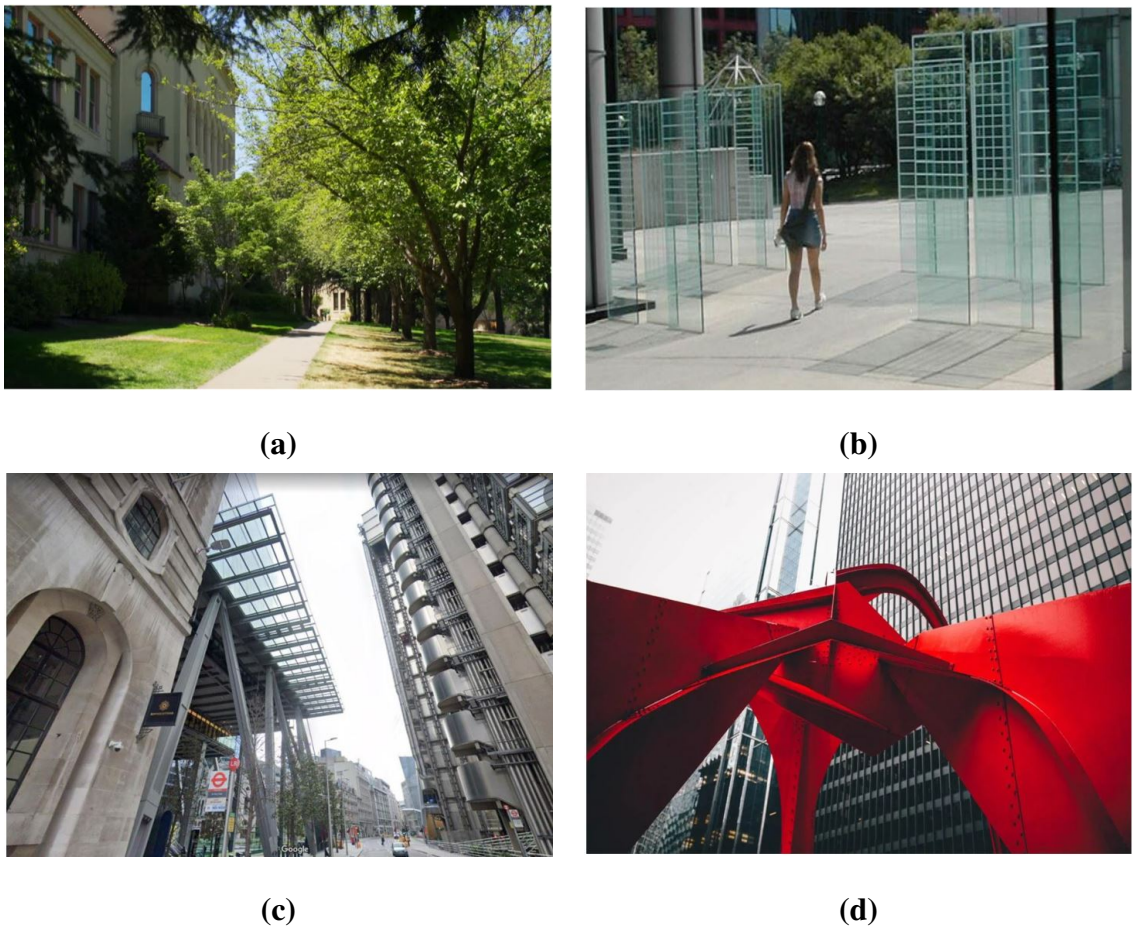

(a) **(b)**

(c) **(d)**

Figure 2.9: Wind speed mitigation methods: **a**) Trees; (**b**) Porous screen; (**c**) overhang shading; (**d**) solid canopies; Images taken from [142].

Chapter 3

Mathematical modelling of thermal environment

3.1 Preliminary remark

The comprehensive mathematical models that are required for simulation of the urban environment are described in detail in this chapter. This includes the governing equations for flow, turbulence modelling, heat transfer, vegetation and modelling of pollution.

3.2 Turbulence modelling

Turbulence modelling of flow around buildings can be done in a variety of ways. Reynolds Averaged Navier-Stokes (RANS), Direct numerical simulation (DNS), and large eddy simulation (LES) are three of the most common methods detailed in the following sections [32, 147–149]. All the simulations presented in this work are based on the RANS turbulence models, including the standard k-ε, realizable k-ε, standard k-ω and SST k-ω.

3.2.1 Reynolds Averaged Navier-Stokes(RANS)

The Reynolds averaged Navier-Stokes equations are derived by time-averaging the Navier-Stokes equations. For incompressible flow, the Navier-Stokes momentum and continuity equations, expressed in tensor notation, are defined as Equation 3.1 and 3.2 respectively. [150, 151].

$$\frac{\partial u_i}{\partial t} + u_j \frac{\partial u_i}{\partial x_j} = \frac{-1}{\rho} \frac{\partial p}{\partial x_i} + \frac{\partial}{\partial x_j}(\frac{\mu}{\rho} \frac{\partial u_i}{\partial x_j}) + g_i \tag{3.1}$$

$$\frac{\partial u_i}{\partial x_i} = 0 \tag{3.2}$$

Equation 3.3 and 3.4 are used to define Reynolds-averaged quantities.

$$u_i(x_k,t) = \overline{u_i}(x_k,t) + u'(x_k,t) \tag{3.3}$$

$$\overline{u_i}(x_k,t) = \lim_{T\to\infty} \frac{1}{T} \int_0^T u(x_k,t)dt \tag{3.4}$$

The time-averaged momentum equation below is obtained by substituting the Reynolds decomposition for velocities and pressure in the Navier-Stokes momentum equation.

$$\frac{\partial \overline{u_i}}{\partial t} + \overline{u_j} \frac{\partial \overline{u_i}}{\partial x_j} = \frac{-1}{\rho} \frac{\partial P}{\partial x_i} + \frac{\partial}{\partial x_j}(\frac{\mu}{\rho} \frac{\partial \overline{u_i}}{\partial x_j}) + \frac{\partial}{\partial x_j}(-\overline{u_i' u_j'}) + g_i \tag{3.5}$$

Where u_i, $\overline{u}_i$ and $u^{'}$ are the velocity component in direction i, mean (time-averaged) velocity and the fluctuating velocity respectively. g_i and P stand for the the i-the component of the acceleration due to gravity and mean pressure field. Given transient data over a sufficiently large time, the average of velocity can be numerically computed within some small error (Equation 3.4). The term $\overline{-u_i' u_j'}$ is the specific Reynolds stress tensor, which must be expressed in terms of averaged quantities. The net rate of momentum over a surface caused by turbulence in the field is known as Reynolds stress and is defined by the Reynolds stress transport model.

The Boussinesq hypothesis is a type of turbulence modelling approach that uses the eddy viscosity coefficient to relate the mean turbulence field to the mean velocity field in the RANS method. Equation 3.6 shows this theory mathematically. Equation 3.7 shows the relationship

between the strain tenor S_{ij} and the velocity field.

$$R_{ij} = \overline{-u_i' u_j'} = \frac{2\mu_t}{\rho} S_{ij} \tag{3.6}$$

$$S_{ij} = \frac{1}{2}\left(\frac{\partial \overline{u_i}}{\partial x_j} \frac{\partial \overline{u_j}}{\partial x_i}\right) \tag{3.7}$$

where μ_t refers to eddy viscosity which is a scalar variable in this approximation. R_{ij} and S_{ij} stand for specific Reynolds stress tensor and strain tensor respectively. In Reynolds stress modelling, effects of anisotropy are also considered. This method is more complex and computationally expensive while, eddy viscosity modelling has a lower computational cost. There are a number of transport equations that are added to RANS equations and enclose the problem when using eddy viscosity models. These models begin with a zero-equation model and progress to a four-equation model.

Mixing length model and Spalart-Allmaras are two examples of zero equations. The k-model is a one-equation turbulence model that can be used. Standard k-ε, revised version of k-ε (e.g. realizable k-ε [152, 153], k-ω and revised k-ω (SST k-ω) [154] are well-known methods in urban environment modelling among two equations models. Additional equations in the In k-ε model are turbulent kinetic energy and turbulent dissipation energy, which will be discussed in depth in the next sections. k-ε-A is employed in three equations turbulence modelling. V^2f, elliptic blending, and lag elliptic blending are common methods among 4-equation turbulence models.

Eddy viscosity methods work well in many CFD simulations for urban environments, and the additional computational cost of the Reynolds stress model to characterise anisotropy is not justified [154, 155]. In the context of urban climate simulation, the number of urban environment studies which employed turbulence models based on the RANS approach were given in a review study published in 2017 [32]. This distribution rate is depicted in the Figure 3.1.

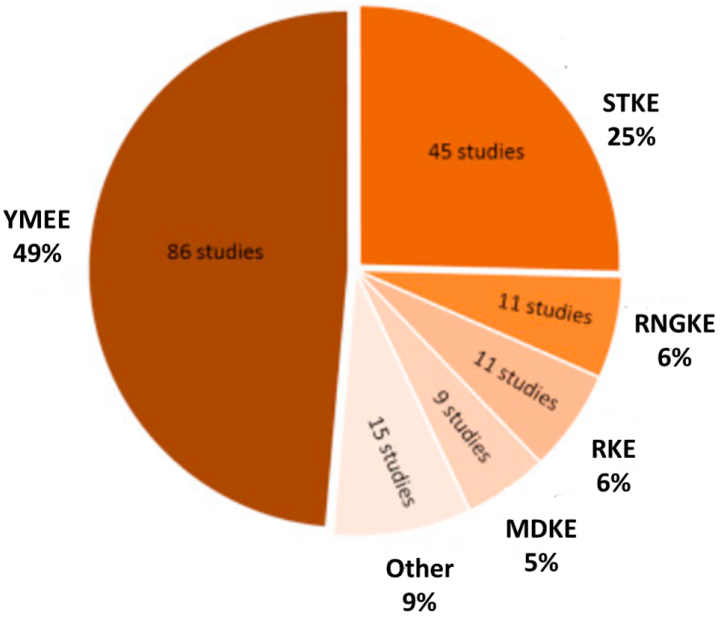

Figure 3.1: Distribution of turbulence model with RANS: Others are studies with SSTKW, MEE, ED, DKE, LRNKE, AKNKE and CKEKE. abbreviation: MDKE (modified k-ε, RKE (realizable k-ε), SSTKW (SST k-ω), RNGKE (RNG k-ε), STKE(standard k-ε), YMEE(Yamada and Mellor E-ε), LRNE(Low Reynolds number k-ε), ED(eddy viscosity), CKEKE (Chen-Kim Extended k-ε model), AKNKE (AKN k-ε). Image taken from [32].

Standard K-ε

The k-ε turbulence model is a two-equation model that determines turbulent eddy viscosity by solving transport equations for turbulent kinetic energy and turbulent dissipation rate. The standard k-ε model contains 5 unknown constants and is defined with turbulent kinetic and dissipation energy. The kinetic energy equation for incompressible flow is defined by equation 3.8.

$$\frac{\partial K}{\partial t} + \overline{u_j}\frac{\partial K}{\partial x_j} = \frac{\mu_t}{\rho}S^2 - \varepsilon + \frac{\partial}{\partial x_j}[\frac{1}{\rho} + (\mu + \frac{\mu_t}{\sigma_k})\frac{\partial k}{\partial x_j}] + S_k \tag{3.8}$$

Turbulent dissipation energy is defined by:

$$\frac{\partial \varepsilon}{\partial t} + \overline{u_j}\frac{\partial \varepsilon}{\partial x_j} = \frac{\varepsilon}{k}(c_{1\varepsilon}\frac{\mu_t}{\rho}S^2 - c_{2\varepsilon}) + \frac{\partial}{\partial x_j}[\frac{1}{\rho} + (\mu + \frac{\mu_t}{\sigma_\varepsilon})\frac{\partial \varepsilon}{\partial x_j}] + S_\varepsilon \tag{3.9}$$

The eddy viscosity correlation in STARCCM+ is defined based on equations 3.10 and 3.11 respectively.

$$\mu_t = \rho c_\mu K T' \tag{3.10}$$

$$T' = \max(\frac{K}{\varepsilon}, c_t\sqrt{\frac{\nu}{\varepsilon}}) \tag{3.11}$$

S_k and S_ε in Equations 3.8 and 3.9 are turbulent source terms. c_t is the time scale coefficient, which has a default value to 0.6 and $\sqrt{\frac{\nu}{\varepsilon}}$ is Kolmogorov scale. Away from a wall $T' = \frac{K}{\varepsilon}$ [151]. The default value of the required constants used in standard kε model is in Table 3.1.

Table 3.1: Variables in standard k-ε model

$c_{1\varepsilon}$	$c_{2\varepsilon}$	c_μ	c_t	σ_k	σ_ε
1.44	1.92	0.09	0.6	1	1

Revised k-ε model such as Launder-Kato (LK), MMK k-ε models are also recommended for prediction of wind flow at pedestrian level. The difference of these models with standard k-ε model is in the production term of kinetic energy. More information on these equations can be found here [132]. It has been determined that the computational stability of this model are better than nonlinear k-ε model. Thus, revised k-ε model is suggested for simulating flow around bluff bodies [156].

Realizable k-ε

The realizable k-ε model consists of new transport equation for turbulent dissipation rate (ε) and turbulent viscosity. In contrast to standard k-ε , c_μ is not constant and is a function of mean flow and turbulence properties.

The transport equation of ε for incompressible flow in this model are defined as below:

$$\frac{\partial \varepsilon}{\partial t} + \frac{\partial}{\partial x_j}(\varepsilon \overline{u_j}) = \frac{1}{\rho}\frac{\partial}{\partial x_j}(\mu + \frac{\mu_t}{\sigma_\varepsilon})\frac{\partial \varepsilon}{\partial x_j} + C_1 S_\varepsilon - C_2 \frac{\varepsilon^2}{k + \sqrt{\nu\varepsilon}} + \frac{1}{\rho} c_{1\varepsilon}\frac{\varepsilon}{k} c_{3\varepsilon} G_b \tag{3.12}$$

In this equation, G_b represents the generation of turbulence kinetic energy due to buoyancy. More information on the formulation of c_μ and ε equation can be found in refs. [153, 157].

Standard k-ω

K-ω models are similar to k-ε in that two transport equations are solved, but differ in the choice of the second transported turbulence variable. This model allows for a more accurate near wall treatment. To determine the turbulent eddy viscosity, this model uses the dissipation rate per unit turbulent kinetic energy ($\omega \propto \frac{\varepsilon}{k}$). The k and ω equations are defined as Equations 3.13 and 3.14 [158–160]. The model does not employ damping functions and has straightforward Dirichlet boundary conditions, which leads to significant advantages in numerical stability. However, this model underestimates the amount of separation for severe adverse pressure gradient flows.

$$\frac{\partial}{\partial t}(\rho K) + \frac{\partial(\rho \overline{u_j} K)}{\partial x_j} = \frac{\partial}{\partial x_j}[(\mu + \sigma_k \mu_t)\frac{\partial K}{\partial x_j}] + p_k - \rho\beta^* f_{\beta^*}(\omega k - \omega_0 k_0) + S_k \tag{3.13}$$

$$\frac{\partial}{\partial t}(\rho \omega) + \frac{\partial(\rho \overline{u_j} \omega)}{\partial x_j} = \frac{\partial}{\partial x_j}[(\mu + \sigma_\omega \mu_t)\frac{\partial \omega}{\partial x_j}] + p_\omega - \rho\beta f_\beta(\omega^2 - \omega_0^2) + S_\omega \tag{3.14}$$

where $\overline{u}$ stands for the mean velocity, μ for the dynamic viscosity. σ_k, σ_ω are model coefficient. p_k and p_ω are production terms. f_β and $f_{\beta^*}$are vortex-stretching modification and free-shear modification factors respectively. S_k and S_ω are source terms. The default value of the required constants in the present simulation is in Table 3.2 [151].

Table 3.2: Variables in standard k-ω model

σ_k	σ_ω	β	β^*
0.5	0.5	0.072	0.09

SST k-ω

Development of the SST k-ω (shear stress transport k-ω) arose due to the fact that the k-ε model is restricted to use of near-wall treatments without wall damping functions. The SST k-ω model uses k-ω model close to walls and alters to k-ε model away from walls. These two models are combined together with blending functions (functions of wall distance), meaning that cross diffusion term will be used far from the wall and not near the wall. The k-ε model has sensitivity to free stream/inlet conditions because of ε transport equations from the standard k-ε model. This way, ε can be transformed to ω equations. The k and ω model is defined by equations 3.15 and 3.16 respectively.

$$\frac{\partial K}{\partial t} + \overline{u_j}\frac{\partial K}{\partial x_j} = \beta\omega k + \frac{\partial}{\partial x_j}[(\nu + \sigma_k \nu_t)\frac{\partial K}{\partial x_j}] \tag{3.15}$$

$$\frac{\partial \omega}{\partial t} + \overline{u_j}\frac{\partial \omega}{\partial x_j} = \alpha S^2 - \beta\omega^2 + \frac{\partial}{\partial x_j}[(\nu + \sigma_\omega \nu_t)\frac{\partial \omega}{\partial x_j}] + 2(1 - F_1)\sigma_{\omega 2}\frac{1}{\omega}\frac{\partial}{\partial x_i}\frac{\partial \omega}{\partial x_i} \tag{3.16}$$

where ν and ν_t refer to eddy viscosity and kinematic eddy viscosity and F_1 is the blending function. In the boundary layer's sublayer and logarithmic region, F_1 is supposed to be 1, but it changes to zero in the wake region. SST k-ω formulation, is basically the Wilcox model [159] active in the near wall region and the standard k-ε model active in the outer wake region and free shear layers. The more details of this model are found in Ref. [154]. α is the model coefficient and is 0.52.

3.2.2 Direct Numerical Simulation (DNS)

The objective of this approach is to solve the time dependent Navier-Stokes equations for all eddies (small and large) for a specific time step so that the fluid properties reach equilibrium [161]. In this method, there is no turbulence modelling and the whole spatial and temporal scales of turbulence must be resolved. A high resolution of grid is required which leads to huge computational cost. Due to the fact that in wind engineering and city simulation, large computational domain is required, the use of DNS is restricted and is not cost effective [162].

This approach is more suitable for low Reynolds number flows and simple geometries.

3.2.3 Large Eddy Simulation (LES)

This turbulence modelling is required for geometry dependent problems. In contrast to the RANS equations, the LES equations are derived by a spatial filtering process rather than an averaging technique where the large eddies are explicitly calculated and the small scales are modelled. This methods use filters for Navier-Stokes equations to take out small scales from the solution and resolve the large scales [161, 163].

The filtering process that is applied to the Navier-Stokes equations to distinguish the resolved from the unresolved scales are desribed by Equation 3.17. The following is the definition of a filtered quantity of $\overline{f}$.

$$\overline{f}(x) = \int_D f(x')\overline{G}(x,x';\Delta)dx' \tag{3.17}$$

where D is the entire domain, $\overline{G}$ is the filter function and Δ is the filter width to distinguish between small and large eddy. The scales larger than Δ is retained in the equation and smaller than which is called subgrid scales (SGS) will be modelled. The reason is because SGS are too small and cannot be resolved. The reader is referred to [164] for further information on these equations.

The mathematical representation equation of continuity and motion with LES for incompressible flow are shown by the equations below [165]. The large eddies which will be resolved are shown with $\sim$.

$$\frac{\partial \widetilde{u_i}}{\partial x_i} = 0 \tag{3.18}$$

$$\frac{\partial \widetilde{u_i}}{\partial t} + \frac{\partial(\widetilde{u_i}\widetilde{u_j})}{\partial x_j} = -\frac{1}{\rho}\frac{\partial \widetilde{p}}{\partial x_i} + \nu\frac{\partial^2 \widetilde{u_i}}{\partial x_i \partial x_j} - \frac{\partial \tau_{ij}}{\partial x_j} \tag{3.19}$$

where $\widetilde{u}$ and $\widetilde{p}$ are filtered velocity and pressure. τ_{ij} stands for the residual stress tensor. The effect of smaller unresolved scales is contained in the SGS stress tensor (τ_{ij}) and are modelled

using the Bossinesq approximation as below:

$$\tau_{ij} = 2\mu_t \widetilde{S_{ij}} - \frac{2}{3}(\mu_t \frac{\partial \widetilde{u_i}}{\partial x_j} + \rho K_{SGS}) \tag{3.20}$$

Where $\widetilde{S_{ij}}$ is the resolved or filtered strain rate tensor and will be computed through resolved velocity field, ρ is the density and K_{SGS} is the subgrid scale turbulent kinetic energy. μ_t stands for the subgrid turbulent viscosity and are described by the subgrid scale model and explains the effect of small eddies on the resolved flow. The subgrid scale model consists of a model which accounts for subgrid scale viscosity and stress tensor. These models are named as: Smagorinsky Subgrid Scale, Dynamic Smagorinsky Subgrid Scale and WALE Subgrid Scale. The most common method of SGS models is Smagorinsky-Lilly method. More details of this approach is found in Ref. [151, 166, 167].

Among the three turbulence modelling methods described, LES is faster than DNS but slower than RANS models. In addition, in comparison to RANS [168], the simulation time takes more than two orders of magnitude longer. RANS has the advantage of requiring less computer memory for high Reynolds numbers and is therefore preferred over others in the thermal simulation of urban environments due to high wind speed and complicated geometry. However, there are some works that have used LES for CFD simulation of urban environment including [169–172].

3.3 Wall function for rough surfaces

Because of the strong near wall gradients, obtaining the velocity profile is a critical task. The RANS turbulence model can be used to model boundary layers at walls in two ways. The first method is to resolve the boundary layers in the near wall region using low Reynolds number modelling (LRNM). The computational cost of LRNM is high as it requires a highly refined mesh. As a result, wall functions, which simulate a portion of the boundary layer with empirical equations, are employed in a wide range of applications [151]. The employment of wall

functions allows for a coarser mesh near the wall, which is computationally less expensive. Standard wall functions, on the other hand, may have significant inaccuracies in estimating heat fluxes. The viscous sublayer, buffer layer, and log-law layer are the three components of the boundary layer. In the viscous sublayer, The non-dimensional wall distance (Y^+) value is less than 1, whereas in the buffer layer, it is between 1 and 30. The Y^+ value of the log-law layer is more than 30. Y^+ should be less than 1 to employ a low Reynolds number strategy. This method is used to compute the velocity near the walls. While, Y^+ lies in the log-law layer using wall functions . The velocity can be estimated this way. Estimation is obviously less accurate than computation. However, due to the size of the computational domain, it is not always feasible to refine the mesh to attain $Y^+<1$. As a result, in this case, wall functions are used. The regions at the wall boundary layer are depicted schematically in Figure 3.2.

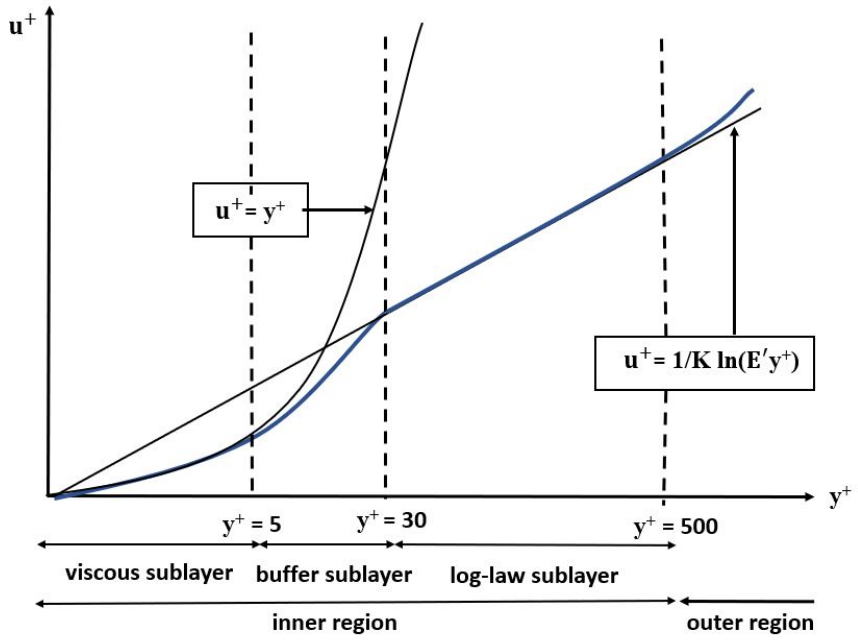

Figure 3.2: Regions in boundary layer. Image adapted from [151] .

The following equation is used to determine the Y^+:

$$Y^+ = \frac{u^+ y}{\nu} \tag{3.21}$$

The distance from the wall is given by y, the kinematic viscosity is given by ν, and the reference velocity is given by u^*. The reference velocity (u^*) is determined using the following equations:

$$u^* = \sqrt{\frac{\tau_w}{\rho}} \tag{3.22}$$

where τ_w is the wall shear stress and ρ is the fluid density.

Roughness height and roughness parameters must be defined in order to model the rough wall in the simulation. Rough walls have a different formulation of wall functions for the boundary layer than smooth walls. Aerodynamic roughness length is the added term for rough wall formulation.

$$u^*_{RH} = \frac{1}{K}\ln(\frac{y+z_0}{z_0}) \tag{3.23}$$

The aerodynamic roughness length is z_0, and the normal distance from the wall to the centroid of the wall cell is y. The flows in the atmospheric boundary layer are turbulent, and the velocity distributions are estimated using the following formula:

$$u^*_{tur} = \frac{1}{K}\ln(E^{'}Y^{+}) \tag{3.24}$$

$$E^{'} = \frac{E}{f} \tag{3.25}$$

E is set to 9 by default in STARCCM+. The value of the roughness function f for a smooth wall is unity, whereas it is equal to CR^{+} for rough functions. In STARCCM+, the roughness functions are defined using the equation below.

$$f(r) = \begin{cases} 1, & \text{Hydrodynamically smooth if } k_s^+ > 2.25 \\ (B.\frac{k_s^+ - 2.25}{90-2.25} + C_s k_s^+)^a, & \text{Transitional if } 2.25 < k_s^+ < 90 \\ B + C_s k_s^+, & \text{Fully rough if } k_s^+ > 90 \end{cases} \tag{3.26}$$

$$a = \sin(\frac{\pi}{2}.\frac{\ln(k_s^+/2.25)}{\ln(90/2.25)}) \tag{3.27}$$

C_s=0.253 and B=0 are the default values in STAR-CCM+. The following correlation is used to calculate roughness height:

$$R^+ = \frac{\mu r u^*}{\rho} \tag{3.28}$$

Where r is the corresponding sand-grain roughness height and u^* is the wall-function reference velocity.

$$E^{'} = \frac{E}{CR^+} \tag{3.29}$$

The equation below is obtained by equating the two velocities in equations 3.23 and 3.24 and substituting into equation 3.29.

$$\frac{y + z_0}{z_0} = \frac{EY^+}{CR^+} \tag{3.30}$$

Combining equations 3.29 and 3.30 gives:

$$\frac{y + z_0}{z_0} = \frac{Ey}{Cr} \tag{3.31}$$

If $y>z_0$ is assumed, the following equation is obtained, which is the basic equation for a wall function with roughness:

$$r = \frac{Ez_0}{C} \tag{3.32}$$

The aerodynamic roughness length can be used to calculate the roughness height, represented by r. The default values for E and C in STAR-CCM+ are 9 and 0.253, respectively. To achieve the desired roughness height, default values can be modified.

In the case of a rough wall, the effect of wall roughness is approximated by bringing the boundary layer's logarithmic region closer to the wall, as shown in Figure 3.3. This indicates that refining the mesh (initial cells from the wall) to a value less than 50% roughness is futile. It follows that $y_p>2r$, where y_p is the prism layer's initial height.

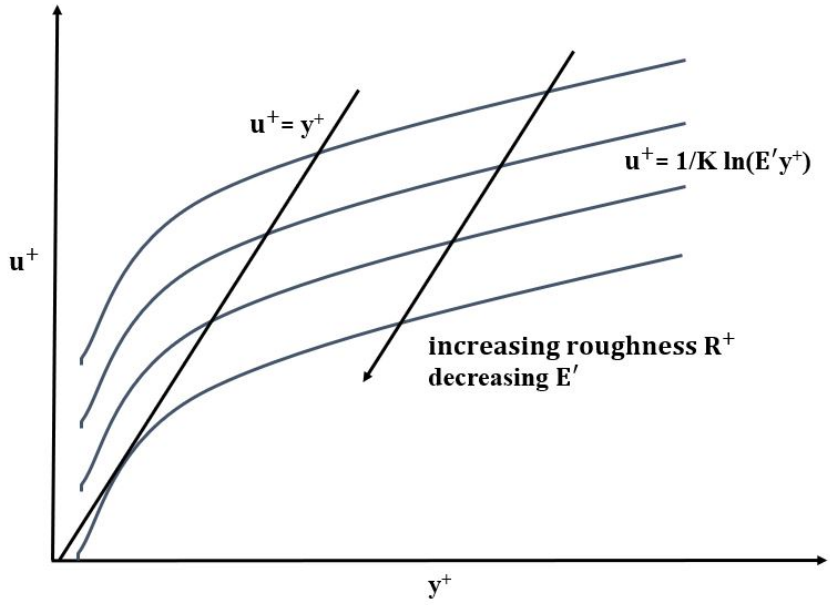

Figure 3.3: Wall treatment of rough walls. Image adapted from [151] .

All of the equations shown above are based on the use of common wall functions. When the blending function is employed, the reference velocity is calculated in a different way, which are shown below. Equation 3.33 is then used to define the blending function (g).

$$g = \exp(\frac{-Re_y}{11}) \tag{3.33}$$

The equation below is used to determine u^+ in the low, high, and all Y^+ procedures.

$$u^+ = \begin{cases} \sqrt{c_\mu^{1/2} k}, & \text{high } Y^+ \\ \sqrt{g\nu u/y + (1-g)c_\mu^{1/2} k}, & \text{low } Y^+ \\ \sqrt{g\nu u/y + (1-g)c_\mu^{1/2} k}, & \text{all } Y^+ \end{cases} \tag{3.34}$$

3.4 Heat transfer modelling

Conduction, convection, and radiation are three different heat transfer methods that occur around buildings. Figure 3.4 simply displays several heat transfer mechanisms on buildings.

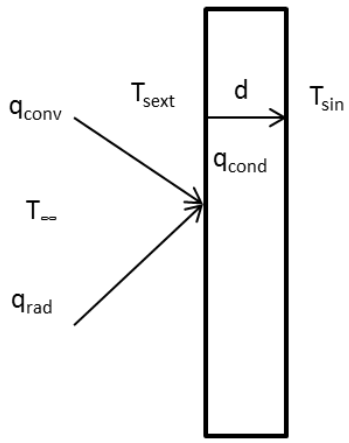

Figure 3.4: Heat transfer mechanisms on buildings.

Internal heat transfer is not depicted in the figure above. The equations describing external conduction, convection and radiation are mathematically shown from Equation 3.35 to Equation 3.37 [151].

$$q_{cond} = -k\nabla T = \frac{T_{Sext} - T_{sin}}{d} \tag{3.35}$$

$$q_{conv} = h_{\infty}(T_{\infty} - T_{Sext}) \tag{3.36}$$

$$q_{rad} = \varepsilon\sigma(T_{Sext}^4 - T_{\infty}^4) \tag{3.37}$$

Conductive, convective, and radiative heat transfer are represented by q_{cond}, q_{conv} and q_{rad} respectively. The object's thermal conductivity is k and the temperatures of the building's outside and inner surfaces are T_{Sext} and T_{Sin} respectively. The ambient temperature is T_{∞} and the thickness of the object is d.

Heat conduction is the transfer of internal energy from a hotter region to a cooler region through the contact of nearby particles. The transfer of thermal energy through the flow of a fluid is known as convective heat transfer and is usually classified as either natural or forced. Natural convection occurs in a gravitational field due to temperature changes that affect the density of the fluid and consequently its relative buoyancy. As a result, lighter components rise, while denser components descend [151]. This mode of heat transfer is the main focus of this study.

The emission of electromagnetic waves from all matter with a temperature greater than absolute zero is known as thermal radiation, and it symbolises the conversion of thermal energy into electromagnetic energy. Modelling the radiation can be done in a variety of ways. One of the most difficult aspects of a radiation model is determining how surfaces interact with one another and with the sky. Therefore, surface to surface schemes are very popular methods in radiation modelling. In this method, the effect of air as a medium is neglected. While, many studies show that scattering cause by pollution and particulates is a significant factor [7]. More information on surface to surface radiation model can be found here [173, 174].

Besides these 3 mechanisms on buildings, there are other sources of heat which exist in modelling of UHI. The surface energy balance is defined as equation 3.38 [175]:

$$Q^* + Q_F = Q_H + Q_E + \Delta Q_s + \Delta Q_A \tag{3.38}$$

The net all-wave radiation is denoted by the symbol Q^*. Q_F stands for anthropogenic heat, Q_H for sensible heat, Q_E for the latent heat, ΔQ_s for net heat storage, and ΔQ_A for net heat advection via the lateral side of the buildings. The left hand side represents the system's inputs, while the right hand side represents the system's output.

Convection and evapotranspiration processes at the surface are accounted by the sensible and latent heating factors, respectively [176]. More information on mathematical formulation of each term in Equation 3.38 can be found in Ref. [26]. Part of the source heat is transferred via the ground, building walls, and roof, while the other part is stored in the soil and ambient air, raising the temperature which is known as a heat storage. The most difficult term contained in the energy balance is the anthropogenic heat [177]. There are some estimations suggested by Grimmond et al. [178] which can give a rough idea of this term . Anthropogenic heat is made up of three components. The first term is a function of the kind and amount of gasoline used and corresponds to the number of vehicles in an area, the distance they travel, and their fuel efficiency (distance travelled per unit of gasoline). Electricity and gas are referred to as the second term. Residential properties (schools, churches, hospitals, and individual flats) as well

as industrial units can provide data. The third term is metabolic rates, which is defined as the ratio of the number of animals to the number of people, as well as the ratio of their metabolic rates. More information on anthropogenic heat mathematical modelling can be found in Ref. [178].

It must be noted that in the simulations in chapter 6, the heat source from the sun is represented in a simplified manner as bottom heating. Heat source from the sun affects the bottom temperature of the urban area as the sun warms the earth's surface. Other heat sources including anthropogenic was neglected [179].

3.5 Modelling of vegetation in urban areas

At computational cells that contain vegetation, variables are added to the transport equations of momentum (eq. 3.39), turbulence kinetic energy (eq. 3.40), and turbulence dissipation rate (eq. 3.41) to account for the impacts of vegetation on air flow (the terms in the boxes indicate the sink and source terms on vegetations) [180–183]:

$$\frac{\partial \overline{u_i}}{\partial t} + \overline{u_j}\frac{\partial \overline{u_i}}{\partial x_j} = \frac{\partial}{\partial x_j}[\nu(\frac{\partial \overline{u_i}}{\partial x_i} + \frac{\partial \overline{u_i}}{\partial x_j}) - \overline{u_i u_j}] - \frac{1}{\rho}\frac{\partial P}{\partial x_i} - \boxed{C_D a|u|u_i} \tag{3.39}$$

$$\frac{\partial k}{\partial t} + \overline{u_j}\frac{\partial k}{\partial x_j} = \frac{\partial}{\partial x_j}[(\nu + \frac{\nu_t}{\sigma_k})\frac{\partial k}{\partial x_j}] + P_k - \varepsilon - \boxed{C_D a(\beta_p|u|^3 - \beta_d|u|k)} \tag{3.40}$$

$$\frac{\partial \varepsilon}{\partial t} + \overline{u_j}\frac{\partial \varepsilon}{\partial x_j} = \frac{\partial}{\partial x_j}[(\nu + \frac{\nu_t}{\sigma_\varepsilon})\frac{\partial \varepsilon}{\partial x_j}] + P_k - \varepsilon - \boxed{C_D a(\beta_p c_{\varepsilon 4}|u|^3\frac{\varepsilon}{k} - \beta_p c_{\varepsilon 5}|u|\varepsilon)} \tag{3.41}$$

where C_D is the drag coefficient and a is the leaf area density, |u| refers to the velocity magnitude and u_i is the velocity component in direction i. Given many trees in the UK are deciduous, the average value for leaf area density is fixed as 1.6. The average leaf area densities for deciduous trees are approximated between 1.06 and 2.18 m^3m^{-3} [184]. The drag coefficients for most types of vegetation are between 0.1 and 0.3. The constant parameters for modelling of vegetations are defined in Table 3.3. β_p is the fraction of mean kinetic energy that is converted to the wake turbulence, β_d is the coefficient that accounts for short-circuiting of eddy cascade

and $c_{\varepsilon 4}$ and $c_{\varepsilon 5}$ are empirical coefficients [141]. These parameters can be slightly different for various types of vegetation [185].

Table 3.3: Constant parameters for tree modelling.

Constants	c_d	β_p	β_d	$c_{\varepsilon 4}$	$c_{\varepsilon 5}$
Value	0.2	1	4	1.5	0.4

To account for the impact of vegetation on air temperature, a volumetric cooling power is assigned to vegetation per unit volume which is a function of the leaf area density (LAD). The essential concept is that as air passes through vegetation, it is cooled through transpiration, which occurs mostly on the leaf surfaces. The heat required to change an object's temperature can be estimated using the equation 3.42 [180].

$$P_c = \dot{m} c_p \Delta T \frac{1}{V} \tag{3.42}$$

where P_c refers to volumetric cooling power which is a transfer of heat per volume per time, C_p is the specific heat capacity, ΔT the change in temperature where air flows through vegetation and V is the volume, $\dot{m}$ is the mass flowrate. Based on the work of Gromke [180], volumetric cooling power can be estimated as 250 W m^{-3} per LAD unity. This value is used in all simulations of chapter 6.

3.6 Modelling of air pollution within street canyons

A passive, non-scalar model is used to model traffic emissions in this study. Passive scalars are arbitrary-valued user-defined variables allocated to fluid phases or individual particles. They are passive because they have no effect on the simulation's physical properties. The CFD method is used in the modelling of air pollution in urban areas, as well as a passive scalar that is transported through a fluid volume in an idealised non-reactive medium. Transport equations consisting of convective and diffusive flow are included in passive scalar models

(see Equation 3.43 and 3.44) [151]. The movement of passive scalar values within a flow domain is driven by advective and diffusive processes, with turbulence playing a key role in their mixing and distribution [96]. The passive scalar model, which comprises of convection and diffusion terms, is chosen with an arbitrary passive scalar model to build up passive scalar tracking (here pollutant concentration). The passive scalar's transport equation is specified by the equation below.

$$\frac{\partial}{\partial t}\int_V \rho\phi\, dV + \oint_A \rho\phi(v - v_g)\, da = \oint_A J.da + \int_A S_\phi\, dV \tag{3.43}$$

where ϕ is the passive scalar and refers to the concentration of the pollutant in this work. S_ϕ is the pollutant's source term. The diffusion flux is denoted by J . The linear eddy-diffusivity model or the Generalized Gradient Diffusion Hypothesis model can both be used to express the diffusion flux J. The diffusion is modelled in this study using a linear eddy-diffusivity model specified by equation 3.44. Equations 3.45 and 3.46 calculate the turbulent viscosity and turbulent Schmidt number, which are essential variables for diffusion transport.

$$J = (\frac{\mu}{\sigma} + \frac{\mu_t}{\sigma_t})\nabla\phi \tag{3.44}$$

$$\mu_t = \frac{c_\mu k^2}{\varepsilon} \tag{3.45}$$

$$SC_t = \frac{\mu_t}{\rho D_t} \tag{3.46}$$

where SC_t is the turbulent Schmidt number, D_t is the turbulent diffusivity, μ is the viscosity, μ_t is the turbulent viscosity, σ is a molecular Schmidt number which is a material property, and σ_t is a turbulent Schmidt number.

In the simulation of contaminants in urban environments, the turbulent Schmidt number plays a key role. The Schmidt number was varied between 0.2 and 1 in the work of Gromke et al. [186] and its effect on computed concentration was studied. While this is defined as a value of 0.9 in Kim's study [187] utilising the RNG k-ε model. The value of 0.5 for turbulent Schmidt number was employed in the work of Jeanjean et al. [188], which was validated

against the wind tunnel data [184]. Jiang et al. [189] investigated the effect of Schmidt number on the projected concentration field in this study. He demonstrated that using the standard k-ε model, a Schmidt number of 0.4 produces the best results, and that a larger value leads to an overestimation of the concentration field. Since in this study, the standard k-ε is chosen for the simulations (see chapter 4) and based on the references mentioned here, the value of 0.4 is specified for turbulent Schmidt number in chapter 6 of this thesis.

The pollutant concentration is represented as a passive scalar, and the pollutant emission source is represented as a source term in the scalar transport equation, as previously stated. A volume source is used to represent traffic emissions. This indicates that at the required discharge location, the source terms are applied to the separated volume in the geometry. In chapter 6, the specific location of the source term is shown. The emission rate is set to 100 ppb s^{-1}, as suggested by Baik et al. [101], and used by Moradpour et al. [92]. This number represents the average traffic volume of 930 vehicles per hour [190]. The traffic emission's source can also be represented as a line or area source . The reader is referred to [91] for further information on the line or area sources of pollution.

Chapter 4

Numerical procedure of urban modelling

4.1 Preliminary remark

This chapter starts with the CFD analysis of wind speed for a generic configuration consisting of two parallel buildings (Test case 1). The input parameters (e.g., boundary conditions), mesh information (e.g., ratio of prism layer thickness to core cell size, number of prism layers), turbulence model and solver settings including velocity-pressure coupling are the same for this test case and for the East Village (i.e., Test Case 2, to be discussed in section 4.3.1). The results of this test case are validated with the experimental data reported in Blocken [191]. In the present work, a cylindrical domain is used as the computational domain in contrast to the work of Blocken where a block was used. The cylindrical domain was chosen to directly link and relate the numerical procedures in Test Case 1 to those in Test Case 2, where in the latter a circular domain was adopted to ensure adaptability to various wind directions.

4.2 Test case 1: CFD simulation of wind speed between parallel buildings

4.2.1 Computational domain and mesh

To make the application of wind direction easier, the computational domain used in this study is a cylinder with a circular subdomain. While there is only one inlet (i.e., the wind is blowing from one direction) when two buildings are used, in reality, and for a true urban geometry, the wind might be blowing from various directions. The computational domain, which consists of two buildings, is depicted in Figure 4.1. The size of computational domain is based on the guidelines for CFD simulations for pedestrian comfort [113, 192]. Based on that, the outflow boundaries must be 15 H_{max} at least, where H_{max} is the height of the tallest building. The top and inlet boundaries must be at least 5 H_{max} from the target area (vicinity of buildings). Buildings have a height of 10 m. As a result, the chosen cylindrical computational domain's radius and height are given as 150 m and 50 m, respectively. The building blocks are located within a smaller circular subdomain to distinguish between mesh sizes near and far from the area of interest. SolidWorks V.2019 was used to construct the CAD model in Figure 4.1a. Figure 4.2 shows how the computational mesh was constructed in STARCCM+ using unstructured tetrahedral and polyhedral meshes.

The grid resolution must meet the CFD standards. The grid resolution must be set to $\frac{1}{10}$ of the building scale as a minimum. The expansion ratio should not exceed 1.2. For parts that are far away from the target area, a coarser mesh is used. Close to the walls, prism layers are generated. The cell size on the building façade is 0.5 m, whereas the green interior part in Figure 4.1b is 1 m and the grey region is 8 m. To avoid an excessive volume ratio for adjacent cells, there should be a reasonable growth rate between the outer prism layer and the first core cell. To ensure this, the thickness of the prism layers adjacent to the wall is defined as 10%, 20% and 30% of the cell size of each section. The number of prism layers ranges from 2 to 5. With this size, around 1.4 million polyhedral cells are produced. The simulation results were

compared to the wind tunnel measurement data using the aforementioned grid size settings.

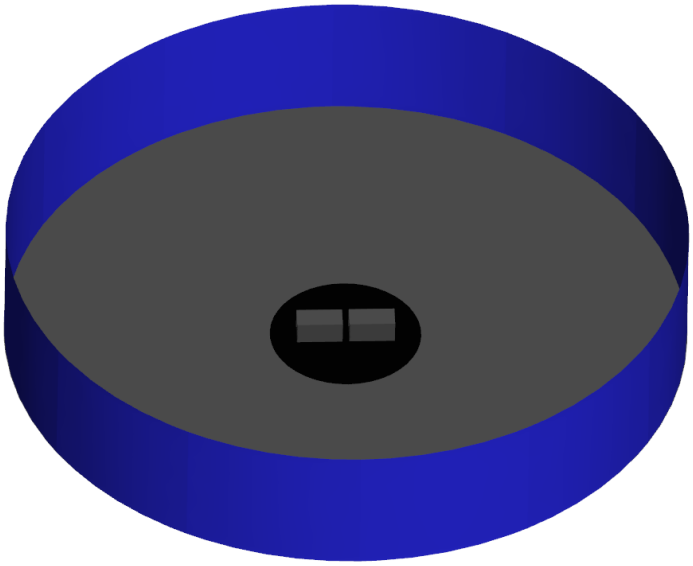

Figure 4.1: Computational domain for Test case 1.

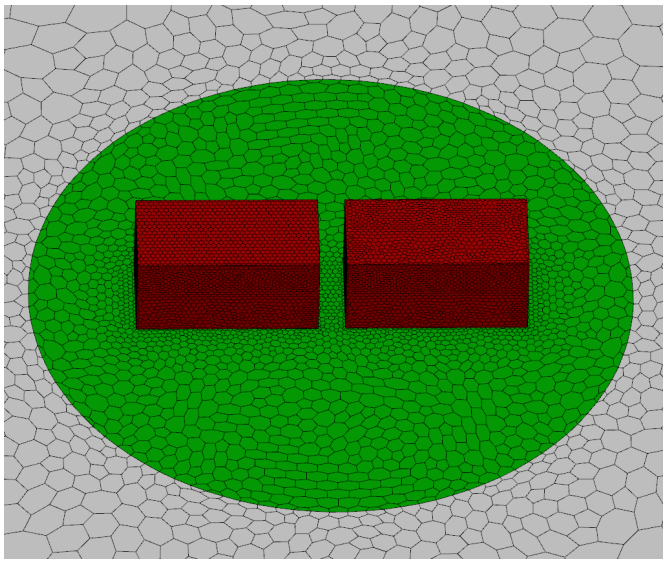

(**a**)

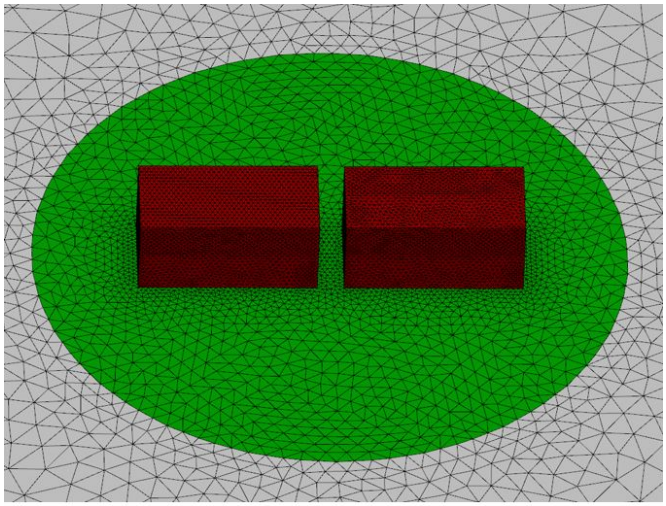

(**b**)

Figure 4.2: (**a**) Computational mesh for Test case 1: (**a**) Polyhedral mesh; (**b**) Tetrahedral mesh.

4.2.2 Governing equations and boundary conditions

Using RANS techniques, the equations that must be linked to resolve are continuity and momentum. Additional terms are required for closure of the mentioned equations to compute

the eddy viscosity model, which changes based on the type of turbulence model. The turbulent kinetic energy and turbulent dissipation energy are solved along with the continuity and momentum equations in the standard and realizable k-ε model. Specific dissipation rates are calculated when employing standard and SST (shear stress transport) k-ω [159, 160]. The SST k-ω model uses the k-ω model close to the walls and switches to k-ε model away from walls [154]. These two are combined with blending functions. The model was developed due to restrictions of the k-ε model in the treatment of the near-wall without a damping function. The formulation of these equations are discussed in section 3.2.1. All four models were used for a case study consisting of two buildings and a real-life case study in the East Village. After that, the accuracy of all the models was compared.

In terms of boundary conditions, the computational domain is divided into two sections of inlet and outlet. The velocity boundary condition is imposed on the flow at the inlet, while zero static pressure is applied at the outlet. [193]. A log-law profile is applied at the inlet shown in Figure 4.3 and Equation 4.1. The friction-free velocity (u^*) must be calculated based on the reference velocity. When the reference wind speed is 5.9 m/s at a pedestrian level of 2 m, u^* is determined as 0.587 m/s [194]. To specify turbulence parameters at the boundary, this velocity is essential. It must be noted that in this equation the effect of zero displacement (term 'd' in Figure 4.3) is neglected. For wind speed profiles over rough terrains such as forests, the concept of zero displacement is of importance [195, 196]. Since there is no accurate method that can be applied to determine the displacement length, the knowledge of u^* and z_0 completely defines the state of the wind. Thus, the effect of vegetation in Section 5.2 is expressed as a drag exerted on the surface, which is similar to the concept of zero-plane displacement [197].

$$\mathbf{u}(z) = \frac{u^*}{k} ln(\frac{z+z_0}{z_0}) \tag{4.1}$$

In the case of using k-ε, turbulent kinetic energy and dissipation energy are defined as follows [198]:

Turbulent kinetic energy:

$$k(z) = \frac{u^{*2}}{\sqrt{c_\mu}} \sqrt{C_1 ln(\frac{z+z_0}{z_0}) + C_2} \tag{4.2}$$

Turbulent dissipation energy:

$$\varepsilon(z) = \frac{u^{*3}}{k(z+z_0)} \sqrt{C_1 ln(\frac{z+z_0}{z_0}) + c_2} \tag{4.3}$$

In the case of using the k-ω model, specific dissipation rate is given by Equation (4.4) [154]:

$$\omega(z) = \frac{u^{*3}}{k\sqrt{c_\mu}} \sqrt{C_1 ln(\frac{z+z_0}{z_0}) + C_2} \tag{4.4}$$

In the equations for inlet boundary conditions, k is the von Karman constant, which has the value of 0.41. Cμ is a constant parameter set to 0.09 for the standard k-ε model. z_0 is the aerodynamic roughness length. C_1 and C_2 are 1.99 and 1.44 in the case of using the k-ε turbulence model. C_t, which is required for the eddy viscosity model in k-ε, is 1. The boundary condition at the top wall is a free slip wall. For solving the boundary layer close to the walls, the standard wall functions in combination with the sand-grain roughness modification are used [22]. The building walls and roofs are defined as smooth walls, while the ground is described as a rough wall.

The roughness function for the rough surfaces in STARCCM+ is defined by Equation 3.32 in section 3.3. The roughness parameters are given to all the walls. For building walls and roofs, the aerodynamic roughness length is zero and for the ground, has the value of 0.3. The roughness height should be min of ($30z_0$, $1/2y_p$). [194], where y_p is the distance between the centre point of the wall-adjacent cell to the wall.

The pressure–velocity coupling is combined with a segregated flow solver using a SIMPLE-type algorithm. Second-order discretisation schemes are used for all convection terms.

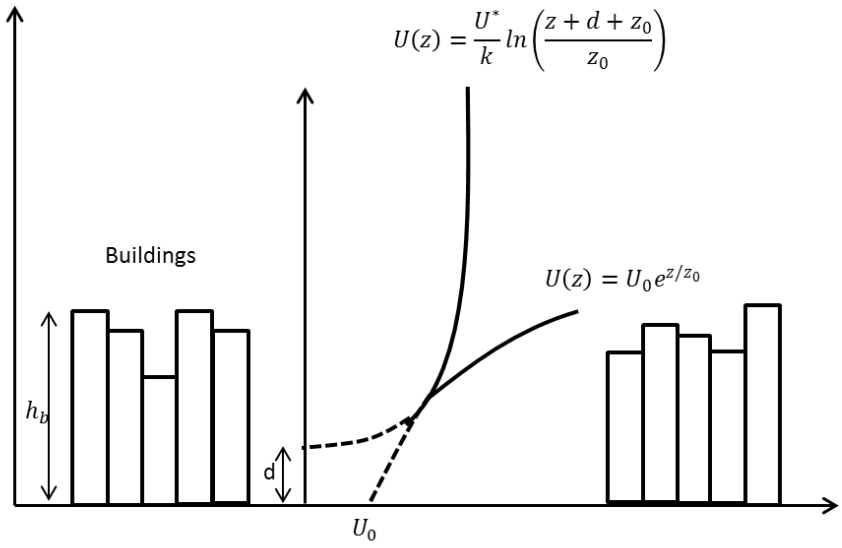

Figure 4.3: Logarithmic and exponential wind profile in surface layer. Image adapted from [199].

4.3 Test case 2: CFD simulation of East Village of London Olympic Park

4.3.1 Computational domain and grid

In this section, the wind assessment is carried out on a 3D model representing part of the development in the East Village in the London Olympic Park. The schematic of the CAD model and the location of this development are shown in Figure 4.4. A 3D model of this geometry was constructed using SolidWorks V.2019 software. The surface of the cylindrical computational domain is divided into 12 equal segments. The height of buildings varies between 17m and 102 m. The diameter and the height of the computational domain are 3 km and 500 m, respectively, which meet the criteria of the CFD guidelines and are large enough to avoid reverse flow pressure. The results using a polyhedral mesh type are closer to the measurement data than a tetrahedral mesh, according to the simulation of two buildings (Test case 1). As a result,

the same mesh type is employed in this case too. Buildings, internal subdomain, and far from buildings have cell sizes of 1.5, 3, and 24 m, respectively. The total number of cells generated is estimated to be around 6 million. The number of cells generated is fine enough as indicated by mesh independence test in Figure A.2 in Appendix A.

(**a**)

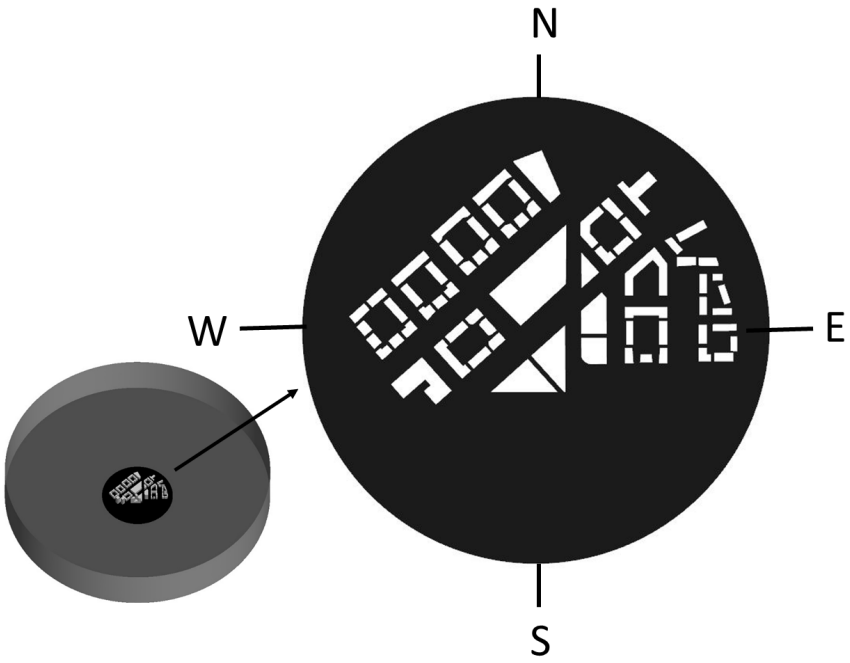

(**b**)

Figure 4.4: (**a**) The East Village location within the London Olympic Park; (**b**) The CAD model generated for the East Village.

4.3.2 Wind data analysis

A wind rose, shown in Figure 4.5b, is used to show wind speed in different directions at 10 m above ground level. Where segment 1 to 12 in the figure are mean wind directions with 15 degree intervals. The frequency of mean wind speed in each direction is represented by the numbers 0 to 15000. The cumulative wind speed at various frequencies was averaged over a ten-year period from 2001–2010. This value was determined as 8 m/s and was used as a reference velocity throughout the simulation. The surface of the cylinder in the computational domain is divided into 12 segments based on wind data analysis, displaying various wind speeds in different directions. Six portions are designated as inlets in each simulation, while the remaining sections are assigned as outlets. The velocity data obtained from the UK Met Office for the closest weather station is used as the boundary condition at the computational domain's inlet. The wind rose in Figure 4.5b shows that velocity is prominent in the south-west (SW) direction, and it reaches its maximum at an angle of 240º. The inlet boundary is then defined in the range of SW $-$ 90 °< Inlet < SW + 90. This is shown schematically in Figure 4.5a. Half of the circle is specified as an inlet, while the other half is defined as an outflow, as can be seen. The inlet, outflow, top of the computational domain, building walls, and roof have the same boundary conditions as the validation case. The weather station data is provided for a height of 10 m. For all wind directions, the aerodynamic roughness length is set to 0.3, which is an estimated value for suburban or industrial locations [200, 201]. With an aerodynamic roughness length of 0.3 and a velocity of 8 m/s at a height of 10 m, the friction-free velocity is computed to be 1.078 m/s. This value of friction-free velocity is used in turbulent kinetic and dissipation energy for the inlet.

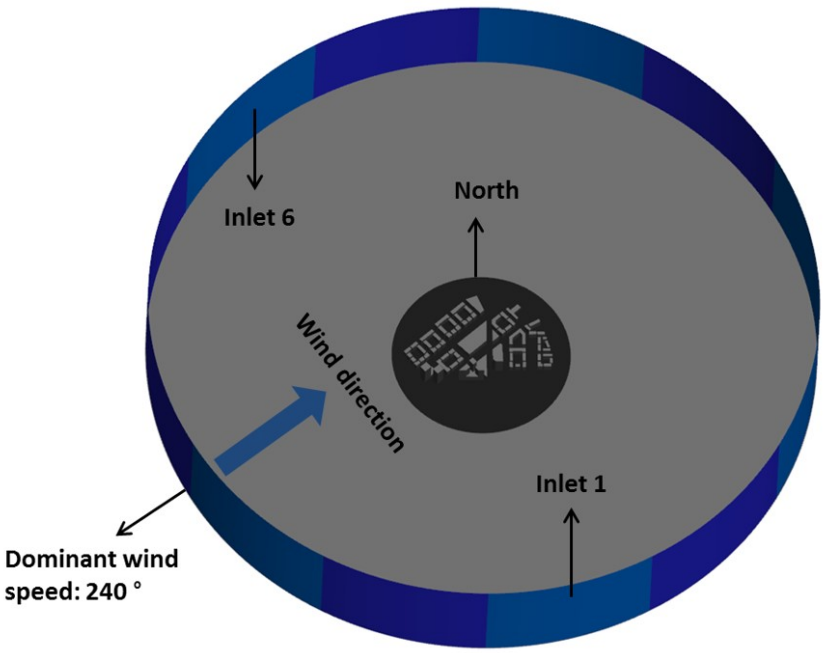

(**a**)

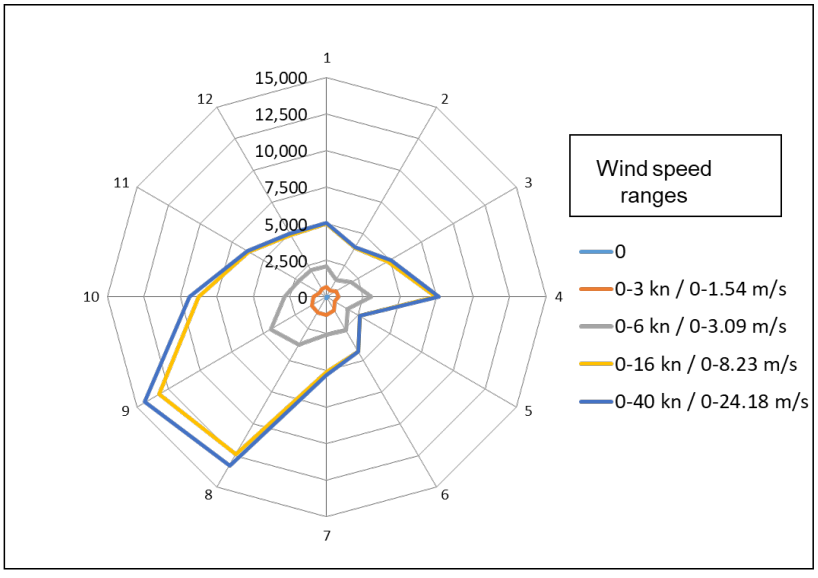

(**b**)

Figure 4.5: (**a**) Computational domain for East Village; (**b**) Wind data analysis.

4.4 Results

4.4.1 Preliminary remark

4.4.2 Test case 1

The results of the simulations are presented in terms of velocity profiles at the pedestrian level of 2 m in Figure 4.6.

The simulation results are for the case with the polyhedral mesh, using a prism layer thickness of 20% of the core cell size and the number of prism layers as 2. Polyhedral mesh produces more accurate results than tetrahedral mesh, according to the findings. The key reason for this is that each individual cell in a polyhedral mesh has many neighbours, allowing gradients to be well approximated [202]. In addition, faster convergence with fewer iteration can be achieved using polyhedral mesh. To create the core mesh, the polyhedral meshing model uses an arbitrary polyhedral cell shape which is created from an underlying tetrahedral mesh using a specific dualisation process [151]. This technique enhances mesh quality by reducing skewness. Furthermore, because more than one or two tetrahedral cells join to form polyhedral cells, a reduction in mesh count is always feasible, and thus the simulation time is also reduced. The results also show that changing the number of prism layers from 2 to 5 does not affect the simulation. So, to reduce the computational cost for a complex urban geometry it is reasonable to use 2 layers. These inputs indicate more accurate results as they fit the measurement data better. Simulation results using different turbulence models are fully converged and the residuals reach below 10^{-4}.

For comparing the results of this simulation quantitatively, 5 points within the building passages are taken along the wind direction, as shown in the inset of Figure 4.6.

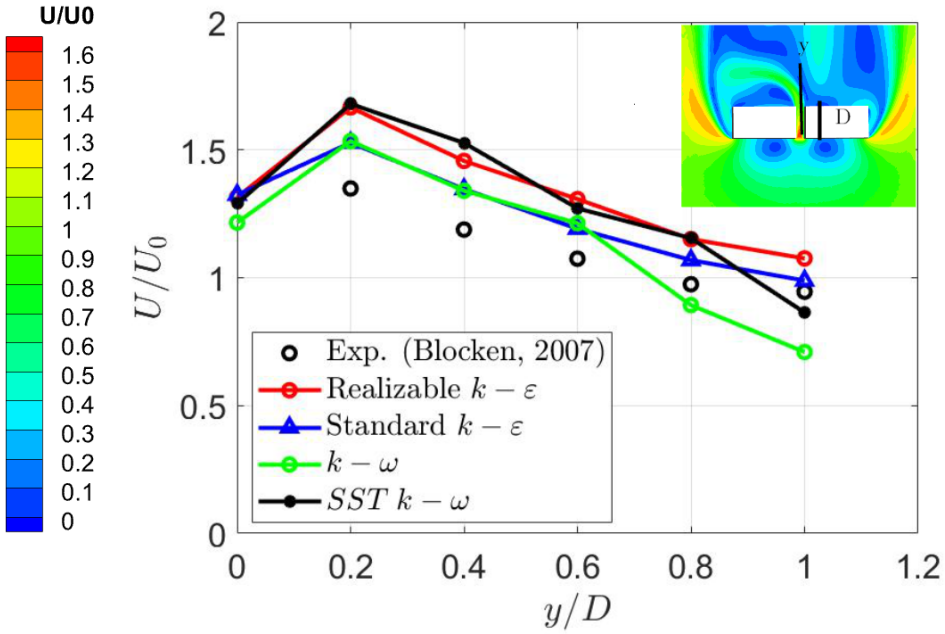

Figure 4.6: Comparison of amplification factors (u/u_0): u_0: 5.9 (m/s) using different turbulence model (same cell size); building width: 6 m.

It can be seen that overall, the standard k-ε model fits the experimental results better compared to other models. Nearly all models tend to over-predict the velocity. The standard and SST k-ω models tend to under-predict the velocity further downstream, therefore predicting a much steeper gradient in the velocity levels with respect to y/D. All the numerical settings used in this simple case study provide great insight for the much more complicated case of the East Village, which is presented below.

4.4.3 Test case 2

Colour contours of velocity at the pedestrian level of 2 m are shown in Figure 4.7. The area of high velocity is clearly observed from the velocity contours, which are due to corner effects as well as downwash and funnelling effects (this will be discussed further in conjunction with Figure 4.9).

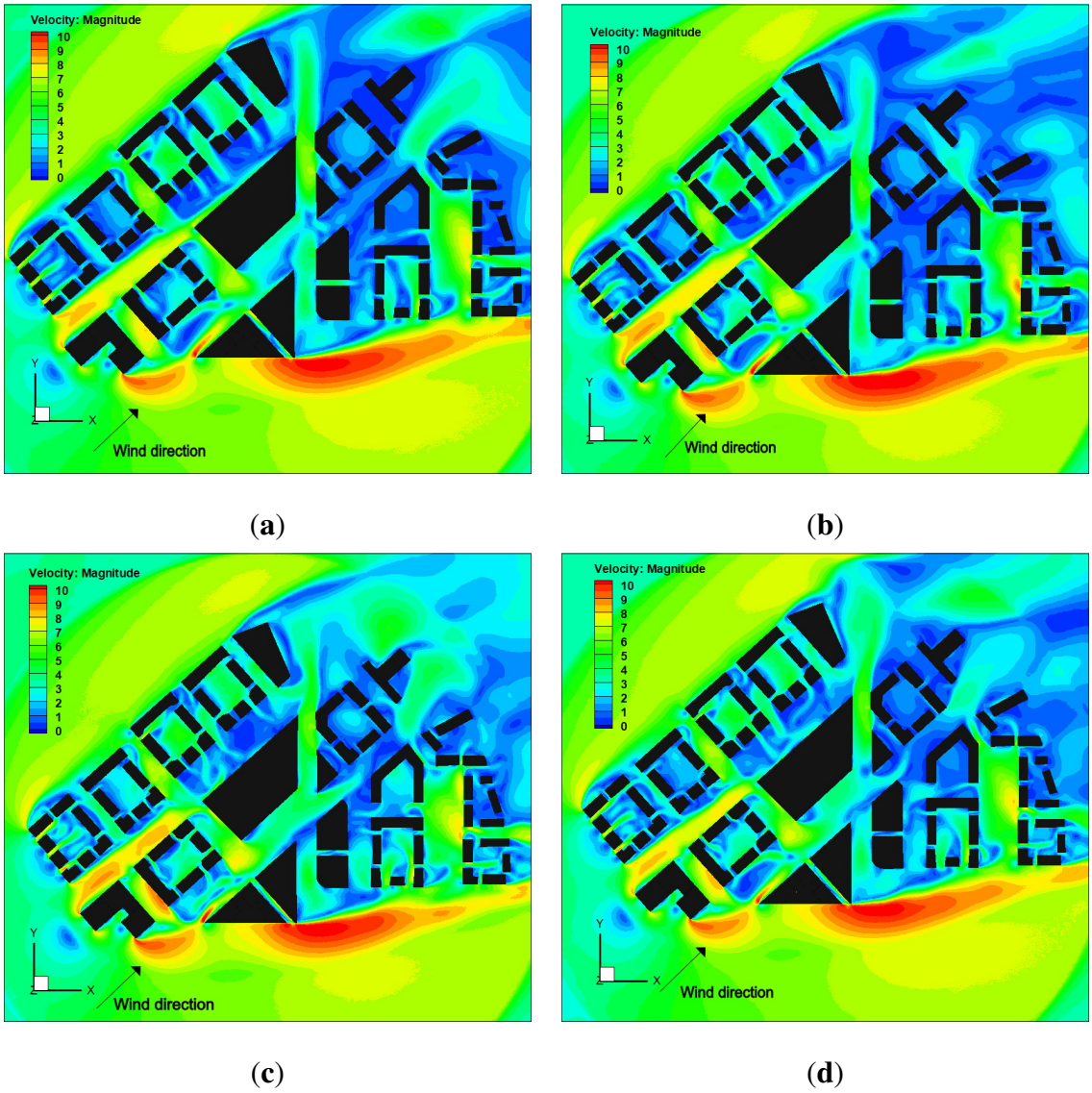

Figure 4.7: Contours of the velocity magnitude: (**a**) standard k-ε; (**b**) realizable k-ε; (**c**) k-ω; (**d**) SST k-ω.

Based on the velocity contours shown in Figure 4.7, no significant difference between different models can be observed. To further investigate this, the variation of the predicted velocity should be monitored at different heights. To do so, the velocity profiles across three vertical lines are shown in Figure 4.8 for different turbulence models.

Line 1 is located very close to buildings, just before the wind impinges on the bluff bodies. Along this line, all turbulence models show the most similar trends and the buildings behind them have similar heights. Line 2 is located in the area with the highest velocity magnitudes. The buildings in front of them have heights varying between 30 and 100 m. As can be observed from Figure 4.8b, velocity variation with height along line 2 and above the height of 30 m are increasingly similar with a very small variation for all models. Beyond the height of 30 m, the main obstacle is a tall structure and the results appear to exhibit the same trend for four turbulence models. Line 3 is located where the streamlines have passed the bluff bodies. From this line, it is clearly recognised that the k-ω does not obey the logarithmic trend as the velocity decreases up to the height of 30 m, and then it follows an increasing trend. In the work carried out by Tominaga et al. [203], which assessed the accuracy of various turbulence models around one high rise building, it was mentioned that SST k-ω underestimates the turbulent kinetic energy around buildings and as a result, flow separation is expected around the corners of the buildings. Overall, their finding indicated that k-ε models are more accurate in the prediction of flow around the buildings for both steady and unsteady state RANS simulations.

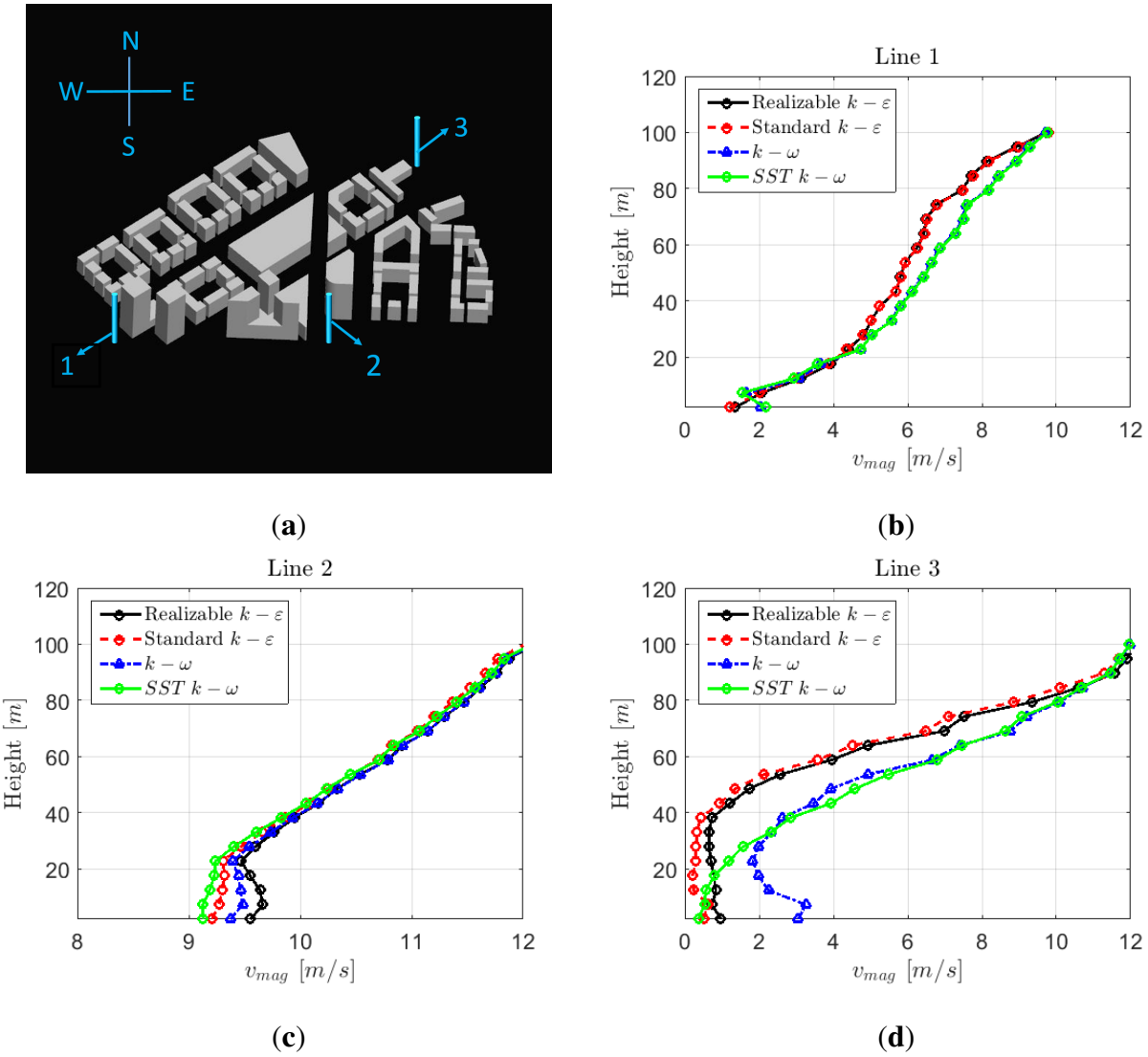

Figure 4.8: Comparison of various turbulent models at different heights for 3 distinct sections of the geometry: (**b**) line 1; (**c**) line 2; (**d**) line 3.

Despite indicating the velocity contours at pedestrian level, different wind patterns including corner, downwash and funnelling effects are also shown graphically in this section. In Figure 4.9a, the effect of interaction flow is illustrated. As has been mentioned by Blocken [191],

building influence scale is the factor used to determine different patterns of flow (e.g., resistance, interaction and isolated flow). This factor is calculated based on Equation (4.5).

$$S = (B_L B_s)^2 \tag{4.5}$$

where S is the building influence scale, and B_L and B_s refer to the larger and smaller dimensions of windward faces. In Figure 4.9a, the distance between buildings is 6 m and the ratio of width to building influence scale (W/S) is in the range of $0.125 < \text{W/S} < 1.25$, which is in the category of interaction flow. This factor indicates that the streams at the corner entrance separate and subsequently merge into one single stream. In addition, flow separation, corner and downwash effects are illustrated with streamlines in Figure 4.9b–d, representing areas of high velocity.

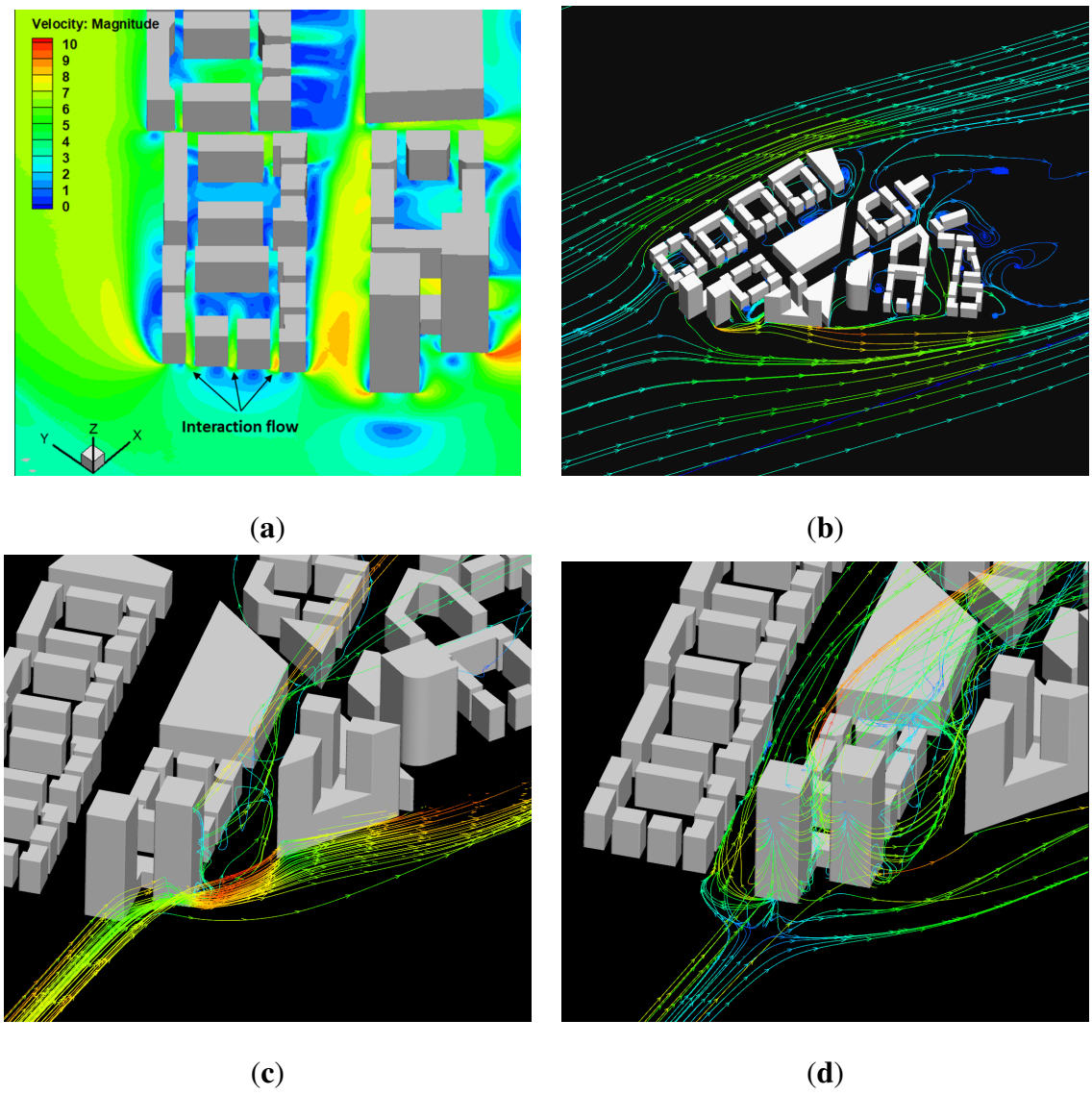

Figure 4.9: Velocity streamlines: (**a**) interaction flow; (**b**) flow separation; (**c**) corner effect; (**d**) downwash effect.

Streamlines in Figure 4.9b show the flow separation. Where the flow is separated from the surface of the buildings after hitting them it forms a recirculation zone after passing them. Streamlines in Figure 4.9c demonstrate the corner effect where the wind is accelerating around the corners of the buildings. The high-velocity area near the ground is due to corner effects

and this can lead to pedestrian discomfort, while calmer stagnation regions are at the sides of the buildings. In addition, high-velocity areas can occur due to the funnelling effect, where the flow accelerates through narrow passages between buildings. Figure 4.9d shows the downwash effect. When the wind strikes a tall building, it can flow above or around it and can be partly detached towards the ground, and its intensity depends on the height of buildings. This effect also amplifies the wind speed towards the ground and the pedestrian level.

It is worth noting that a standard wall function was used in Test cases 1 and 2 in contrast to the work of Blocken [191], where the wall function roughness was modified. However, further work is required to eliminate the effect of horizontal inhomogeneity such as using periodic boundary conditions instead of Richard and Hoxey [198], including boundary conditions for the velocity profile, turbulent kinetic and dissipation energy. A structured mesh could also improve the efficiency of CFD simulations. However, to reduce the computational cost, a structured mesh in the area of interest and unstructured far from buildings is more desirable. Unsteady-state RANS simulation for this case may also lead to improved prediction of the wind speed [203]. For reducing uncertainty, higher fidelity CFD techniques can be used (e.g., LES versus RANS) [169, 204]. However, using an expensive method of LES might not be very feasible for complex urban geometries such as the ones tested here due to significant computational cost [168]. Therefore, RANS still appears to be a preferred choice and a compromise between accuracy and cost in simulating complicated and/or large urban models [205].

It should also be mentioned that the turbulence model used is based on those found in STAR-CCM+ for high Reynolds numbers. Other works, however, have compared other variants of the k-ε model [206]. Santiago [207] and Tominaga [208] , for example, found that a RNG k-ε model agrees better with wind flow around buildings than standard k-ε and realizable k-ε models. In addition, Liu et al. [209] compared the wind velocity data from the RNG k-ε model and a wind tunnel experiment, finding a satisfactory agreement. Despite the fact that other research have found modified k-ε models to be more efficient, standard k-ε is the turbulence model used in other test cases in this thesis.

4.5 Summary

In this chapter, numerical simulations of the flow were conducted for two different test cases. first case was a simple model for sensitivity analysis and validation of the CFD methodology. Subsequently, the second case involved a large and detailed 3D model representing the East Village in the London Olympic Park. Various input parameters for mesh considered including two unstructured types of the mesh, ratio of prism layer thickness to core cell size and number of prism layers. According to the finding of this chapter, an unstructured polyhedral mesh produces more accurate results than a tetrahedral mesh with the same base size. Furthermore, increasing the number of prism layers from 2 to 5 had no significant effect on the results. To predict the velocity around buildings by using wall functions, there should be a reasonable growth rate between the outer prism layer and the first core cell. The results of the simulation of Test case 1 reveal that more accurate results are produced if the prism layer total thickness is 20% of the core cell size. The simulations of this study were performed using four different turbulence models including standard k-ε, realizable k-ε, standard k-ω and SST k-ω. Based on a comparison of simulation results and measurement data in Test case 1 and other references, including the work of Tominaga [203], it is believed that the simulation of wind on an urban scale works more effectively with the derivatives of the k-ε model.

Chapter 5

Effect of vegetation on flow field

5.1 Preliminary remark

Following the determination of areas of high velocities for Test case 2 from chapter 4, which result from the corner and downwash effects, appropriate tree planting is proposed to overcome these effects and mitigate the velocities for pedestrian comfort. As it was explained earlier in chapter 2, planting trees in urban areas contributes to urban heat island mitigation and can reduce energy use, wind speed and air pollution [141]. Urban trees are modelled through implicit and explicit approaches. Using implicit approaches, trees are considered in surface parameterisation with the value of aerodynamic roughness length z_0, which is applied in wall function. However, in the explicit approach, the aerodynamic effects of trees are modelled by adding source and sink terms to momentum, turbulent kinetic energy and turbulent dissipation energy [141]. Extra terms in the equation of turbulence kinetic and dissipation energy account for the enhanced production of turbulence, i.e., wake turbulence due to its smaller scale than shear turbulence, which is subjected to faster dissipation. Thus, vegetation acts as a net sink for turbulent kinetic energy [180, 210].

5.2 Test case 3: East Village of London Olympic Park with Vegetation

In the present work, trees were added to the case of the East Village with 14 different arrangements. The distance between trees, the proximity to building edges and the type of trees (evergreen or deciduous) will all affect the results. These critical parameters are shown in Figure 5.1. In this study, the trees were modelled using the explicit approach and were considered as porous media. The source and sink terms in the momentum, turbulent kinetic energy and turbulent dissipation energy are activated when the flow reaches the porous media zone according to Equations (3.39)–(3.41) in section 3.5 [180].

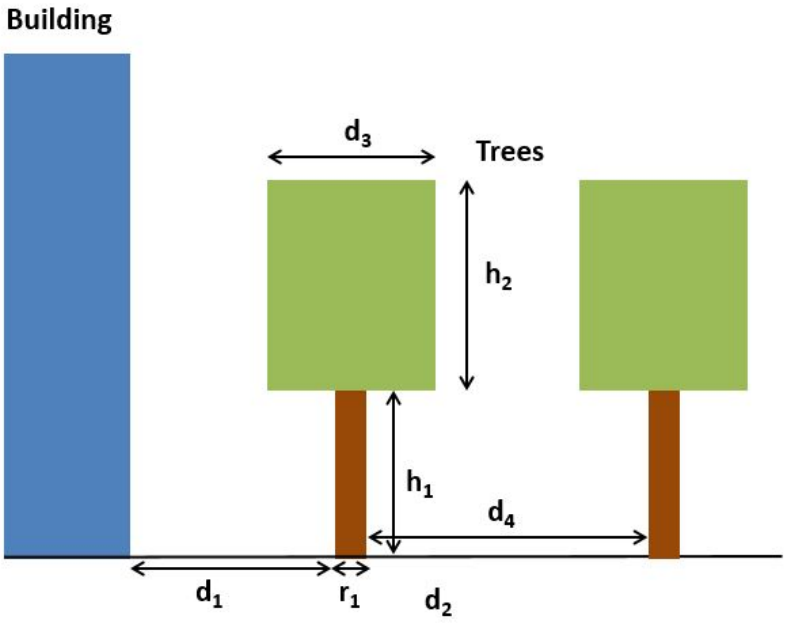

Figure 5.1: Critical parameters affecting the wind speed.

In this work, tree stems are not considered in the modelling due to their small size and thickness. The tree stem must be considered as a wall in case of existence, which creates a limitation for meshing. Only the tree crown is set as the porous media and it is elevated from the ground.

Depending on the type of tree and its age, tree height, crown width and crown height will vary. To estimate the elevation of porous media from the ground, the tree size must be estimated from empirical correlations. In this study, birch trees were chosen for wind mitigation, which are common trees in urban areas and in the UK [211] (Figure 5.2a). The crown height and width for this tree are estimated by Equations 5.1 and 5.2, respectively.

$$\text{Crownheight} = \exp(b_0 + b_1 HG + b_2 BHD + b_3 \text{treeage} + \beta + \beta_{pt}) \tag{5.1}$$

$$\text{Crownwidth} = \exp(c_0 + c_1 BHD + b_2 BHD + c_2 \text{treeage} + \gamma + \gamma_{pt}) \tag{5.2}$$

where *HG* and *BHD* refer to the height growth and the breast height diameter. The coefficients of empirical equations are taken from [211]. With the total tree height of 15 m, 2 mm/year height growth at the age of 20 years, the crown height and tree stem height are estimated as 9 m and 6 m, respectively. Applying these coefficients, the crown width is estimated around 4.5 m. Thus, in the CAD model, trees are elevated 6 m above the ground and the tree crown is shown as a rectangular cube with a height of 9 m and a width of 4.5 m in Figure 5.2. The required constant parameters to find out the tree dimensions are shown in Table 5.1.

Table 5.1: Constant parameters for estimation of the tree height and crown width.

Constants	b_0	b_1	b_2	b_3	c_0	c_1
Value	1.2603	0.0468	-0.0111	0.0060	0.554	0.1596
Constants	c_2	b	b_{pt}	γ	γ_{pt}	
Value	-0.0141	0.02226	4.0055	0.3156	0.8125	

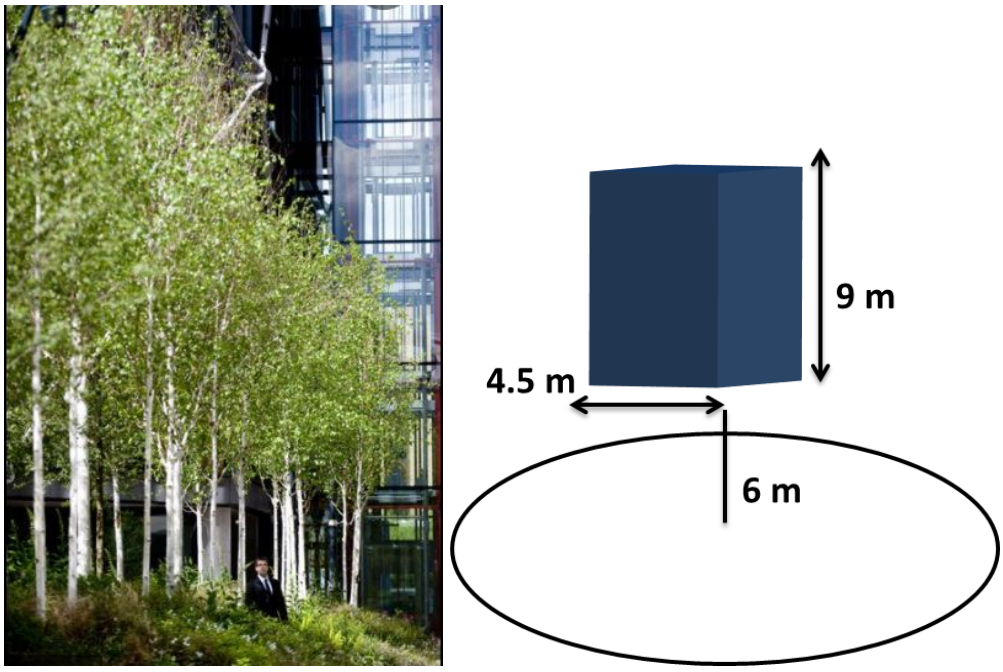

(**a**) (**b**)

Figure 5.2: (**a**) Birch trees; (**b**) Schematic of birch trees implemented in the CAD model.

The wind comfort level depends on individual activity [4]. For this reason, Table 5.2 defines the wind threshold for separate activities. The main objective of using vegetation around buildings is to eliminate A1 regions in the outer boundary of the model for pedestrian comfort, which is presented in Figure 5.3. In order to remove the A1 regions, which are uncomfortable for pedestrians walking and cycling, the different arrangement of trees with heights of 12 and 15 m are assessed in this test case. Many factors in tree modelling in urban simulations can affect wind mitigation. Examples include wind direction, tree type (e.g., deciduous, evergreen), tree age, stem height, tree height, crown height, crown width, diameter at breast height, distance between trees and distance of buildings to the trees [141, 180, 212]. Considering all these parameters simultaneously to find the optimised type of tree and arrangement is beyond the scope of this study. Thus our study deals with optimizing the arrangement of trees after tree selection (e.g., based on price, weather condition). Regions 1–3 in Figure 5.3 show the main areas in need of mitigation. Trees with a height of 15 m represent a birch type. The description

of different tree arrangements tested here is shown in Table 5.3. [3, 4].

Table 5.2: Lawson comfort scale.

Wind speed category	Threshold wind velocity [m/s]	Activity
A4	4	Uncomfortable for pedestrians in the vicinity of entrance door or sitting outside for long period of time.
A3	6	Uncomfortable for pedestrians standing or sitting for shorter periods of time.
A2	8	Uncomfortable for pedestrians 'leisure walking' e.g. strolling and sightseeing
A1	10	Uncomfortable for pedestrian walking quickly e.g. walking to a destination and cycling

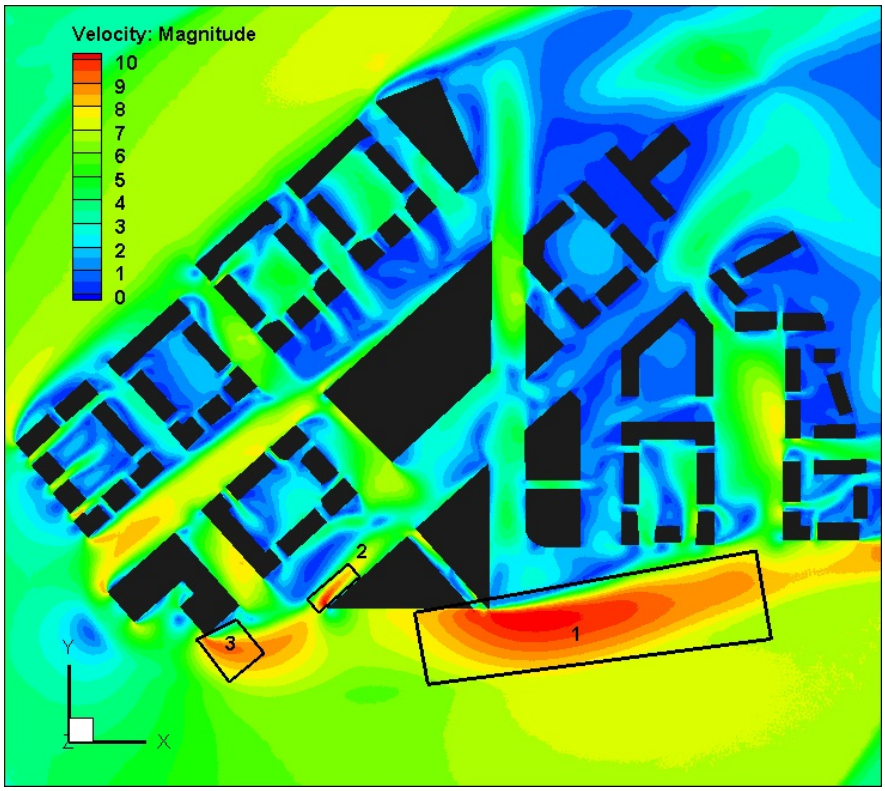

Figure 5.3: A1 region inside the boundary: Targeted area for wind speed mitigation.

Table 5.3: Description of different tree arrangements tested.

Case Number	Tree Height (H) [m]	Minimum Distance to Buildings	Distance to Other Trees	Arrangement
Arrangement 1	12	2/3H	2H	Individual trees
Arrangement 2	12	H/2	H	Individual trees
Arrangement 3	12	H/2	2H	Individual trees
Arrangement 4	12	H/4	H	Individual trees
Arrangement 5	15	H/2	2H	Individual trees
Arrangement 6	15	H/2	H	Individual trees
Arrangement 7	15	H/4	2H	Individual trees
Arrangement 8	15	H/4	H	Individual trees
Arrangement 9	15	H/4	Adjacent	Block
Arrangement 10	15	H/4	Adjacent	Block
Arrangement 11	15	H/4	Adjacent	Block
Arrangement 12	15	H/4	Adjacent	Block
Arrangement 13	15	H/4	H/4	Block
Arrangement 14	15	H/4	H/4	Block

5.3 Results

The velocity contours at the pedestrian level for the 12 m tree for different tree arrangements are shown in Figure 5.4 (arrangements 1–4). The crowns of these trees are modelled as a cube with 5 m width and 8 m height and are elevated 4 m above the ground. The tree crown is closer to the ground in comparison to birch trees (arrangements 5–8). By looking at Cases 1 to 4, it is evident that the A1 region is smaller when the distance between the trees is reduced. However, the minimum distance between trees and buildings is not large enough to overcome the corner acceleration that leads to the A1 region. The minimum gaps between trees and buildings for trees with a 12 m height are set as 3, 6 and 8 m. Changing the type of trees to one with a larger crown width and higher leaf area intensity can lead to improved performance.

The velocity contours for birch trees are shown in arrangements 5–8. By comparing arrangements 5 and 6, no significant difference can be observed, despite the trees in arrangement 6 being denser. The results suggest that the porous media that is closer to the ground works more effectively by comparing arrangements 2 and 6 for tree heights of 12 and 15 m. Both configurations have the same density for trees and the same minimum distance to buildings. Even though the crown height is bigger for the 15 m tree, due to the proximity of porous media to the ground, 12 m trees are more effective at decreasing the wind velocity. In general, 15 m trees work less effectively than 12 m trees for all the cases assessed here because the tree crown is located higher above the ground. In Figure 5.5, various blocks have been defined as a representation of adjacent trees, an approach which is very efficient in terms of computational time [180, 186]. By comparing 14 cases of wind mitigation in this study, it appears that tree arrangements from Cases 9 to 14 act more effectively in terms of wind velocity mitigation at the pedestrian level. However, to compare the effectiveness of arrangements 9 to 14, the area-weighted averages of velocity are taken for regions 1–3 and are presented in Table 5.4.

The results in Table 5.4 demonstrate that the most effective arrangement for wind speed reduction at the pedestrian level for region 1 is arrangement 14, leading to approximately 25% reduction. For regions 2 and 3, arrangement 12 leads to 66% and 3% reductions, respectively.

As can be observed from the results, in region 3, despite inserting blocks all around the buildings, the wind velocity cannot be decreased significantly. This suggests that in this region, other types of trees with perhaps wider crowns should be considered.

5.4 Summary

The impact of various tree arrangements on pedestrian comfort has been investigated in this chapter. The results of this section focus on the importance of trees height, their distance from buildings and other trees. Trees that are closer to the edge of the buildings are more efficient in decreasing wind speed when compared to alternative layouts evaluated in this chapter. Furthermore, the impact of tree age is demonstrated by the elevation of the tree crown from the ground. This illustrates that the crowns of younger trees are more effective at lowering wind speed since they are closer to the ground. The quantitative evaluation of several tree arrangements shows that with the optimised arrangement of trees in Test Case 3 using a specific type of trees (e.g., birch), the wind speed at the pedestrian level is reduced by 25% in region 1, 66% in region 2 and 3.5% in region 3.

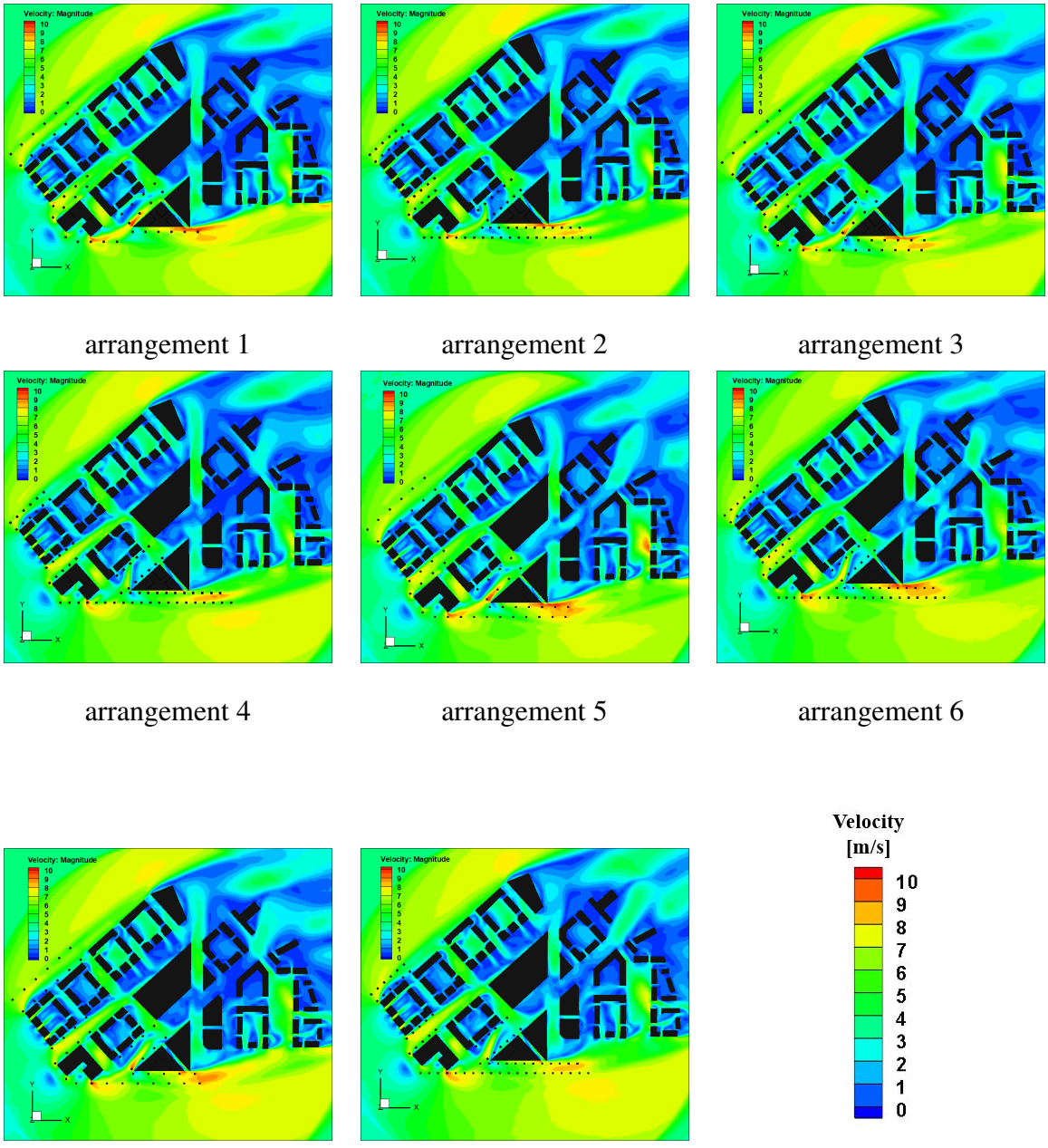

Figure 5.4: Velocity contours at the pedestrian level (2 m) with various tree arrangements (Arrangements 1–8).

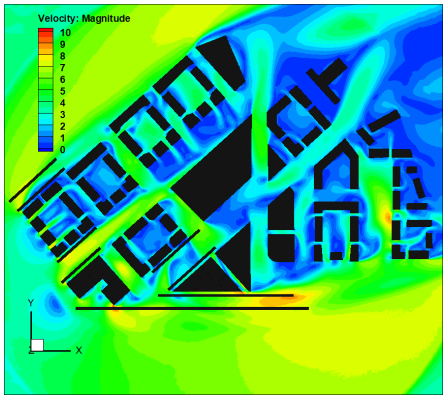

arrangement 9

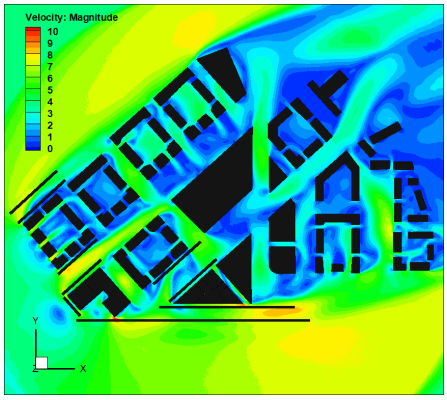

arrangement 10

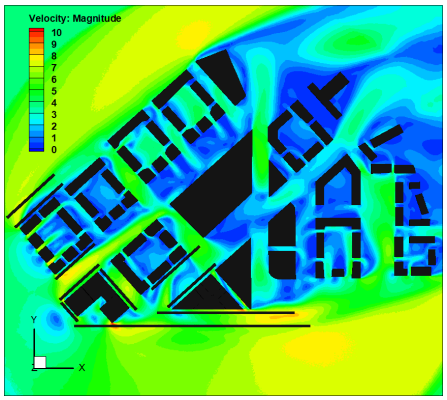

arrangement 11

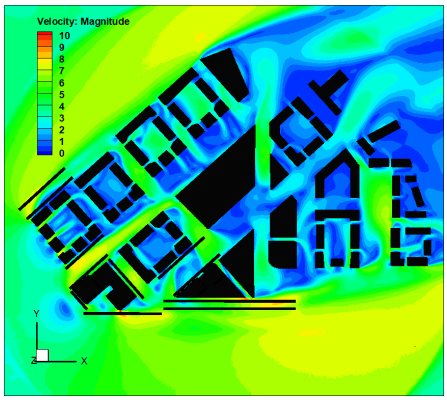

arrangement 12

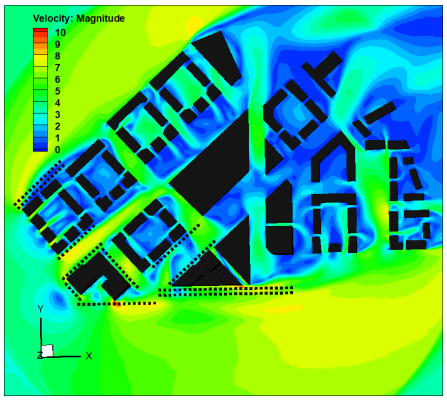

arrangement 13

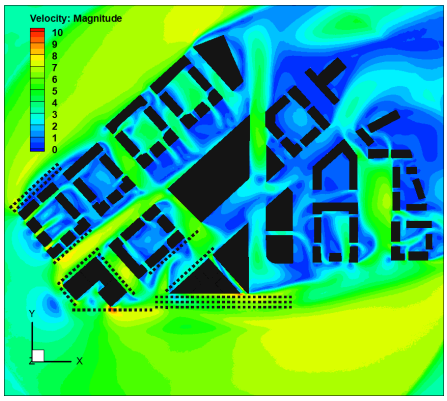

arrangement 14

Figure 5.5: Velocity contours at the pedestrian level (2 m) with various tree arrangements (Arrangements 9–14).

Table 5.4: Area weighted average of velocity for regions 1, 2 and 3.

Case Number	**Area weighted Average of Velocity (m/s)**		
	Region 1	**Region 2**	**Region 3**
East Village without trees	8.05	8.80	5.40
Arrangement 9	7.06	2.83	5.28
Arrangement 10	7.04	2.88	5.33
Arrangement 11	6.84	2.84	5.51
Arrangement 12	6.71	2.68	5.24
Arrangement 13	6.68	2.93	5.64
Arrangement 14	6.03	3.12	5.61

Chapter 6

Effect of vegetation on air quality, temperature and velocity

6.1 Preliminary remark

This chapter includes four case studies: Test cases 4, 5, 6 and 7. Table 6.1 summarises the descriptions of these case studies as well as their findings. A CFD analysis of street canyons with bottom heating is used in Test case 4. The current simulation has been compared to the work of Kim and Baik [179], as well as the wind tunnel data of Uehara et al. [213]. Test case 4 is used to validate Test cases 6 and 7, which assess various bottom heating circumstances. The effect of building roof greening on air quality in street canyons is investigated in Test case 5, which is a replication of Baik et al's study [101]. The concept of a pollution source term in street canyons that was used in this study is implemented for Test cases 6 and 7. Test case 6 represents the selected areas of East village (Figure 6.3) consisting of 7 buildings where the CFD analysis of wind around these buildings with bottom heating of 10 °C on air temperature, quality, and wind speed at the pedestrian level is assessed. Test case 7, on the other hand, is identical to Test case 6, except with the addition of one building. The comparison of Test case 6 and 7 data demonstrates how the addition of buildings can aggravate the UHI impact, degrade air quality, and create pedestrian discomfort. As a result, alternative mitigation approaches

are applied on this test case, as discussed in chapter 2. Mitigation methods which take into account the impact of vegetation with various layouts are green roofs, green walls and trees. The influence of trees on pedestrian wind speed has been assessed by Test case 3 in section 5.2, whereas their effect on air quality and temperature has been evaluated in this chapter. Furthermore, a parametric study is carried out to evaluate the impact of some key parameters on air temperature, pollution, and velocity at the pedestrian level. These parameters include wind speed (8 and 4 m/s at the reference height of 10 m), cooling intensity of the vegetation (250 and 500 W m^{-3}) and three cases where the streets have no bottom heating, bottom heating of 2 °C and 10 °C. Pollution is simulated as a form of passive scalar with an emission rate of 100 ppb s^{-1}, considering NO_2 as the pollutant.

Table 6.1: Evaluated case studies in this chapter.

Case number	Description of the case	Findings
Test case 4	2D idealised street canyons	Prediction of the air temperature
Test case 5	2D model representing 2 buildings in street canyon with the source of pollution	Prediction of the air temperature and pollutant concentration
Test case 6	3D model representing selected areas of East Village with 7 buildings	Prediction of the air temperature, pollutant concentration and velocity
Test case 7	3D model representing selected areas of East Village with 8 buildings	Prediction of the air temperature, pollutant concentration and velocity

6.2 Test case 4: Street canyon with bottom heating

In this section, a CFD model is used to predict the air temperature in idealised street canyons. The results of the present simulation are compared against wind tunnel data from Uehara et al. [213] and the simulation results of Baik et al. [90]. It is worth mentioning that this case study has also been validated by other studies [86, 214, 215].

6.2.1 Computational domain and mesh

In this case study, there are seven street canyons. The building's height, H, and width, W, are both 1 m, as illustrated in Figure 6.1.For the discretization of this 2D model, a structured (trimmed cell) mesh was used. Using a 0.02m cell size, with a stretching ratio of 1.2, approximately 420,000 rectangular elements were generated. The target street canyon with bottom heating is the middle canyon in Figure 6.1. Bottom heating is defined as the temperature difference between the ground's surface and the ambient air temperature and represents the effect of the sun warming the earth. The estimated normalised potential temperature and horizontal velocity are acquired at the centerline of the target street canyon.

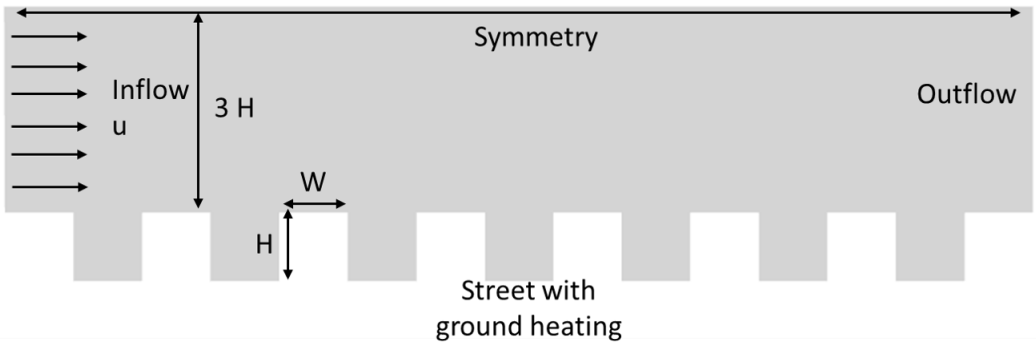

Figure 6.1: 7 street canyons with bottom heating in the middle street.

6.2.2 Governing equations and boundary conditions

In this case study, the temperature and velocity variations are computed using coupled flow and energy equations. The flow models are based on the RANS equations and standard k-ε turbulence model, as described in in Chapters 4 and 5. The segregated fluid temperature energy model is employed in this simulation. The energy equation is solved using the Segregated Fluid model in STARCCM+, with temperature as the solution variable. The equation of state is then used to calculate enthalpy from temperature [151]. The wind speed and temperature at the boundaries are given based on the bulk Richardson number (Rb) which is defined by equation

6.1.

$$Rb = gH(T_a - T_{g)}/(T_a + 273)u_h^2 \tag{6.1}$$

where g is the gravitational acceleration, H denotes building height, T_a and T_g stand for the ambient air and the ground temperature respectively. The velocity at the building height is denoted by u_h. The simulated case has a bulk Richardson number of -0.27 and a ground heating of 2 °C. Wind speed at the inlet is set 0.5 m/s.. The ambient air temperature at the inlet and outlet set as 20 °C. The outflow boundary has zero static pressure and the top of domain is symmetric. Table 6.2 represents a summary of the boundary conditions for Test case 4.

Table 6.2: Boundary conditions for Test case 4

Boundary conditions	**Value/Definition**
Inflow wind speed [m/s]	0.5
Width of street canyons [m]	1
Height of buildings [m]	1
Air temperature [°C]	20
Ground temperature [°C]	22
Richardson number	-0.27
Outflow	Zero static pressure
Top of the domain	Symmetry

6.3 Test case 5: Street canyon with the source of pollution

The model in this section is used to predict air temperature and pollutant concentration in the street canyon surrounded by two buildings. The results of the present simulation is compared against the simulation results by Baik et al. [101]. The street canyon is simulated with the bottom heating of 6 °C. The green roof is applied on building 1 in Figure 6.2 and is not shown as a vegetation block, but as a wall with a 2 °C cooling intensity. In addition, the traffic emission was modelled using the passive scalar model and is explained in section 6.3.2.

6.3.1 Computational domain and mesh

Figure 6.2 shows the 2D computational domain and mesh for this test case. The height of the buildings represented as wall 1 and 2 in this figure, as well as the width of the street canyon, are 20 m. The computational domain is 50 m long in the x direction, which means that roof 1 and roof 2 are 20 and 10 m wide respectively. The computational domain is 60.8 m tall. For this case study, this dimension was chosen to be compatible with experimental data. Because of the geometry's simplicity, a structured grid was employed to discretize the domain, as in the preceding section. The domain is split into two parts: upper and lower. The cell size in the lower domain, which is shown in a darker colour in Figure 6.2, is 0.025 m, whereas the cell size in the upper domain is 2.5 m. Around 100000 trimmed cells were generated using these values.

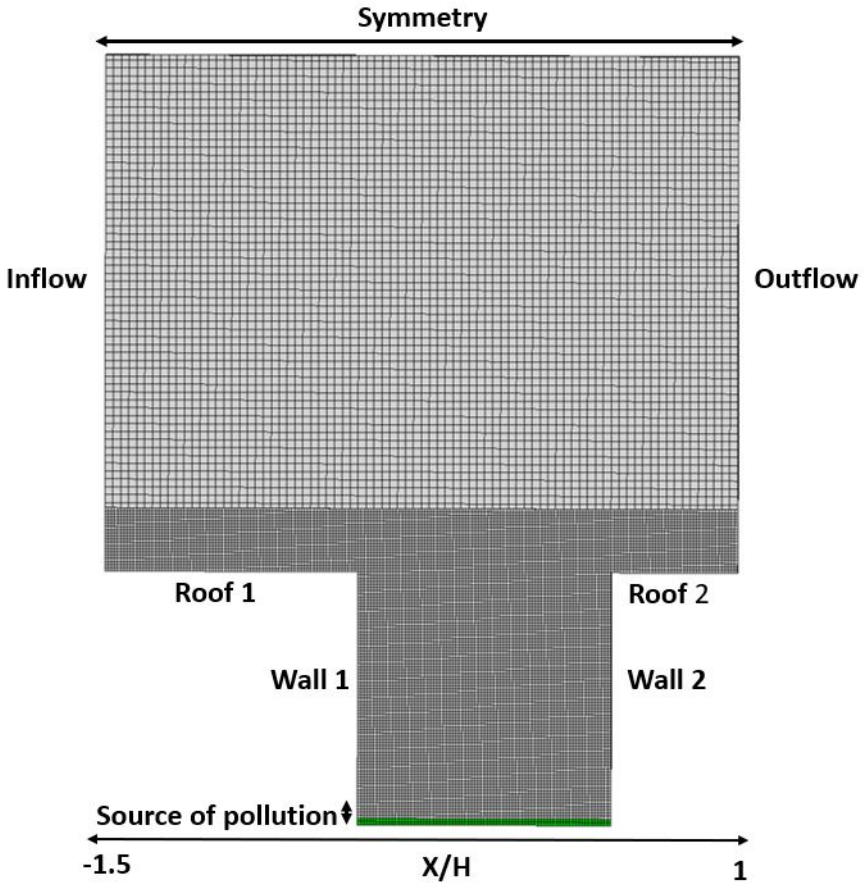

Figure 6.2: Street canyon with pollution.

6.3.2 Governing equations and boundary conditions

The flow and energy equations included in the CFD simulations of this test case are the same as those for Test case 4 in section 6.2.2. To model traffic emissions at the bottom of the street canyon, additional equations are required. A passive scalar model is used to model pollution [96, 189]. The mathematical equations for this model, as well as constants and model parameters such as the turbulent Schmidt number and turbulent diffusivity, are detailed in chapter 3 in section 3.6. Figure 6.2 shows the exact location for applying the pollution source term, which is from the ground up to a height of 0.5 m. Regarding NO_2 as a pollutant, the emission rate is 100 ppb s^{-1}. For this test case, the CFD simulations were run in unsteady state mode and integrated for 2 hours with a time step of 0.1 s. For the first 30 minutes, there is no traffic or pollution, and the source term is active from t=30 minutes to t=2 hours. he initial air temperature is fixed at the 30 °C. The temperature at the ground, wall 1, wall 2 and roof 2 are also set as 30 °C. The temperature at roof 1 is given as 28 °C to represent green roofs with cooling intensity of 2 °C. The inflow wind profile is logarithmic with wind speed of 2 m/s at the height of buildings. The outflow has a zero static pressure, and the top of the domain has a symmetric boundary. Table 6.3 represents a summary of the boundary conditions.

Table 6.3: Boundary conditions for Test case 5

Boundary conditions	**Value/Definition**
Air temperature [°C]	30
Temperature at roof 1 [°C]	28
Pollution's emission rate [ppb s^{-1}]	100
Inflow	Logarithmic velocity with the wind speed of 2 m/s at the height of 20 m
Outflow	Zero static pressure
Top of the domain	Symmetry

6.4 Test cases 6 and 7: Selected areas of East Village

In this section, areas of East Village from Figure 4.4 are selected and presented in Figure 6.3 and 6.4. Test case 6 is represented by the first, whereas Test case 7 is represented by the latter. Test case 6 consists of 7 buildings, while Test case 7 is the same as Test case 6 but with one additional building. For these test cases, CFD simulations of flow, energy, and pollution are conducted. The comparison between these two scenarios shows how adding a building to an urban design can increase UHI, deteriorate air quality, and create pedestrian discomfort. As a result, mitigation solutions to counteract these effects must be provided as buildings are added. As a result, the main focus of this section is on adding vegetation to Test case 7. The influence of vegetation in the form of trees for pedestrian comfort was clearly established in chapter 4. Therefore this chapter will focus on their impact on air temperature and pollution dispersion in urban areas. Furthermore, the impact of vegetation in other forms on building faç, such as green roofs and green walls, on air quality, temperature, and velocity in various conditions is compared. The efficacy of different mitigation measures is quantified and compared in terms of area- weighted average of temperature, pollutant concentration and velocity magnitude.

6.4.1 Computational domain and mesh

The computational domain for all test cases in this section is the same size as in Figure 4.4 for East Village. Building heights for Test case 6 range from 30 to 80 m, while those for Test case 7 range from 30 to 102 m. In this part of East Village, the additional building in Test case 7 is the tallest building. In Test case 6, there is no vegetation, however in Test case 7, there are numerous types of vegetation that are defined in Table 6.4.

Table 6.4: Test case 7 with various forms of vegetation.

Case number	**Description**
Test case 7-a	Without vegetation
Test case 7-b	With green roofs
Test case 7-c	With green walls
Test case 7-d	With trees
Test case 7-e	With combination of green roofs and green wall
Test case 7-f	With combination of green roofs and trees
Test case 7-g	With combination of green roofs and more trees
Test case 7-h	With combination of green roofs and more trees: trees 2 m closer to the ground
Test case 7-i	With targeted combination of green walls and trees
Test case 7-j	With targeted combination of green walls and trees

The size, type and location of trees are chosen based on the optimal layout of trees in chapter 5. The thickness of green walls and roofs is 1 m. Green roofs and green walls are represented in this study by a block with a thickness of 1 m, as opposed to Figure 2.7, where green roofs contain numerous layers. According to Figure 5.2, the birch trees are elevated 6 m above the ground, thus the green walls are similarly lifted 6 m. In Test cases 7a and 7b, green walls and roofs are found on all of the building surfaces which are depicted by numbers 2 and 3 in in Figure 6.4. Apart from the influence of individual vegetations, the efficacy of combination strategies was also assessed. Figure 6.6 from cases e-h shows the combination of greenery. Cases 'g' and 'h' have similar arrangement while trees in case 'h' are 2 m closer to the ground. The difference between cases 'f' and 'g' are more observable in Figure 6.7. Cases 'i' and 'j' are targeted mitigation choices, and the reason for this configuration will be detailed in section 6.5.6.

The domain is discretised, and the computational mesh is the same size as in Test case 3. As demonstrated in Figure 6.5, a thin mesh with two layers was adopted for meshing green roofs

and green walls.

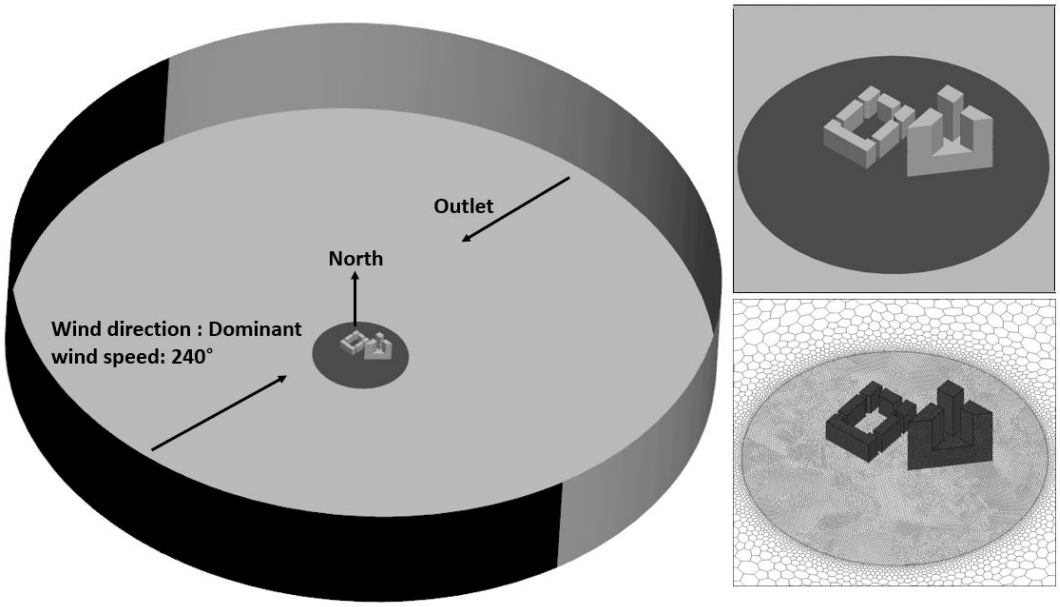

Figure 6.3: Computational domain for Test case 6.

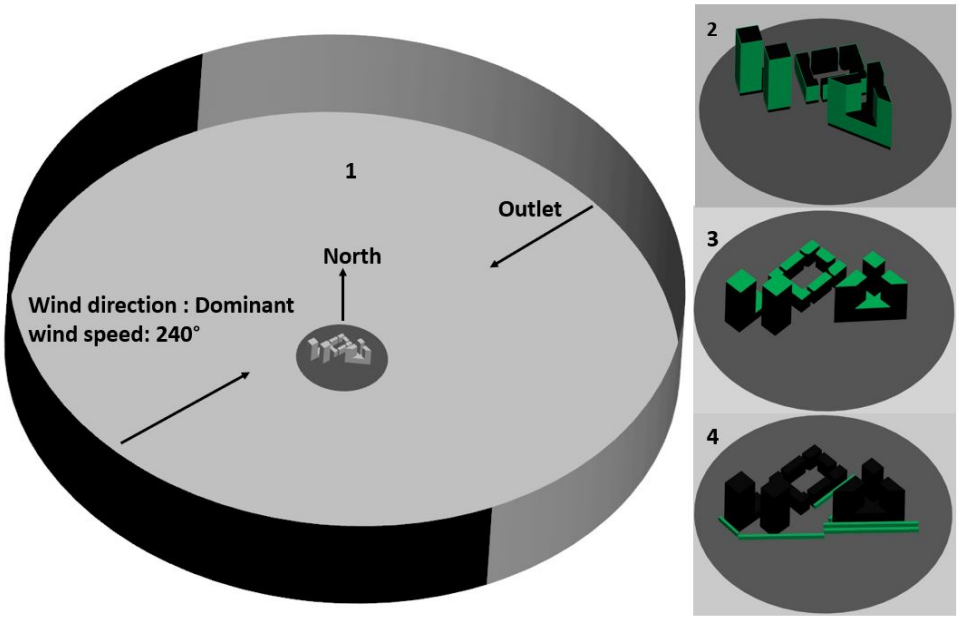

Figure 6.4: Computational domain with green wall, green roof and trees for Test case 7.

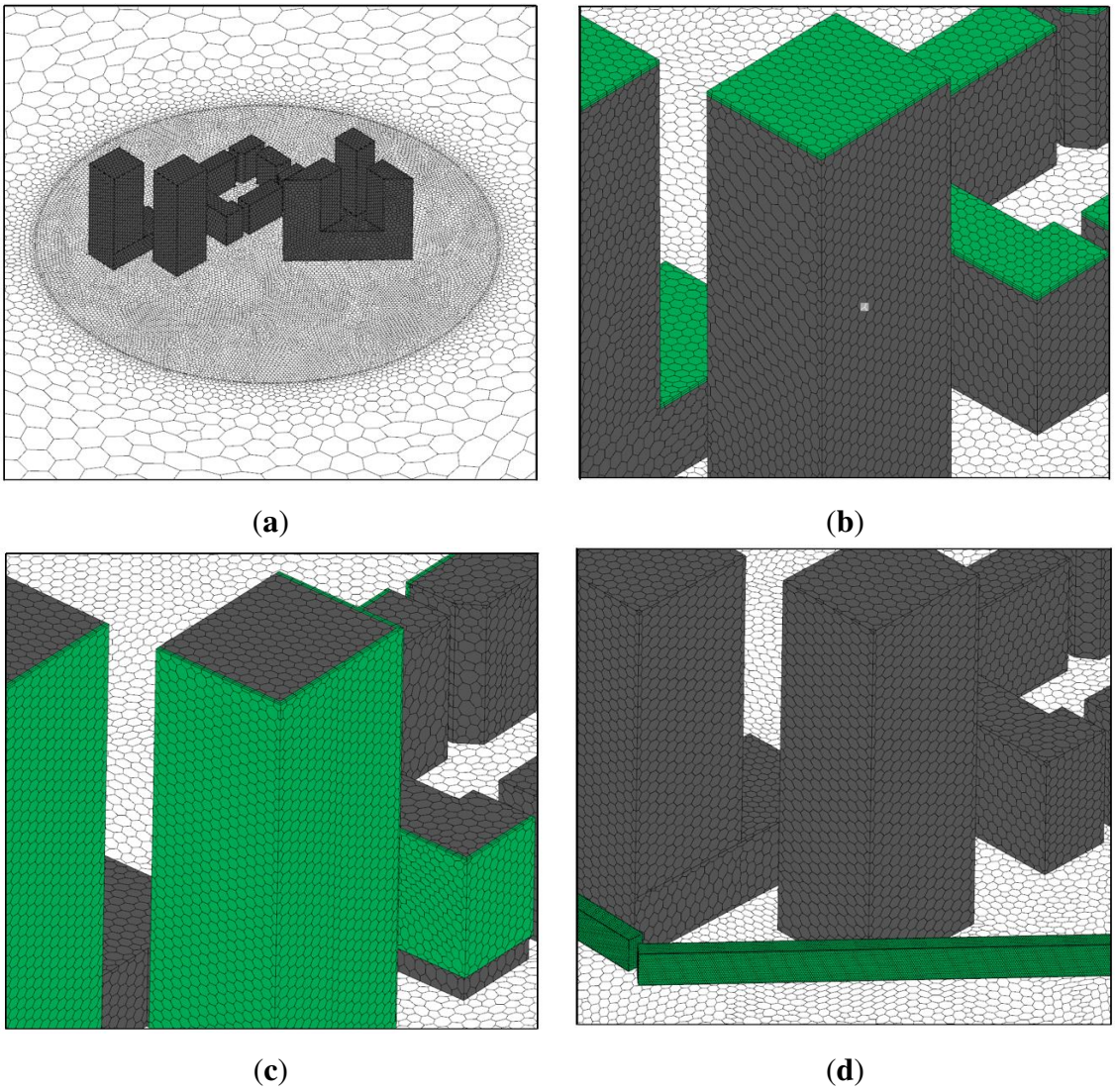

Figure 6.5: Computational mesh for Test case 7: (**a**) without vegetation; (**b**) with green roofs; (**c**) with green walls; (**d**) with trees.

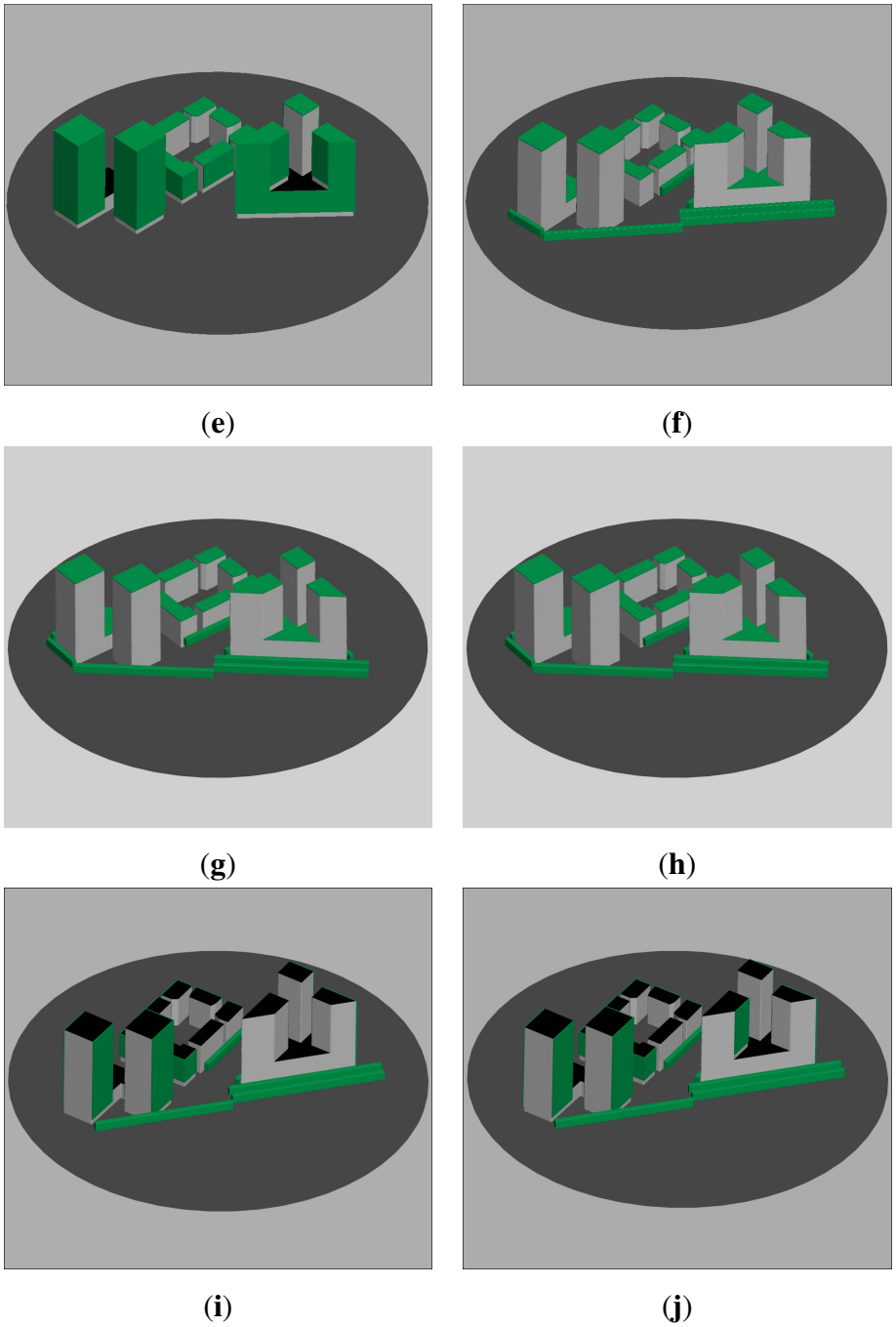

(**e**) (**f**)

(**g**) (**h**)

(**i**) (**j**)

Figure 6.6: Geometry for Test case 7: description of sub-figures can be found in Table 6.4.

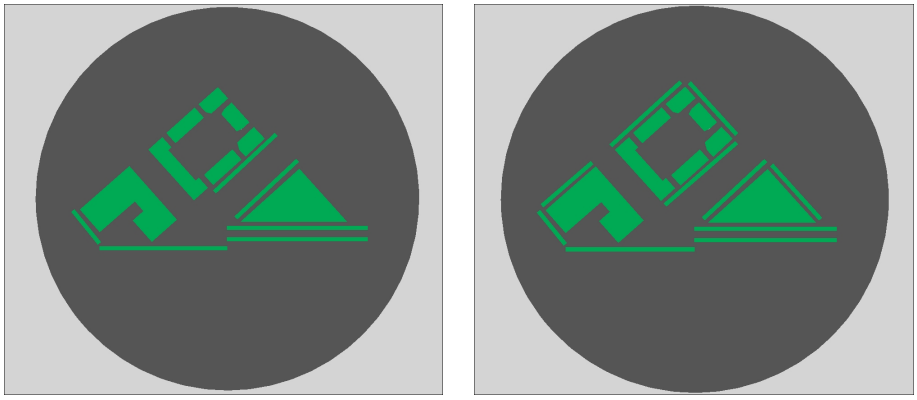

(**f**) (**h**)

Figure 6.7: Geometry for Test case 7: (**f**) with combination of green roofs and trees; (**h**) with combination of green roofs and more trees.

6.4.2 Governing equations and boundary conditions

The flow equations and boundary conditions are identical to those in Test case 3. The energy and pollution equations are coupled in the same way as in Test cases 4 and 5. Heat conduction is neglected, and the walls are considered thin. The simulations are all run in steady state mode in order to maintain consistency with the preceding chapters. As noted in Chapter 4, unsteady-state simulations may improve wind speed prediction [203], however the author employed steady state simulations to lower the computing cost for a complex urban layout. The flow and surface roughness boundary conditions are the same as in Test case 2. For all test situations, the air temperature is set to 20 °C. Different ground temperatures were used to generate various heating intensities, which represents as bottom heating, the difference between air and ground temperatures. The earth is warmed by the sun, which is represented by bottom heating.

To evaluate the effect of vegetations (green roofs, green walls and trees) the source terms are added to the equations of momentum, turbulent kinetic energy and energy dissipation. In chapter 3 and section 3.5, these equations and parameters are described in depth.

The exact location of pollution is the internal circular subdomain in Figure 6.4 up to the height

of 1 m. Different scenarios are investigated in order to assess the impact of various types of vegetation under different conditions. These are as follows in Table 6.5

Table 6.5: Different scenarios for Test case 7

	Bottom heating [°C]	**Cooling intensity [W m^{-3}]**	**Wind speed at the height of 10 m: [m/s]**
Scenario 1	0	250	8
Scenario 2	2	250	8
Scenario 3	10	250	8
Scenario 4	10	500	8
Scenario 5	10	250	4

6.5 Results

6.5.1 Test case 4

The results of this test case consist of the normalised temperature and velocity distributions in the middle of the street canyon. As shown in Figure 6.8, the accuracy of this model is validated by Uehara's experimental work [213] and the numerical study conducted by Baik et al. [90]. The estimated normalised temperature correlates well with the wind tunnel study, as shown in this figure. Furthermore, when compared to the other simulation, it is obvious that the calculated temperature near the ground is very similar to the measured data. Near the ground, the normalised velocity is overestimated, while the normalised velocity derived by this model matched the wind tunnel data better than the simulation results, especially at heights beyond the roof level (Z/H>1). Because of changes in simulated settings and experimental setup, the results of this simulation and the wind tunnel data may differ. For example, no roughness was applied to the ground when roughness elements were present in the experimental setup. Moreover, a 3D configuration was employed in the wind tunnel experiment, with buildings displayed

as blocks, but the model developed in this study was in 2D. Additionally, the Richardson number in the experiment is -0.21, whereas it is -0.27 in this work. Despite a few minor differences, the overall findings closely matched the wind tunnel data. Based on the results of this validation study, the same strategy for modelling of energy in urban areas with bottom heating will be used in the subsequent sections of this chapter for Test cases 6 and 7.

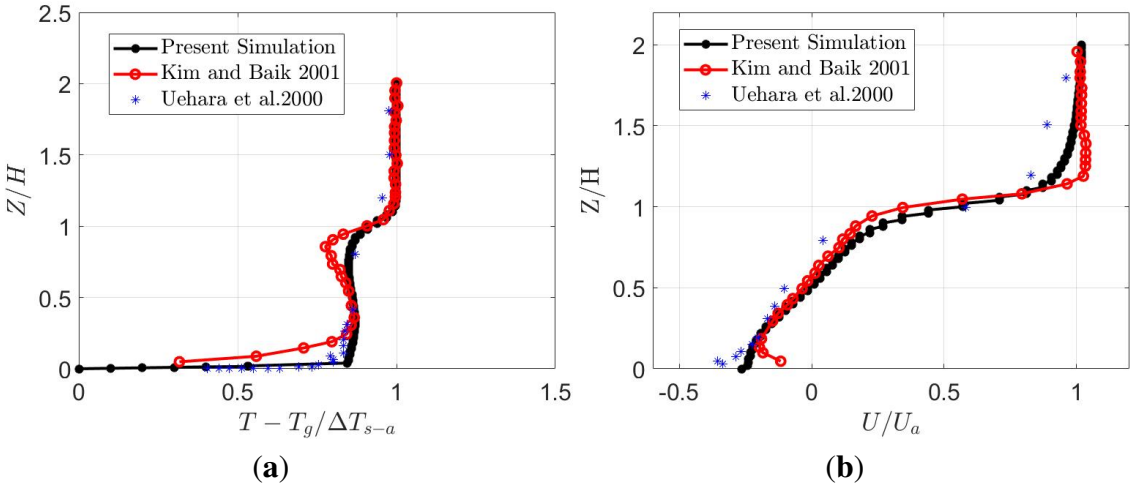

Figure 6.8: Variation of normalized velocity and temperature with the height in the middle of target street canyon with bottom heating (**a**) normalized temperature, (**b**) normalized velocity.

6.5.2 Test case 5

Figure 6.9 illustrates the findings of this test case, which include streamlines of velocity, pollutants, and temperature. The pollution streamlines are shown up to 1000 ppb with 100 ppb interval in Figures 6.9a and 6.9b. The temperature variations are represented in Figures 6.9e 6.9f for the presented simulation and Baik et al's study [101]. This demonstrates the cool air distribution in the street canyon. The rotating vortex in the street canyon is depicted in Figures 6.9c and 6.9d.

There are some discrepancies in the streamlines between the current simulation and Baik et

al's validation scenario, despite the fact that the variation of pollutant concentration and temperature are similar in both. The differences between the current simulation and Baik et al's study could be related to a variety of factors. For example, in Baik et al's study, the applied turbulence model is RNG k-ε, however in our simulation, the standard k-ε model was used. The value of the turbulent Schmidt number varies depending on the type of turbulence model, as indicated in section 3.6. The applied value for turbulent Schmidt number was not mentioned in Baik et al's paper. Because the standard k-ε model has the greatest performance in CFD modelling of urban microclimate among the evaluated models (see chapter 4), it is used throughout this work for consistency. Furthermore, this study used a 2D simulation as opposed to Baik et al's work, which used a 3D domain to simulate temperature and pollutants in the street canyon. Furthermore, the precise value of the aerodynamic roughness length was not provided, which could be another cause of discrepancy when comparing two simulations. Additionally, in the current simulation, a cooling intensity of 2 °C is applied to the roof, but in Baik et al's study, this value is applied to 0.25 m above the roof level. Also, the results of this simulation are compared against another simulation rather than field or wind tunnel data. As a result, the minor discrepancy between two simulations can be justified. Despite a few small changes, the findings were nearly identical to Baik et al's. Based on the findings of this validation research, the same technique for modelling pollution in urban areas will be employed for Test cases 6 and 7 in the following sections of this chapter.

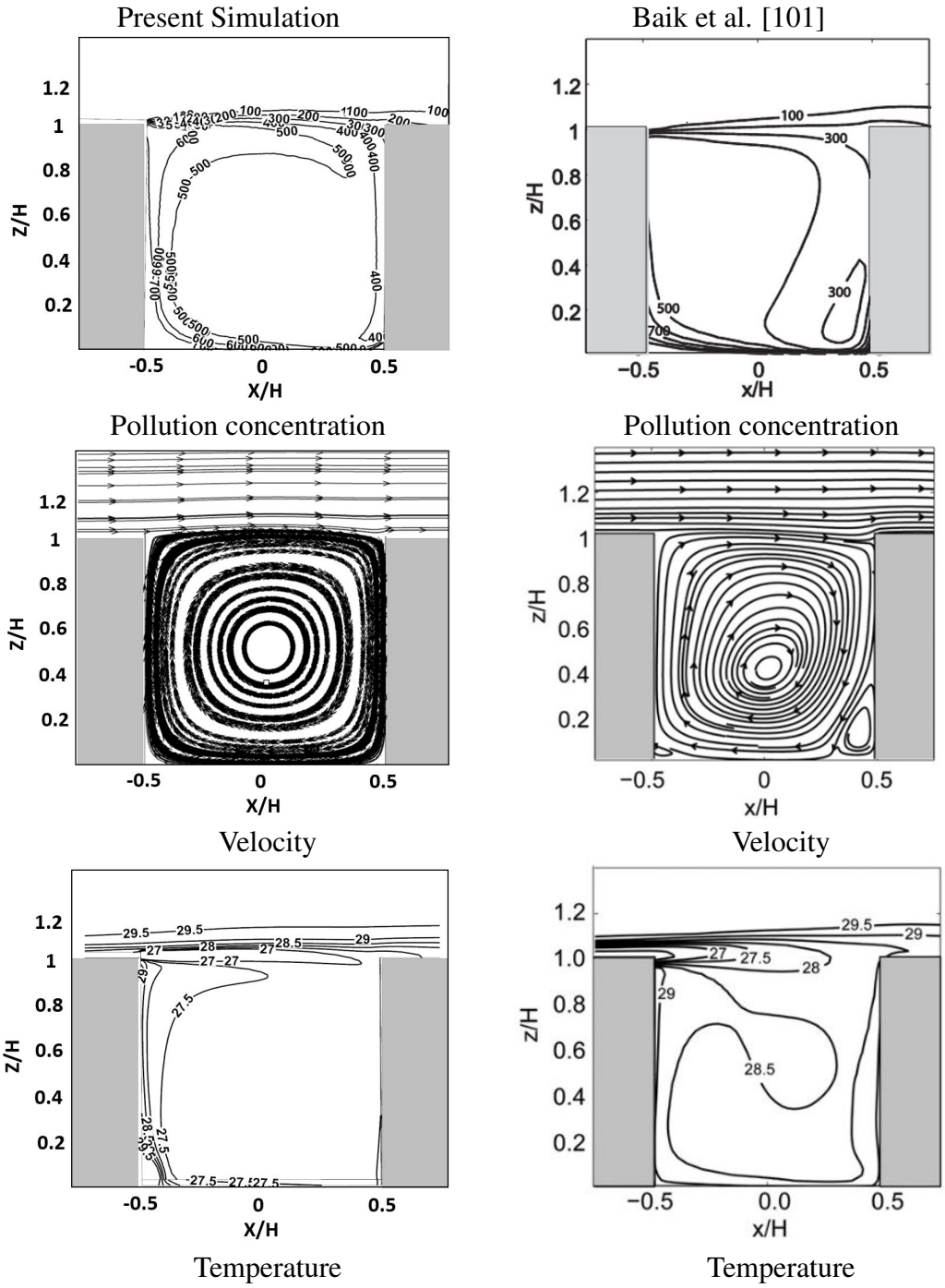

Figure 6.9: Variation of pollution, velocity and temperature in the middle of the canyon with height:

6.5.3 Test cases 6 and 7 without vegetation

The simulation conditions for the cases in this section are based on scenario 3 in section 6.4.2, with a bottom heating temperature of 10 °C, cooling intensity of 250 W m^{-3} and an inlet wind speed of 8 m/s.

The results of this section consist of contours of temperature, pollution and velocity at the pedestrian level for Test cases 6 and 7 as shown in Figure 6.10. In addition, the area weighted average of these variables is taken in three regions of interest, S1, S2, and S3, as shown in Figure 6.20. S1 is the largest region and it contains all of the buildings. S2 is the street that is surrounded by all of the buildings and S3 is behind building 2. S1, S2 and S3 have surface areas of 4.4 km^2, 4500 m^2 and 640 m^2 respectively. Based on the results of the following sections, these regions were identified as areas of interest. By comparing the contours of the left and right sides of Figure 6.10 , it is evident that adding a 102 m high-rise building in the direction of the wind can increase the UHI impact, degrade air quality, and create pedestrian discomfort. The results of area weighted averages for this section are provided in Tables 6.6, 6.7 and 6.8 at the end of this chapter. In all of these tables, Test case 7-a refers to the Test case 7 without vegetation, which is the section's evaluated case. The results showed that adding building 1 to Test case 6 increased the average temperature in the S1, S2, and S3 regions by 0.32 °C, 0.13 °C, and 0.22 °C, respectively, while increasing the pollutant concentrations by 117, 93, and 132 ppb in the same areas. The S3 region has the lowest velocity magnitude, which is the recirculation zone, and causes the most pollution because pollutants are trapped and do not move in low velocity areas. The average velocity in the large S1 region also increased by 6%. Although this is only a marginal increase, the addition of a building resulted in high-velocity areas in some regions due to corner and downwash effect. When comparing Test Cases 6 and 7, it appears that the red areas which cause pedestrian discomfort (see chapter 5, Table 5.2) have increased in size dramatically.

The quantitative comparison of these two scenarios necessitates the use of mitigation methods (e.g. vegetations) on Test case 7 to offset the increases in temperature, pollutant concentration, and velocity magnitude. In the next sections, the efficacy of different approaches under various

conditions is discussed.

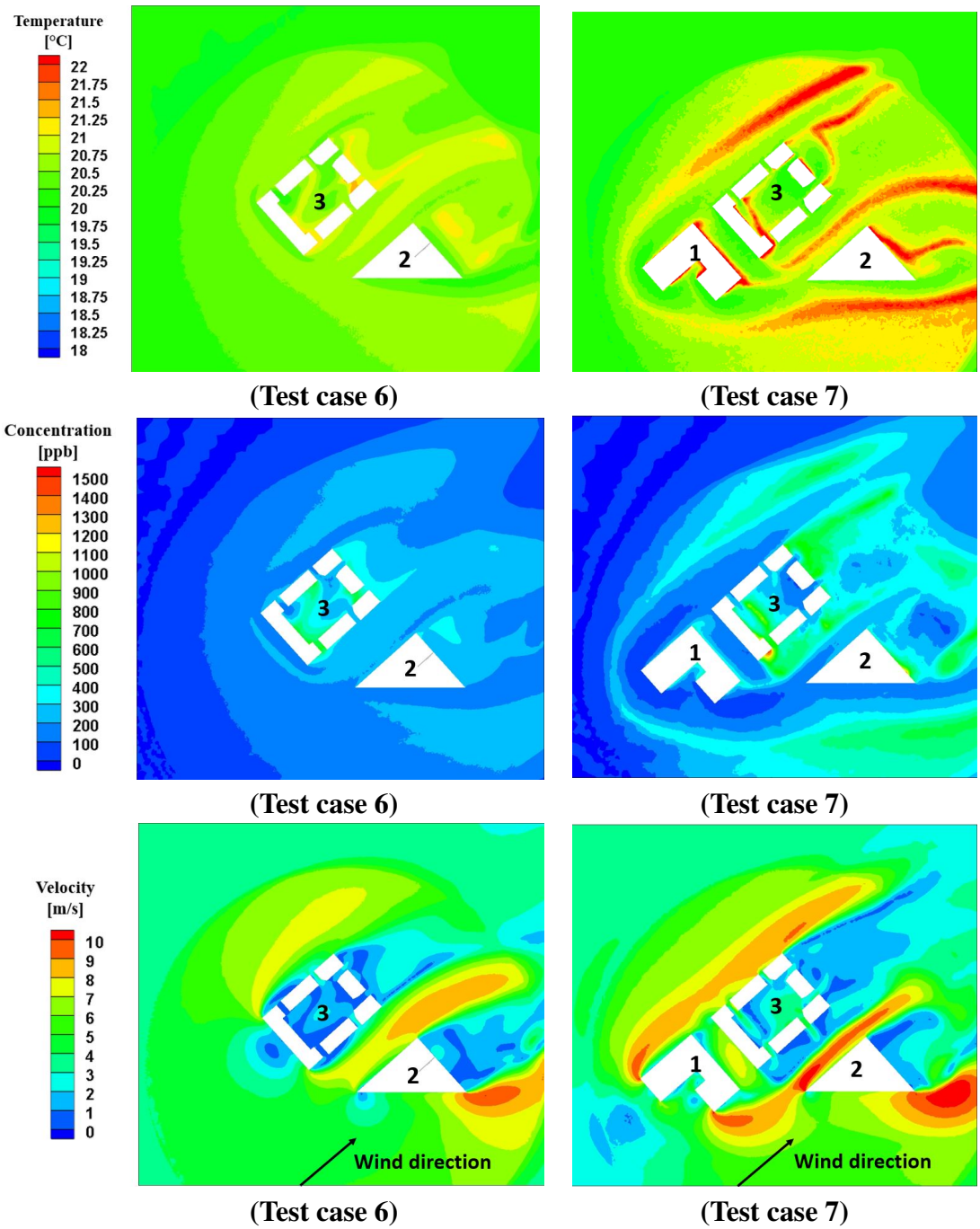

Figure 6.10: Comparison of temperature, velocity, and pollution contours for Test cases 6 and 7 at the pedestrian level (2 m), bottom heating: 10 °C, cooling intensity: 250 W m^{-3}, wind speed at the inlet: 8 m/s.

6.5.4 Test case 7 with mitigation strategies

This section explores how different vegetation layouts such as green roofs, green walls, and trees affect microclimate air temperature, pollution dispersion, and velocity at the pedestrian level. In order to do so, five scenarios are examined, as discussed in section 6.4.2.

First, in scenario 1, the mean flow, temperature, and pollutant characteristics are provided in the absence of ground heating. The results of the cases with street bottom heating, referred to as scenarios 2 and 3, are then presented. The difference between scenarios 3 and 4 is that the cooling intensity in the latter is doubled. The difference between the third and fifth cases is that the velocity in the latter is half.

In all of the circumstances investigated, the average of temperature, pollution, and velocity magnitudes in the region of S1 are decreased by all vegetations. However, the extent of this reduction depends on street bottom heating, vegetation cooling intensity and wind speed. In chapter 5, the influence of vegetation on velocity reduction was discussed. The cooling mechanisms involved in vegetations (e.g. shade and evapotranspiration) are discussed here [180, 206, 216]. Several authors explained the reduction of pollution by trees, with wind tunnel experiments or CFD models (RANS or LES) validating their findings [103, 105]. The presence of trees in street canyons is understood to alter airflow and, as a result, pollutant dispersion. Trees act as impediments to flow due to the reduction in air ventilation imposed by them, and hence larger concentrations are produced in places where trees are present. Furthermore, below the tree crown, the wind direction changes which acts as a source of turbulence and increases turbulent diffusion, which aids in the dilution of contaminants [217]. Despite the fact that all simulations in this paper were performed with RANS, Salim et al. [217] discovered that LES simulations are better than RANS simulations in the presence of pollution because LES predicts horizontal diffusion of concentration better.

It must be noted that although the presence of vegetation reduces the average amount of pollution surrounding all buildings (region S1), it might change the pattern of pollution dispersion in different areas, which will be explored in this section. Despite the fact that walls and green roofs are on all buildings façades, and trees are only located in high velocity areas, the greatest

average temperature reduction is achieved by trees in all tested scenarios, as quantified in Tables 6.9, 6.10 and 6.11. It was also shown that green walls and green roofs are more effective at reducing pollution than trees.

When the ground temperature rises, the average velocity magnitude at the pedestrian level goes up, especially in the S1 zone, but a comparison of Scenario 1 to 3 for the case with no vegetation in Figure 6.13 shows no significant variation in the mean flow pattern between cases with different bottom heating situations. The results of earlier studies [218, 219] show that increasing ground heating improves mean flow inside street canyons. According to these findings, the mean wind speed increased under unstable conditions while decreasing in calm conditions. The Richardson number (see equation 6.1) is used to classify stable and unstable conditions [220]. This indicates that -0.03< R_b <0 is in an unstable region, which corresponds to bottom heating cases in this study. An unstable zone is a time of day when the earth's surface is heated and is normally throughout the day, and a neutral situation is when there is no heating on the ground. Mechanical turbulence and convection are prominent in unstable environments. As the temperature of the ground increases further, the region becomes more unstable. This demonstrates that the air above the surface heats up and expands. As a result of its lighter weight, it begins to rise, causing vertical movement in the atmosphere.

As expected, the average air temperature drops as the cooling intensity increases, and cooler air flows into the street canyon as the cooling effect becomes stronger. This can be seen by comparing scenario 3 and 4 in Figure 6.11, where the only variation is the cooling intensity. Green walls and trees are the most effective solutions for lowering air temperature in the S1 zone, with a drop of 0.5 °C to 0.7 °C when cooling intensity is doubled. Because no trees are planted at the back of building 2, the comparison for region S3 is unnecessary. In scenario 3, trees reduce the temperature in region S2 by 0.95 °C, while green walls reduce temperature by 1.43 °C in scenario 4. It's worth noting that green walls are on the façades of buildings, and trees are only found in specific regions of high velocities. In comparison to trees, increasing the cooling effects of green walls results in a greater temperature drop.

In scenario 5, lowering the wind speed increases the temperature gradient on vegetations, as

shown in Figure 6.14. This observation was confirmed by the results of Fu et al. [221], who found that the temperature gradient on porous material is lower at higher Reynolds. In this simulation, the vegetation acts as a porous medium. As velocity increases, the fluid's inertial forces become more important. The disturbance of the flow flowing process grows along with the increase in heat exchange. Thus, the temperature gradient of the vegetation and, as a result, the entire domain diminishes.

Increasing the cooling intensity of the vegetation and decreasing the wind speed in scenarios 4 and 5 reduces the temperature the most in all test case circumstances. When comparing doubling the cooling intensity with halving the wind speed, halving the wind speed is more effective in lowering the average air temperature, as shown in scenario 5 in Figure 6.11. Where the temperature reduction by green walls and trees in S1 region is 0.9 and 0.8 °C, respectively. Because the trees are not planted at the back of buildings 2 and 3, the best comparison may be made in region S2. In scenario 4, temperature reductions by green walls and trees are 2.15 °C and 2.20 °C, respectively. In all test case scenarios and in all regions, green roofs reduce temperature by 0.1-0.4 °C .

Under neutral conditions, trees reduce temperature by 0.16 °C. In unstable situations, this is 0.25 °C and 0.51 °C. Meaning that as the bottom heating rises, vegetations become more effective at reducing temperature. Green roofs and green walls are following the same trend.

A slight drop in the average of pollutant concentration at the pedestrian level can be detected as the ground temperature rises. One cause could be that earth heating encourages the top layer to move downhill. The study of Jiang et al. [189] for a basic case has proved this. According to Kim and Baik [88, 214, 222] it was found out that the buoyancy force due to the street bottom heating strengthens vortices by reinforcing mechanically induced upward motion. Furthermore, in all circumstances, lowering the wind speed at the inlet resulted in higher pollution concentrations. As a result, more windy weather leads to improved air quality. Cichowicz et al. [223] has also confirmed this. Maerschalck et al. [106] also believes that porous nature of the vegetation can produce more mechanical turbulence and absorb more turbulent kinetic energy. Reduced wind speed and recirculation flow (wake region) result in increased shear

stress and turbulence which subsequently increased dispersion of pollutants. As a result, in the test cases studied in this section, the largest concentrations are found in the recirculation zones inside buildings 3 and in the rear of building 2.

As shown in Figure 6.12, pollution reduction by all vegetations in neutral and unstable situations is nearly identical. The highest levels of pollution are found in the back of buildings 2 with a height of 80 m, where the lowest velocity recirculation zones are located. For scenarios 1 to 3, green roofs and green walls reduce pollution by about 41%, while trees reduce pollution by 26%. While the velocity reduction has slowed the greatest with the use of trees, pollution dispersed the most in those areas with the lowest velocity. When comparing the case without vegetation in scenario 3 and 5 in Figure 6.12, it can be shown that halving the wind speed can result in a 67 % increase in pollution in urban areas. Green roofs reduce pollution by 52 % in scenario 5, while green walls and trees reduce pollution by 44 %. This indicates that when the velocity at the inlet is lower, or when the weather is calmer, the efficiency of all forms of vegetation in reducing pollution is better. Green roofs are more effective in reducing pollution than green walls at lower speeds. Although the average pollution reduction from green walls and green roofs is similar, a comparison between scenario 3 and 5 in Figure 6.12, where the only difference is velocity, reveals that green roofs are more effective than green walls. In general, green roofs appear to be more effective at reducing pollution than other alternatives.

Despite the fact that the contours are given at the pedestrian level, the temperature difference is shown in two separate planes (Figures 6.15 and 6.16). These diagrams depict how convection in the atmosphere distributes heat energy from warmer places near the Earth's surface to higher altitudes in the atmosphere. This graph indicates that the comparison should not be limited at the pedestrian level. When comparing case 'a' with case 'c', as well as case 'd' with case 'b' in this figure, it can be seen that, while trees are able to reduce temperature in more areas at the pedestrian level, green walls are better in general in reducing air temperature if the vertical comparison is also made.

By looking at the contours and the area weighted average velocity, it is clear that the trees are the best in reducing velocity among all the tested test cases. However, trees are not as effective

as green walls and green roofs in reducing pollution dispersion. In comparison to green walls and trees, the outcomes of this study demonstrate that planting green roofs on tall buildings may not be a cost-effective solution for reducing UHI.

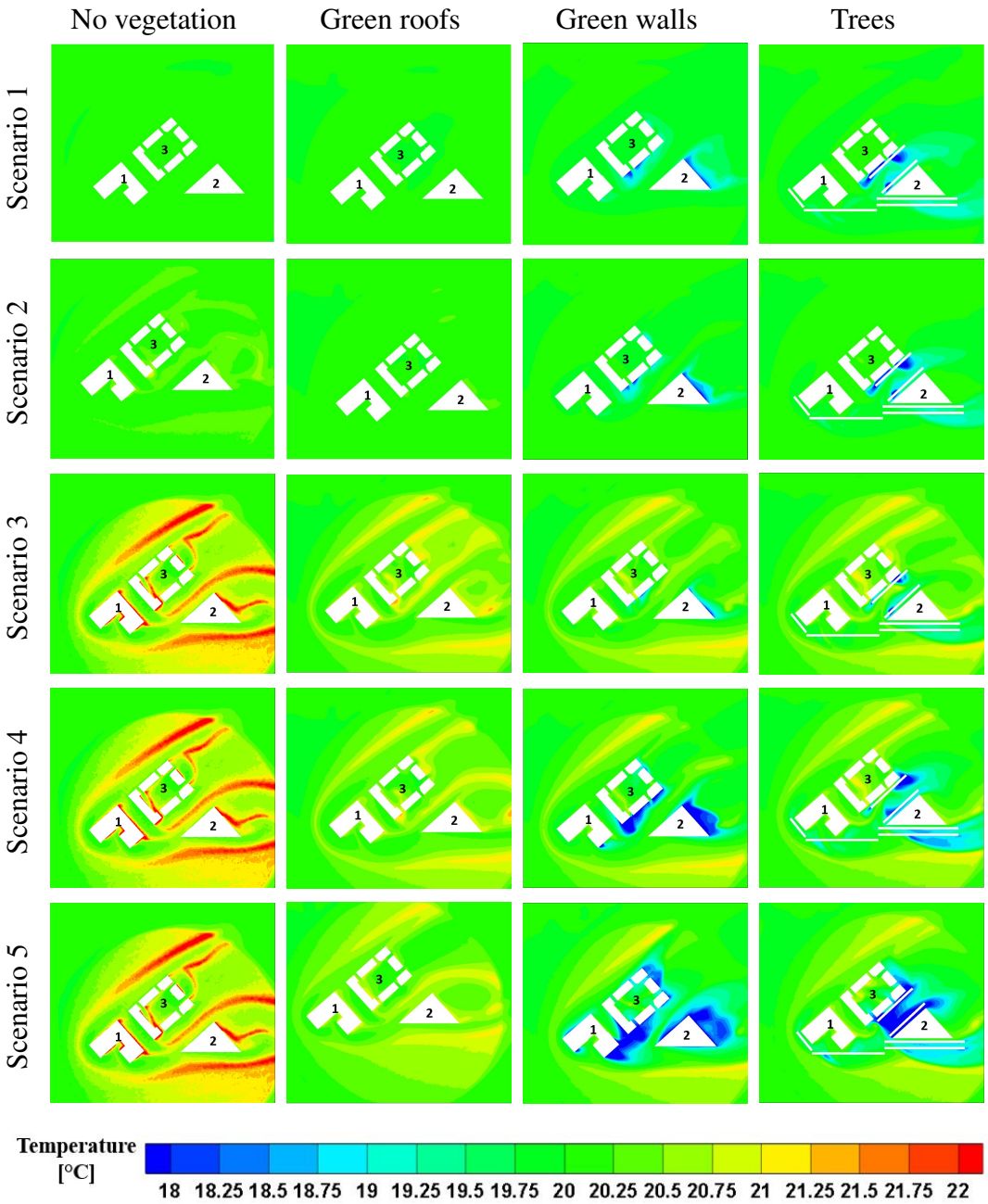

Figure 6.11: Contours of temperature at pedestrian level

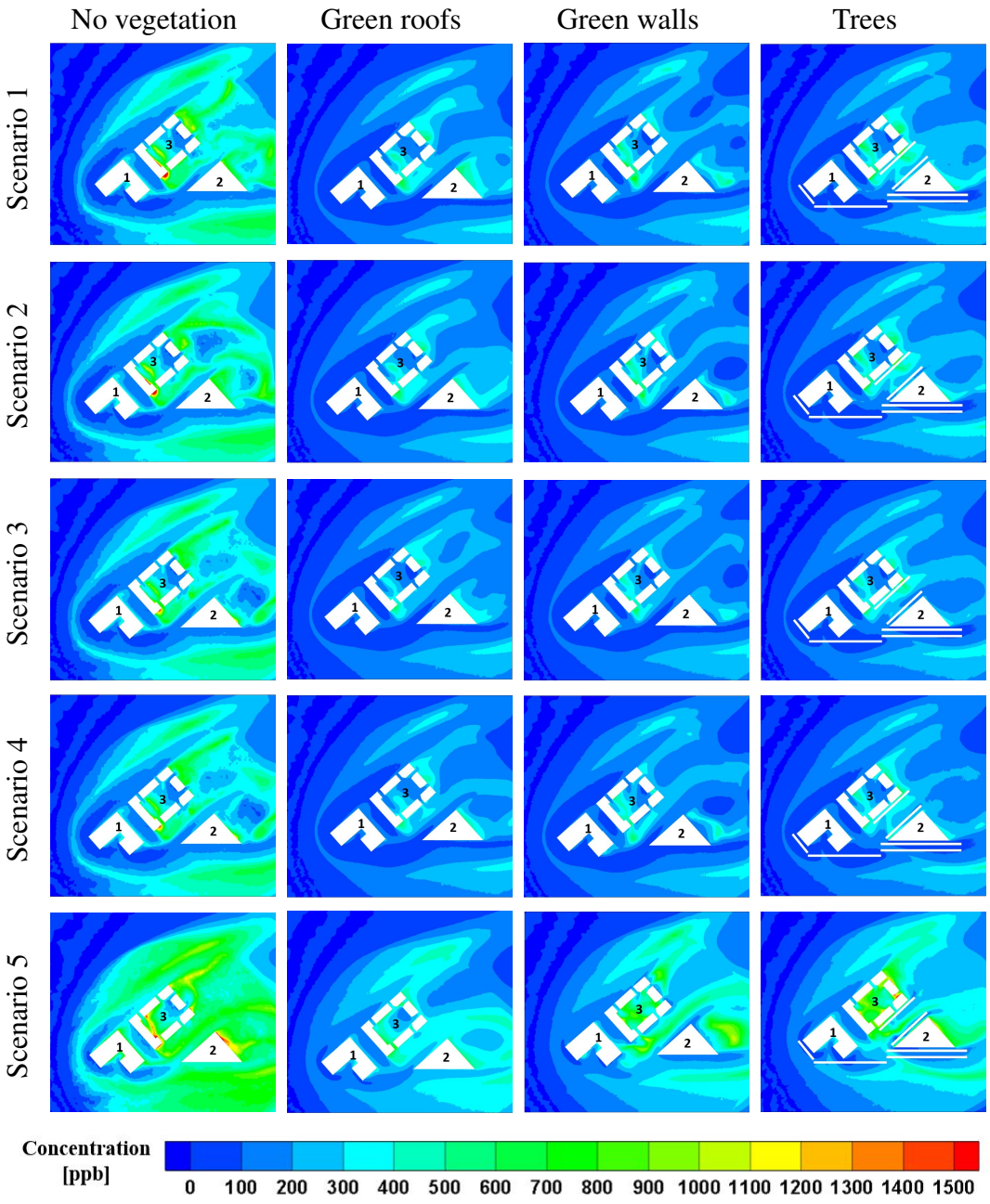

Figure 6.12: Contours of pollutant concentration at pedestrian level

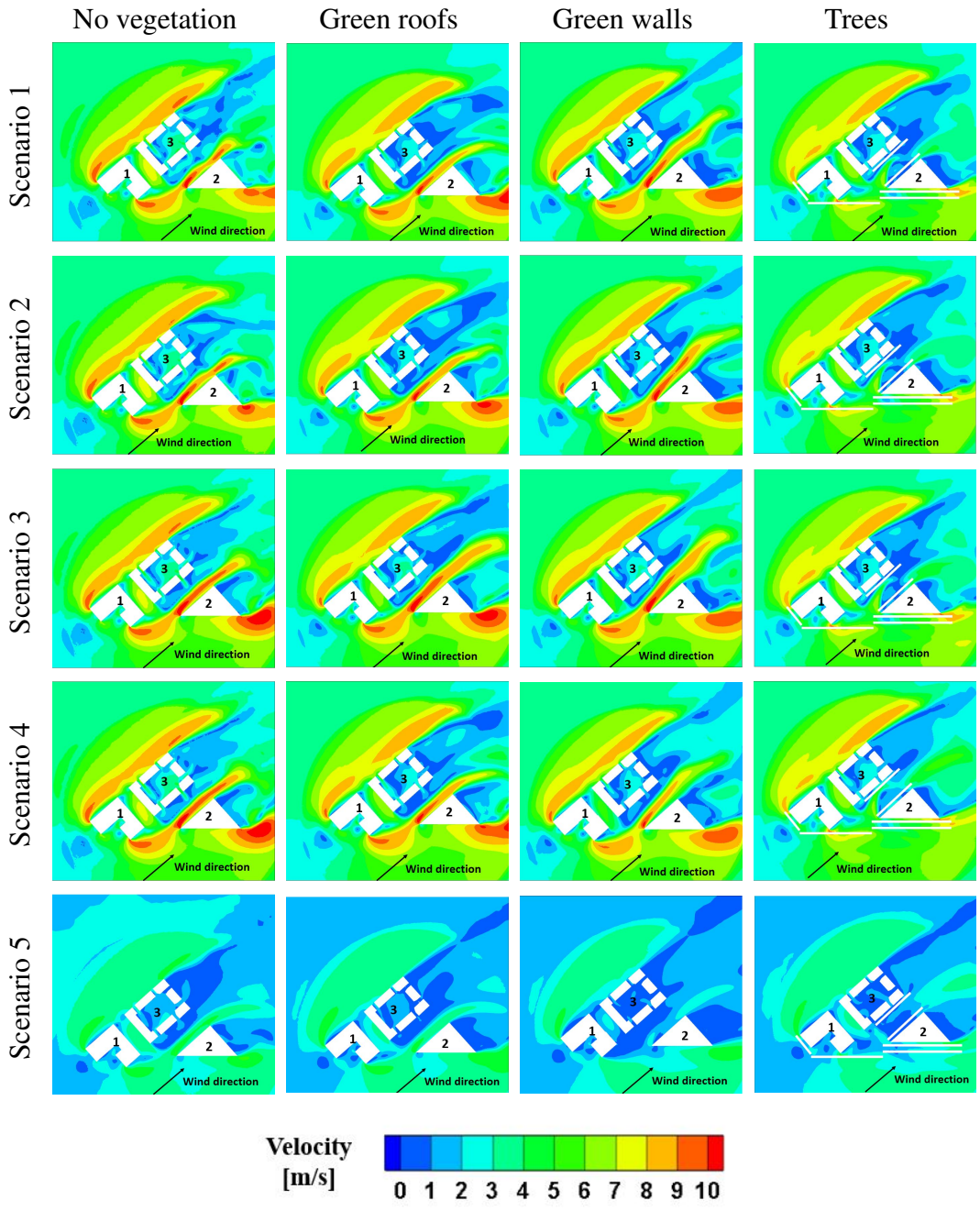

Figure 6.13: Contours of velocity at pedestrian level

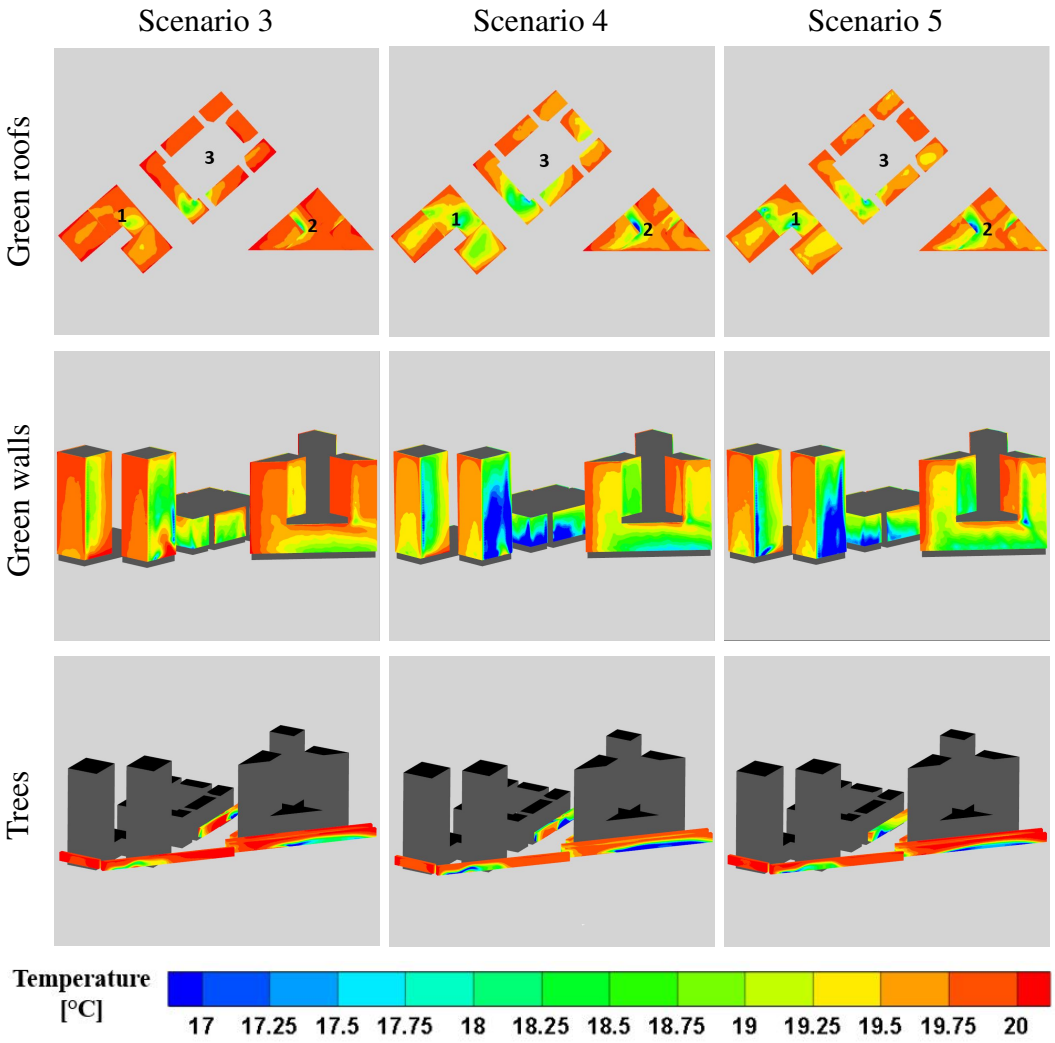

Figure 6.14: Contours of temperature at the surface of green roofs, green walls and trees

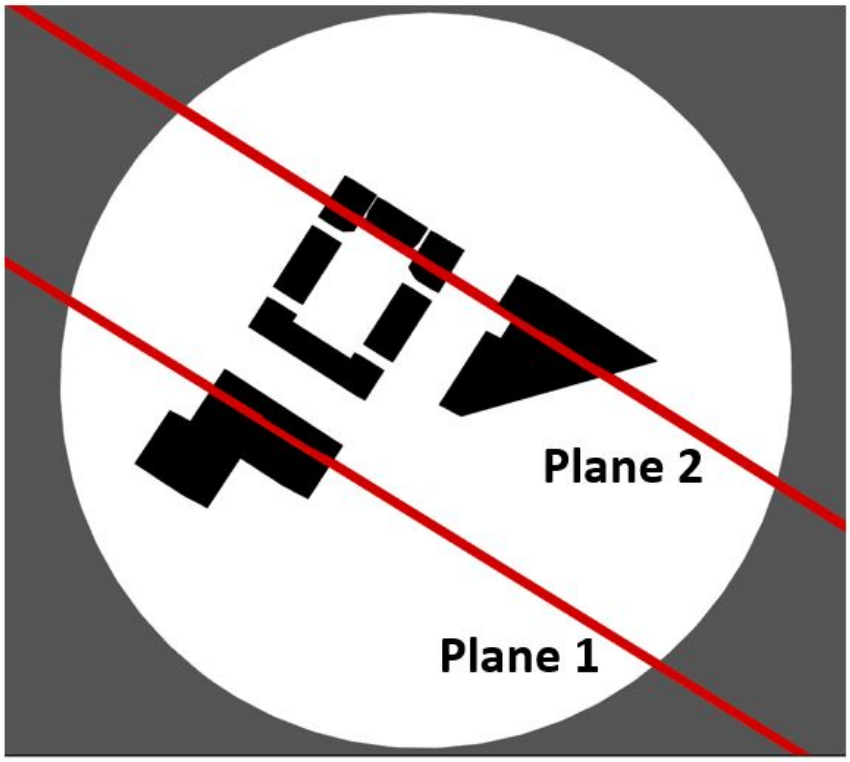

Figure 6.15: plane lines.

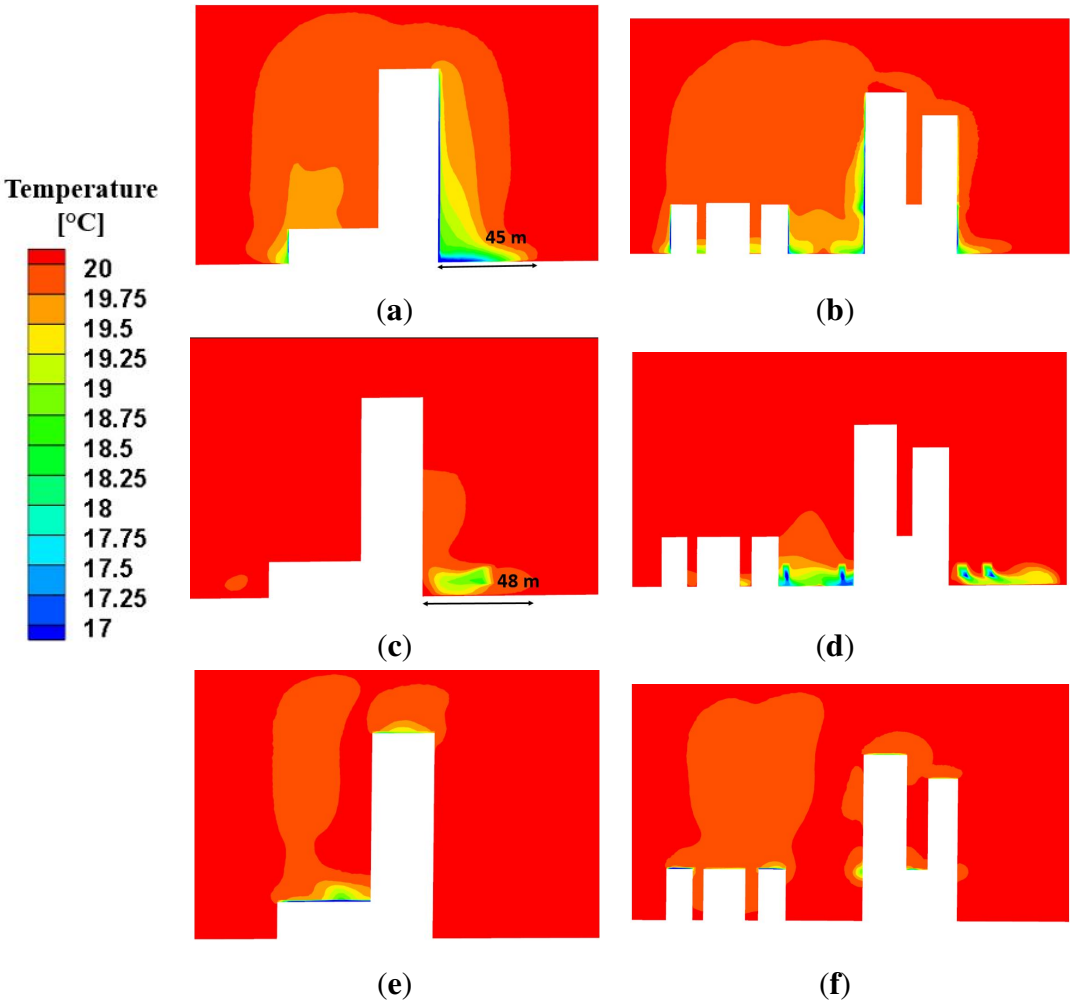

Figure 6.16: Contours of temperature at different planes, bottom heating: 10 °C, cooling intensity: 500 W.m^{-3}, wind speed at the inlet: 8 m/s: (**a**) green walls plane 1; (**b**) green walls plane 2; (**c**) tree plane 1; (**d**) tree plane 2; (**e**) green roofs plane 1; (**f**) green roofs plane 2.

6.5.5 Test case 7 with combination of mitigation strategies

The simulation conditions for the cases in this section are based on scenario 3. where the bottom heating for all cases is 10 °C. The cooling intensity is 250 W m^{-3} and the wind speed at the reference height at the inlet is 8 m/s. In contrast to the previous section, which looked at the effectiveness of green roofs, green walls, and trees individually, this section looks at how

these measures perform when they are combined. The contours of temperature, pollution and velocity are presented in Figure 6.17. Case 'e' is a combination of green roofs and green walls, case 'f' is a combination of green roofs and trees, case 'g' is a combination of green roofs and additional trees (trees all around buildings) and case 'h' is the same as case 'g' but with the tree crowns 2 m closer to the ground. The findings of this section are compared to Test case 7-a in scenario 3, which is a case with no vegetation.

The average temperature drop in cases 'e', 'f', 'g', 'h' for region S1 is 0.5, 0.51, 0.67, and 0.77 °C, according to the findings of this section. While pollution levels decreased by 49%, 47%, 43%, and 42%, respectively. The average quantity of pollutant is reduced in the S1 region, but not in all sections of the domain, as in the other situations reviewed in the previous section. Trees are added around all buildings in cases 'g' and 'h.' The back of buildings have a lower velocity and as a result, a larger level of pollution are observed than in the absence of vegetation. It should be emphasized that, according to the Lawson comfort scale, the backs of buildings are not high-velocity zones (See table 5.2), so planting trees in those areas to lower velocity is unnecessary. The area weighted average of velocity in the region S3 is 1.96 m/s in the absence of vegetation, but this number drops by half when trees are added. This is not only inconvenient for pedestrians, but it also increased pollutants by 2% and 12% in cases 'g' and 'h', respectively. It can be seen that moving the tree crown 2 m closer to the ground reduced the average velocity by 2% more, while by comparing velocity contours of cases g and h in Figure 6.17, it can be seen that both cases were able to reduce the red areas due to the corner and acceleration effect, as discussed in chapter 4. Furthermore, when comparing examples 'f' and 'g,' where the difference is the number of trees, the average velocity reduction for both cases is almost similar, the uncomfortable pedestrian zone (red areas in the velocity contours) is nearly removed. The worst case scenario is combining green walls and green roofs (case e), which failed to reduce high-velocity zones and only reduced velocity by 5% on average for the S1 region.

In comparison to the individual options (Cases a, b, c and d in section 6.5.4), case 'g' and 'h' decrease the temperature more than case 'd' by 0.16°C and 0.26°C, respectively, while the

pollution level increases slightly. Moreover, whether trees are used alone or in conjunction with green roofs and trees, there is no noticeable difference in the reduction of high-velocity zones. Although combining solutions can combat UHI effect better than individual options, the economic evaluation must also take into account the operational costs, maintenance, and other aspects mentioned in Table 2.2.

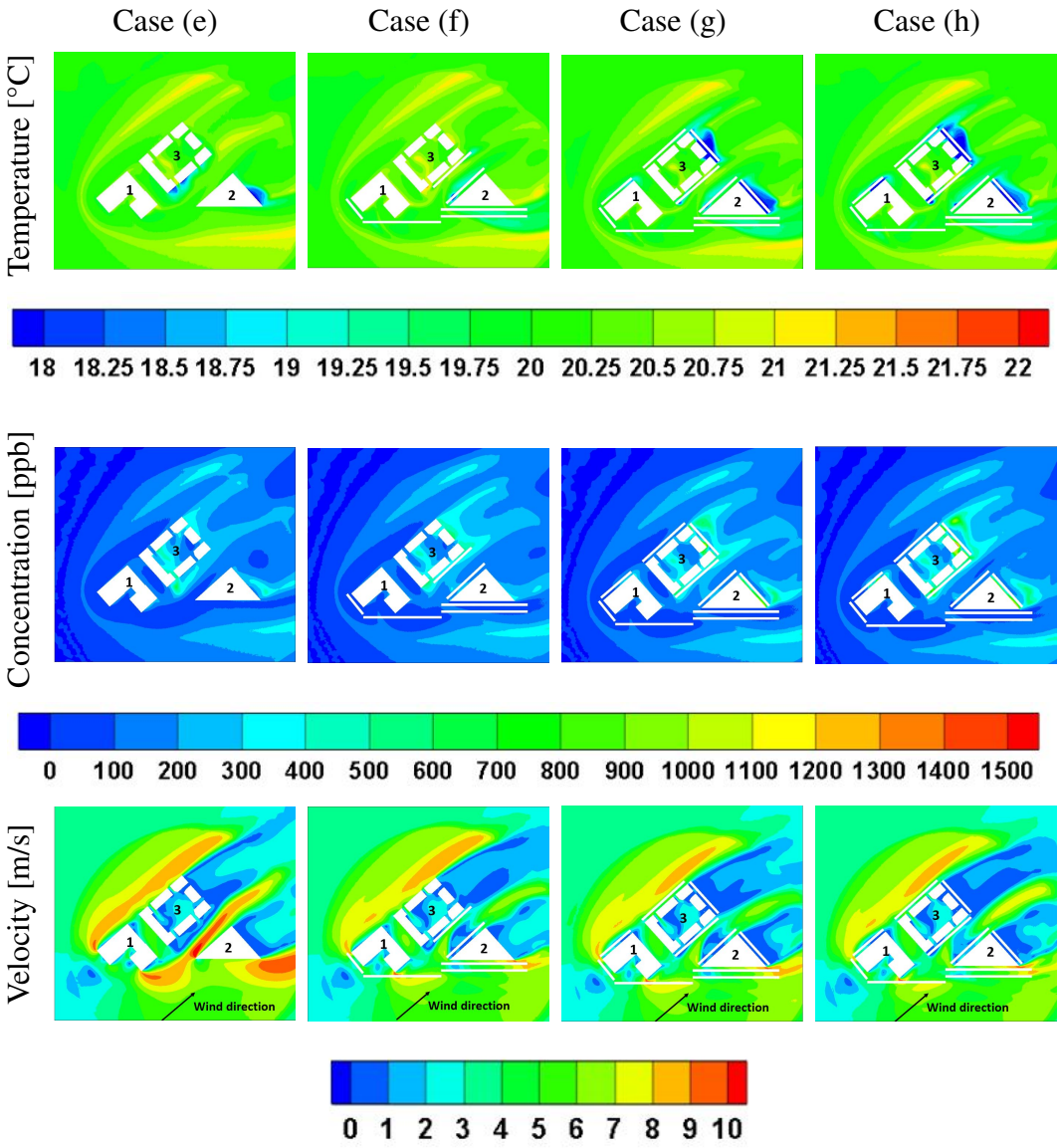

Figure 6.17: Contours of temperature, pollutant concentration and velocity at the pedestrian level for scenario 3 with combination of: (**e**) green roofs and green walls; (**f**) green roofs and trees; (**g**) green roofs and more trees; (**h**) green roofs and trees with trees 2 m closer to the ground.

6.5.6 Test case 7 with targeted mitigation strategy

The simulation conditions for the cases in this section are based on scenario 3. According to the results obtained in the section 6.5.4, green roofs are less effective in temperature reduction, green façades (green roofs and green walls) are better at pollution reduction, and trees are the best in reducing velocity at the pedestrian level. Green walls and trees were discovered to be the most effective ways to reduce urban air temperature. While temperature reduction at pedestrian levels with trees is more observable, based on the temperature gradient at different planes in Figure 6.16, it is observed that with using green walls the intensity of the temperature reduction at higher levels is clearer. It was discovered in section 6.5.5 that a combination of green roofs and green walls is not a viable option for velocity reduction in comparison to the other approaches tested there. As a result of the findings mentioned in the preceding sections, it appears that combining green walls and trees is a viable alternative which is the main focus of this section.

As can be observed in Figure 6.18, the walls facing the wind have a lower temperature gradient than the other walls in these cases. The walls are labelled with numbers ranging from 1 to 5. The temperature gradient on walls 1,2 and 3 is clearly the lowest. As a result, the green walls on this surface have been removed. Although the temperature gradient in wall 5 is greater than on the other labelled surfaces, trees are chosen to be planted in front of this wall because the region in front of it is high-velocity zones (see Figure 6.13). As a result, the green walls on this surface have been removed as well. Face 4 is a smaller wall with a colder surface than Faces 1, 2, and 3. So, in this part, the targeted choices are a case where green walls are removed from all 5 numbered surfaces (case 'i') and a situation where green walls are removed from all numbered faces except face 4 (case 'j'). Since there are no high-velocity areas at the back of the buildings, trees were not planted in these regions. Planting trees close to the edge of buildings reduces velocity and increases pollution, thus it is not required to plant them in regions where pedestrians are not disturbed. The studied cases in this section are presented in Figure 6.6.

The results of this section are compared to the Test case 7 (cases a, b and c) for scenario 3. The reduction of the area weighted average of temperature in region S1, S2, and S3 for case 'i' is

0.54 °C, 0.78 °C, and 0.71 °C, respectively, whereas for case 'j,' it is 0.55 °C, 0.7 °C, and 1.03 °C. These findings reveal that the presence of green walls on wall 4 has an impact on regions S2 and S3 and that they are more effective at temperature reduction in area S3 but less effective in region S2. The total performance of this configuration, however, is not much different from that of case 'i'. When compared to Test case 7-d (with only trees), this combination performs better in terms of temperature reduction in the S1 (largest region) and S3 regions. Trees are better in the S2 (street with buildings around it) area. For region S1, the pollution reduction is very similar to the situations with green walls, green roofs, and trees individually, but it performs better in regions S2 and S3. The average of velocity reduction is also comparable to the trees.

In comparison to the application of vegetation alone or other combination strategies explored, the combination of green walls and trees proved to be a better option. The ideal placement for trees to improve pedestrian comfort, as well as placing green walls on the faces that can produce the highest temperature gradient, are all factors in the optimal combination of green walls and trees. The direction and magnitude of the wind are the most important criteria in determining which walls should be green. Green walls on tall buildings can assist reduce temperature not only at the pedestrian level, but also at higher altitudes by creating cooler air.

6.6 Summary

In this chapter, the impact of various vegetation layouts such as green roofs, green walls and trees on air temperature, pollution dispersion, and velocity has been evaluated. In addition to its impact of individual vegetations, the effectiveness of combination strategies was also investigated. Different scenarios were examined in order to analyse the impact of various types of vegetation under different situations, including wind speed which ranges from 4-8 m/s at a reference height of 10m, and vegetation cooling intensity which varies from 250-500 $W\,m^3$. Three scenarios were also tested in which the streets have no bottom heating, 2 °C bottom heating, and 10 °C bottom heating. Based on the results presented in this chapter, the following

main conclusions can be drawn.

- Adding a building to Test case 6 with a 10 °C bottom heating can raise the average temperature by 0.32 °C and increase pollution concentration and velocity by 71% and 6%, respectively.

- In comparison to green walls and trees, green roofs on tall buildings are less effective at reducing temperature. For all situations studied on Test case 7, the average temperature reduction employing green roofs is between 0.1 and 0.4 °C.

- With increased bottom heating, vegetation is more effective at lowering temperature. The average temperature reduction by trees on Test case 7 is 0.16 °C in neutral conditions (no ground heating), and 0.25 °C and 0.51 °C in unstable situations (cases with bottom heating).

- Pollution concentration rises as wind speed decreases. In Test case 7, halving the wind speed results in a 67% increase in pollution. The places with the highest levels of pollution are those areas with recirculation flow.

- In Test case 7, walls facing the wind have a lower temperature gradient, hence removing green walls from those surfaces has no substantial impact on UHI, pollution, or velocity reduction.

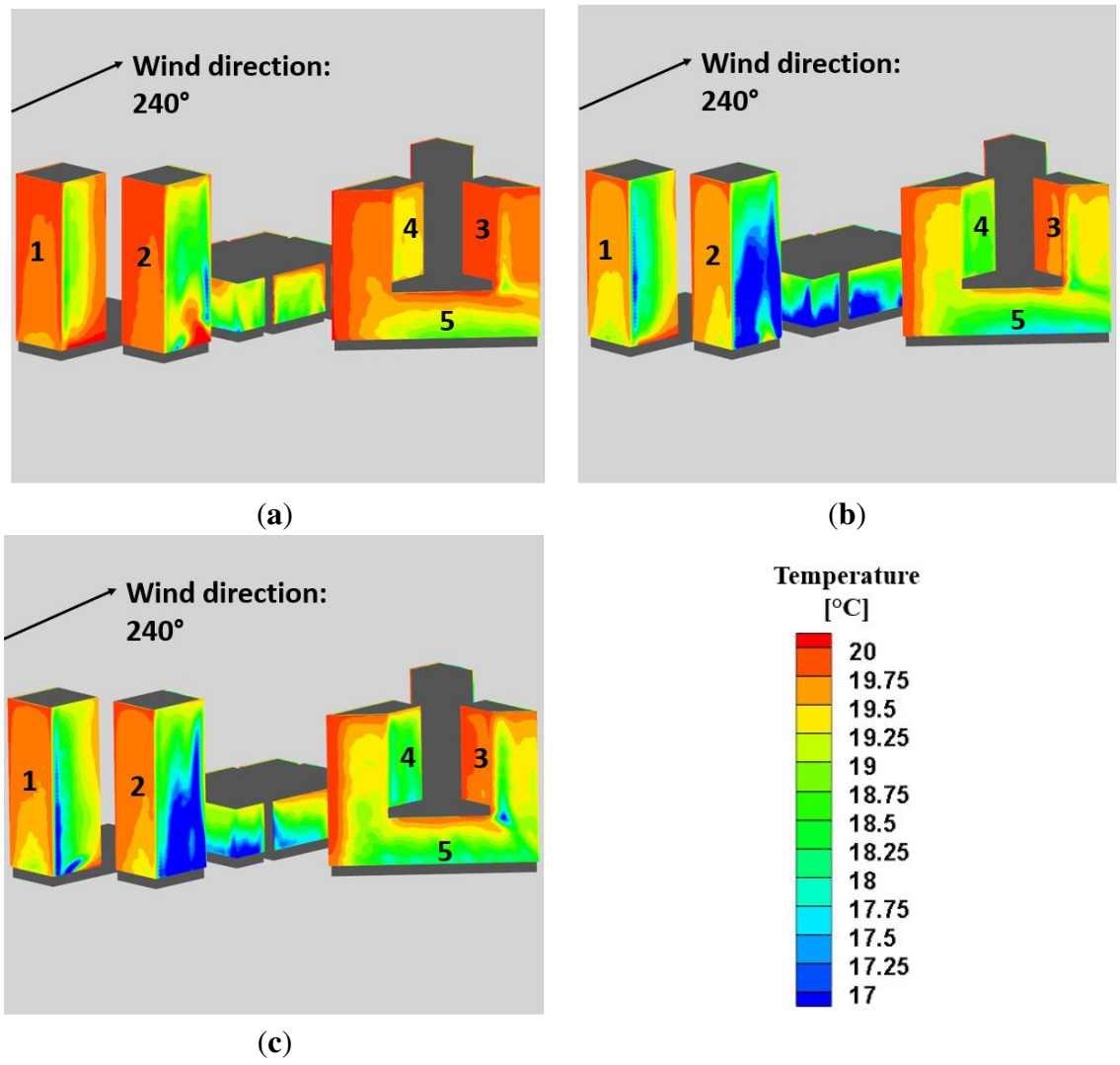

Figure 6.18: Temperature gradient on walls using green walls as a mitigation strategies with bottom heating: 10 °C (**a**) wind speed at the inlet: 8m/s, cooling intensity: 250 W m^{-3}; (**b**) wind speed at the inlet: 8 m/s, cooling intensity: 500 W m^{-3}; (**c**) wind speed at the inlet: 4 m/s, cooling intensity: 250 W m^{-3}.

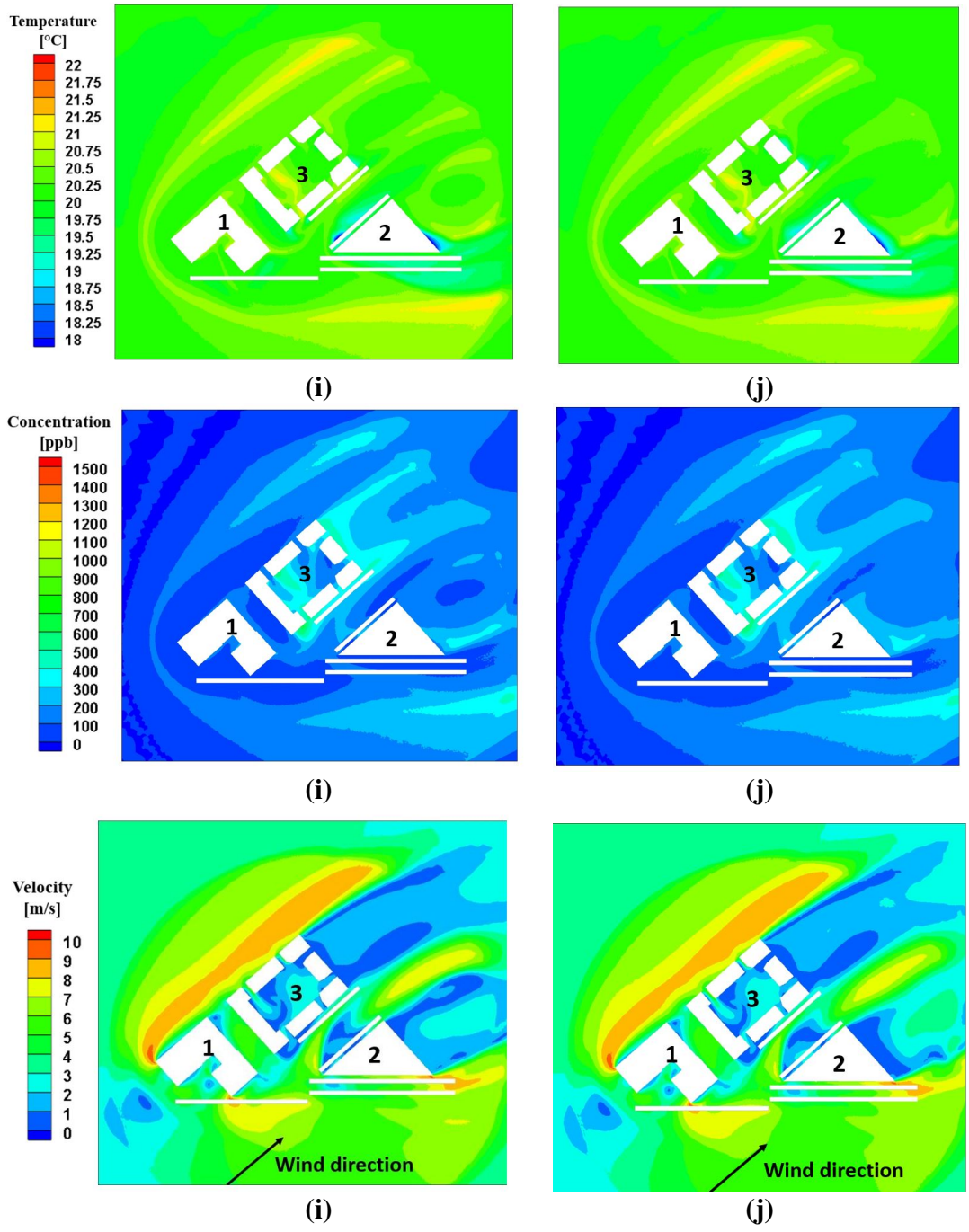

Figure 6.19: Contours of temperature, pollution and velocity at the pedestrian level (2 m), bottom heating: 10 °C, cooling intensity: 250 W m^{-3}, wind speed at the inlet: 8 m/s: (**i**) first targeted combination of green walls and tree; (**j**) second targeted combination of green walls and tree.

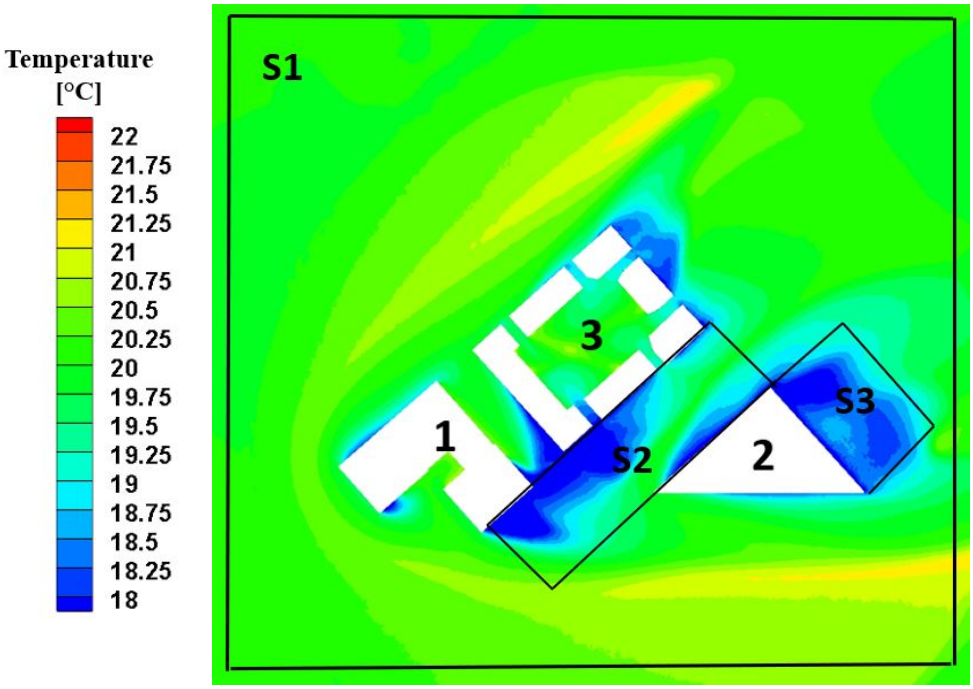

Figure 6.20: Regions S1, S2 and S3: Area weighted average for temperature, concentration and velocity.

Table 6.6: Area weighted average of temperature, concentration and velocity for region S1, all test cases with bottom heating: 10 °C, cooling intensity: 250 W m^{-3}, Wind speed at the inlet: 8m/s.

Test cases	**Temperature [°C]**	**Concentration [ppb]**	**Velocity [m/s]**
Test case 6	20.48	163.50	4.80
Test case 7-a	20.80	280.68	5.13
Test case 7-b	20.47	147.79	5.07
Test case 7-c	20.31	141.41	5.04
Test case 7-d	20.29	152.14	4.61
Test case 7-e	20.30	144.84	4.92
Test case 7-f	20.29	149.26	4.58
Test case 7-g	20.13	159.67	4.50
Test case 7-h	20.027	163.16	4.43
Test case 7-i	20.26	146.62	4.65
Test case 7-j	20.25	146.55	4.69

Table 6.7: Area weighted average of temperature, concentration and velocity for region S2, all test cases with bottom heating: 10 °C, cooling intensity: 250 W m^{-3}, Wind speed at the inlet: 8m/s.

Test cases	**Temperature [°C]**	**Concentration [ppb]**	**Velocity [m/s]**
Test case 6	20.64	207.93	5.67
Test case 7-a	20.77	300.45	5.41
Test case 7-b	20.48	159.92	5.58
Test case 7-c	20.15	166.54	5.31
Test case 7-d	19.82	214.43	3.06
Test case 7-e	20.00	170.93	5.13
Test case 7-f	20.06	178.05	3.49
Test case 7-g	19.94	177.74	3.59
Test case 7-h	19.81	196.22	3.49
Test case 7-i	19.99	167.25	3.64
Test case 7-j	20.06	170.98	3.65

Table 6.8: Area weighted average of temperature, concentration and velocity for region S3, all test cases with bottom heating: 10 °C, cooling intensity: 250 W m^{-3}, Wind speed at the inlet: 8m/s.

Test cases	**Temperature [°C]**	**Concentration [ppb]**	**Velocity [m/s]**
Test case 6	20.70	249.88	1.40
Test case 7-a	20.92	381.85	1.96
Test case 7-b	20.73	312.40	1.46
Test case 7-c	19.47	219.09	1.48
Test case 7-d	20.45	205.60	1.67
Test case 7-e	19.47	191.32	1.23
Test case 7-f	20.46	196.36	1.61
Test case 7-g	18.57	392.29	0.88
Test case 7-h	18.57	425.11	0.81
Test case 7-i	20.03	164.89	1.45
Test case 7-j	19.70	215.85	1.33

Table 6.9: Area weighted average of temperature, concentration and velocity for region S1

Scenarios	Test cases	Temperature [°C]	Concentration [ppb]	Velocity [m/s]
Scenario 1	Test case 7-a	20.02	301.40	4.97
	Test case 7-b	20.01	157.33	4.92
	Test case 7-c	19.89	150.38	4.91
	Test case 7-d	19.86	162.03	4.55
Scenario 2	Test case 7-a	20.19	300.55	4.99
	Test case 7-b	20.10	154.90	4.89
	Test case 7-c	19.97	148.88	4.89
	Test case 7-d	19.94	158.68	4.55
Scenario 3	Test case 7-a	20.80	280.68	5.13
	Test case 7-b	20.47	147.79	5.07
	Test case 7-c	20.31	141.41	5.04
	Test case 7-d	20.29	152.14	4.61
Scenario 4	Test case 7-a	20.80	280.68	5.13
	Test case 7-b	20.44	147.00	4.93
	Test case 7-c	20.11	146.97	4.80
	Test case 7-d	20.13	152.10	4.63
Scenario 5	Test case 7-a	20.79	474.26	2.61
	Test case 7-b	20.43	229.96	2.51
	Test case 7-c	19.91	269.59	2.24
	Test case 7-d	20.00	264.71	2.42

Table 6.10: Area weighted average of temperature, concentration and velocity for region S2

Scenarios	**Test cases**	**Temperature [°C]**	**Concentration [ppb]**	**Velocity [m/s]**
Scenario 1	Test case 7-a	20.04	324.51	5.01
	Test case 7-b	20.01	187.29	4.90
	Test case 7-c	19.62	188.77	4.88
	Test case 7-d	19.26	239.12	2.97
Scenario 2	Test case 7-a	20.21	321.53	5.19
	Test case 7-b	20.11	183.54	4.92
	Test case 7-c	19.73	181.02	4.95
	Test case 7-d	19.35	231.80	2.99
Scenario 3	Test case 7-a	20.77	300.45	5.41
	Test case 7-b	20.48	159.92	5.58
	Test case 7-c	20.15	166.54	5.31
	Test case 7-d	19.82	214.43	3.06
Scenario 4	Test case 7-a	20.77	170.93	5.13
	Test case 7-b	20.44	173.59	5.00
	Test case 7-c	19.34	191.04	4.47
	Test case 7-d	19.52	221.21	3.22
Scenario 5	Test case 7-a	20.78	518.32	2.51
	Test case 7-b	20.46	283.72	2.23
	Test case 7-c	18.63	389.60	1.15
	Test case 7-d	18.58	335.32	1.36

Table 6.11: Area weighted average of temperature, concentration and velocity for region S3

Scenarios	**Test cases**	**Temperature [C]**	**Concentration [ppb]**	**Velocity [m/s]**
Scenario 1	Test case 7-a	20.06	490.42	2.61
	Test case 7-b	20.03	371.66	1.77
	Test case 7-c	18.97	243.54	1.07
	Test case 7-d	19.92	300.53	1.16
Scenario 2	Test case 7-a	20.36	507.13	2.63
	Test case 7-b	20.22	332.85	1.77
	Test case 7-c	19.05	206.19	1.26
	Test case 7-d	20.09	262.89	1.12
Scenario 3	Test case 7-a	20.92	381.85	1.96
	Test case 7-b	20.73	312.40	1.46
	Test case 7-c	19.47	219.09	1.48
	Test case 7-d	20.45	205.60	1.67
Scenario 4	Test case 7-a	20.92	191.32	1.23
	Test case 7-b	20.66	311.45	1.45
	Test case 7-c	18.17	199.91	1.24
	Test case 7-d	20.29	254.02	1.44
Scenario 5	Test case 7-a	20.34	937.76	1.15
	Test case 7-b	20.54	393.68	0.73
	Test case 7-c	18.06	471.53	0.83
	Test case 7-d	19.76	646.50	0.82

Chapter 7

Conclusion and Future Work

7.1 Discussion and conclusion

In the present study, CFD simulations were conducted for seven different test cases. The first case was a simple model to conduct sensitivity analysis and validate the CFD methodology. The second case involved a large and detailed 3D model representing the East Village in the London Olympic Park. Finally, the third case focused on assessing the effects of mitigating wind by planting trees. Many factors can affect wind mitigation including direction, tree type (e.g., deciduous, evergreen), tree age, stem height, tree height, crown height, crown width, diameter at breast height, distance between trees and distance of buildings to the trees [141, 180]. Considering all these parameters simultaneously to find the optimised type of tree and arrangement formed the scope of a parametric study. Thus, this section of this study dealt with optimising the arrangement of trees after the tree selection (e.g., based on price, weather condition, etc). The simulations were performed using four turbulence models including standard k-ε, realizable k-ε, standard k-ω and SST k-ω, building on the previous track-record of the authors in the field [224–226]. By making a comparison between simulation results and experimental data in Test case 1 and other references, including the work of Tominaga et al. [203], it is believed that the k-ε model is appropriate for the simulation of wind in urban areas. However, other renormalized groups of k-ε might show more accurate results, but in this work, only the

available turbulence models in STARCCM+ were tested, which can be used with wall function methods. Test case 4 is the 2D model in an idealised street canyon for prediction of the air temperature with bottom heating. The same model and solution approach were used to model energy in urban areas with bottom heating as in Test case 4. Test case 5 is a basic model for predicting air temperature and pollution dispersion in street canyon with two buildings. The simulation work of Baik et al. [101] was used to validate this case. Based on the findings of this validation research, the same technique for modelling the pollution in urban areas was employed for Test cases 6 and 7. Two additional case studies were considered: Test Case 6, representing a selected area of the East Village in London with seven buildings; and Test Case 7, representing the same area as Test case 6 but with one more building. CFD simulations of flow, energy, and pollution were performed, and the comparison between Test Cases 6 and 7 demonstrated how including a building into an urban design can aggravate the urban heat island effect (UHI), degrade air quality, and cause pedestrian discomfort. As a result, as new buildings are constructed, mitigation strategies to minimise these effects must be offered. The impact of vegetation (such as green roofs, green walls, and trees) on pedestrian comfort, air quality, and UHI was studied for Test Case 7. In order to measure the impact of various types of vegetation under different situations, five scenarios were examined. These scenarios differ in terms of bottom heating, vegetation cooling intensity and the magnitude of the wind speed at the inlet. The results for Test Case 7 showed that all vegetations reduced the average temperature, pollution dispersion, and velocity magnitude at the pedestrian level. In addition to evaluating vegetations individually, the effects of combining these measures were studied.
Overall, based on the results presented thus far, the following main conclusions can be drawn:

- An unstructured polyhedral mesh gives more accurate results compared to a tetrahedral mesh for the same base size and increasing the number of prism layers from 2 to 5 does not change the results significantly. By using a wall function to predict the velocity around buildings, there should be a reasonable growth rate between the outer prism layer and the first core cell. The results of the simulation of Test case 1 show that more accurate results are obtained if the prism layer total thickness is 20% of the core cell

size.

- The validation study in Test case 1 revealed that the standard and realizable k-ε turbulence models produce more accurate results, while the results of the standard k-ε were slightly closer to the measurement data. The commonly used SST k-ω model underestimates the turbulent kinetic energy around buildings and as a result, flow separation is expected around the building and therefore it was found to be less accurate compared to standard and realizable k-ε models for this application.

- The results of Test case 3 show that when employing birch trees, denser trees are needed to overcome high-velocity zones caused by the corner effect. If the tree crown is closer to the ground, fewer trees can be planted there. The effect of tree age can be seen in this conclusion. Wind is better mitigated by younger trees with crowns closer to the ground. Older trees with larger crowns, on the other hand, are better at reducing wind speed. More investigation is required to assess the impact of tree age. In certain regions with high-velocity wind, using trees with a wider crown, or locating trees closer to the edge of buildings are likely to mitigate the corner and downwash effects more efficiently. Further work is required to assess the impact of evergreen trees with wider crown.

- In comparison to green façades, trees are the most effective type of vegetation for lowering velocity due to the corner and downwash effects. Because it has a broader crown and can be planted anywhere on the street, it is the ideal option for pedestrian comfort. Green walls and roofs, on the other hand, are solely on the exteriors of buildings.

- Decreasing wind speed increases the temperature gradient on vegetation, resulting in a greater drop in air temperature at the pedestrian level. However, pollution concentration rises as wind speed decreases. The places with the highest levels of pollution are those areas with recirculation flow.

- Increasing the vegetation's cooling intensity and leaf area density reduces the UHI effect, but has little effect on changing the pattern of pollutant dispersion at the pedestrian level.

- In comparison to green walls and trees, green roofs on tall buildings are less effective at reducing temperature. Green walls reduce temperature more at higher heights, in contrast to trees, which are generally at the pedestrian level.
- As the ground temperature rises, a slight decrease in the average pollutant concentration at the pedestrian level can be detected. In both neutral and unstable conditions, pollution reduction by all means of vegetation is relatively similar. In addition, with increased bottom heating, vegetation is more effective at lowering temperature.
- Overall, when considering the effects of velocity, temperature, and pollution, a combination of green walls and trees on high-speed wind and tall buildings is the best.

7.2 Recommendation for future work

The results of this study can be improved in a number of ways, some of which are given below:

- Accurate modelling of radiation provides more realistic results. In order to provide a more reliable predictions of air temperature, radiation parameters such as radiation flux, emission angle, wavelength of radiation, surface absorptivity, reflectivity, and transmissivity, must be taken into account. However, bottom heating is used in this study to represent how the sun warms the earth. In addition, the strength of bottom heating varies depending on the time of day.whereas in this study, it was fixed, and the simulations were run in steady-state mode.
- Taking into account other heat sources, such as anthropogenic heat (traffic, industry, and people), yields more accurate results.
- The pollutant emission rate is determined using traffic data, however pollution can also be caused by industry. Furthermore, unlike the non-reactive pollutant suggested in this study, the pollutant in a real case study would be reactive.
- It is necessary to assess the impact of vegetation on air temperature, pollution dispersion, and velocity at various times of the day. The pollution source term, which represents the

average number of cars per hour as well as temperature variations during the day, is not constant. As a result, using unsteady state simulation to assess the impact of these time-varying variables can yield more precise results.

- This research looks at the constant drag coefficient for deciduous trees. Porosity, on the other hand, changes with high wind speeds, reducing the drag effects on trees [105, 186].

- It is also recommended that the impact of pollution deposition on vegetation be considered. Only dispersion was examined in this study. The pattern of pollution created by green roofs, green walls, and trees will be more accurate if deposition is taken into account.

- When the various layers of green roofs or a green wall are modelled, more realistic simulation can be accomplished. Green façades were modelled as a green cube derived from the roof and walls in this research. Planting vegetation on building surfaces, on the other hand, requires numerous layers.

- This study only considered a fixed thickness for green walls and green roofs, but different thicknesses can be modelled. Modifying the thickness of green walls and roofs, on the other hand, can alter their efficiency in terms of changing pollutant dispersion, wind speed, and air temperature.

- To choose optimal measures for improving thermal environment, an economic study must be undertaken, which includes a comparison of the costs of trees, green roofs, and green walls. Greenery's environmental effectiveness can be improved if different types of vegetation are combined, but the viability of these combinations, as well as their maintenance time and cost, must be assessed.

Bibliography

[1] B. Hong, B. Lin, Numerical studies of the outdoor wind environment and thermal comfort at pedestrian level in housing blocks with different building layout patterns and trees arrangement, Renewable Energy 73 (2015) 18–27.

[2] L. Pierangioli, G. Cellai, R. Ferrise, G. Trombi, M. Bindi, Effectiveness of passive measures against climate change: Case studies in central italy, in: Building Simulation, Vol. 10, Springer, 2017, pp. 459–479.

[3] M. S. Fadl, J. Karadelis, Cfd simulation for wind comfort and safety in urban area: A case study of coventry university central campus, International journal of architecture, engineering and construction 2 (2) (2013) 131–143.

[4] S. Cammelli, R. Stanfield, Meeting the challenges of planning policy for wind microclimate of high-rise developments in london, Procedia engineering 198 (2017) 43–51.

[5] J. Yang, Z.-H. Wang, K. E. Kaloush, Environmental impacts of reflective materials: Is high albedo a 'silver bullet'for mitigating urban heat island?, Renewable and Sustainable Energy Reviews 47 (2015) 830–843.

[6] H. Frumkin, Urban sprawl and public health, Public health reports (2016).

[7] T. R. Oke, The energetic basis of the urban heat island, Quarterly Journal of the Royal Meteorological Society 108 (455) (1982) 1–24.

[8] A. Mohajerani, J. Bakaric, T. Jeffrey-Bailey, The urban heat island effect, its causes, and mitigation, with reference to the thermal properties of asphalt concrete, Journal of environmental management 197 (2017) 522–538.

[9] S. U. Grimmond, Urbanization and global environmental change: local effects of urban warming, Geographical Journal 173 (1) (2007) 83–88.

[10] H. Mayer, Air pollution in cities, Atmospheric environment 33 (24-25) (1999) 4029–4037.

[11] J. Fenger, Urban air quality, Atmospheric environment 33 (29) (1999) 4877–4900.

[12] C. A. Pope III, M. Ezzati, D. W. Dockery, Fine-particulate air pollution and life expectancy in the united states, New England Journal of Medicine 360 (4) (2009) 376–386.

[13] D. for Environment Food & Rural Affairs, The air quality strategy for england, scotland, wales and northern ireland, Available online: https://www.gov.uk/government/publications/the-air-quality-strategy-for-england-scotland-wales-and-northern-ireland-volume-1 (accessed on 01/07/2021). (2011).

[14] The beyer building and the glacial boulder, Available online: https://twitter.com/0161manchester_/status/1004662786666979328 (accessed on 01/11/2021).

[15] C. Sarrat, A. Lemonsu, V. Masson, D. Guedalia, Impact of urban heat island on regional atmospheric pollution, Atmospheric environment 40 (10) (2006) 1743–1758.

[16] H. Johnson, S. Kovats, G. McGregor, J. Stedman, M. Gibbs, H. Walton, The impact of the 2003 heat wave on daily mortality in england and wales and the use of rapid weekly mortality estimates, Eurosurveillance 10 (7) (2005) 15–16.

[17] L. Chen, E. Ng, Simulation of the effect of downtown greenery on thermal comfort in subtropical climate using pet index: a case study in hong kong, Architectural Science Review 56 (4) (2013) 297–305.

[18] M. Taleghani, U. Berardi, The effect of pavement characteristics on pedestrians' thermal comfort in toronto, Urban climate 24 (2018) 449–459.

[19] M. Santamouris, On the energy impact of urban heat island and global warming on buildings, Energy and Buildings 82 (2014) 100–113.

[20] M. Santamouris, C. Cartalis, A. Synnefa, D. Kolokotsa, On the impact of urban heat island and global warming on the power demand and electricity consumption of buildings—a review, Energy and Buildings 98 (2015) 119–124.

[21] M. Street, C. Reinhart, L. Norford, J. Ochsendorf, Urban heat island in boston–an evaluation of urban air-temperature models for predicting building energy use, in: Proceedings of the BS2013: 13th Conference of International Building Performance Simulation Association, Chambéry, France, 2013, pp. 26–28.

[22] Y. Toparlar, B. Blocken, P. v. Vos, G. Van Heijst, W. Janssen, T. van Hooff, H. Montazeri, H. Timmermans, Cfd simulation and validation of urban microclimate: A case study for bergpolder zuid, rotterdam, Building and environment 83 (2015) 79–90.

[23] A. Tzavali, J. P. Paravantis, G. Mihalakakou, A. Fotiadi, E. Stigka, Urban heat island intensity: A literature review, Fresenius Environmental Bulletin 24 (12b) (2015) 4537–4554.

[24] P. Ramamurthy, E. Bou-Zeid, Heatwaves and urban heat islands: a comparative analysis of multiple cities, Journal of Geophysical Research: Atmospheres 122 (1) (2017) 168–178.

[25] G. A. Meehl, C. Tebaldi, More intense, more frequent, and longer lasting heat waves in the 21st century, Science 305 (5686) (2004) 994–997.

[26] P. A. Mirzaei, F. Haghighat, Approaches to study urban heat island–abilities and limitations, Building and environment 45 (10) (2010) 2192–2201.

[27] C. Georgakis, M. Santamouris, Determination of the surface and canopy urban heat island in athens central zone using advanced monitoring, Climate 5 (4) (2017) 97.

[28] T. R. Oke, City size and the urban heat island, Atmospheric Environment (1967) 7 (8) (1973) 769–779.

[29] T. R. Oke, Canyon geometry and the nocturnal urban heat island: comparison of scale model and field observations, Journal of climatology 1 (3) (1981) 237–254.

[30] K. Gobakis, D. Kolokotsa, A. Synnefa, M. Saliari, K. Giannopoulou, M. Santamouris, Development of a model for urban heat island prediction using neural network techniques, Sustainable Cities and Society 1 (2) (2011) 104–115.

[31] S. Sherafatia, M. Saradjian, S. Niazmardi, Urban heat island growth modeling using artificial neural networks and support vector regression: a case study of tehran, iran, International Archives of the Photogrammetry, Remote Sensing and Spatial Information Sciences 1 (2013) W3.

[32] Y. Toparlar, B. Blocken, B. Maiheu, G. Van Heijst, A review on the cfd analysis of urban microclimate, Renewable and Sustainable Energy Reviews 80 (2017) 1613–1640.

[33] Roughness layer surface layer, Available online: `https://slideplayer.com/slide/5002878/` (accessed on 01/05/2021).

[34] E. J. Gago, J. Roldan, R. Pacheco-Torres, J. Ordóñez, The city and urban heat islands: A review of strategies to mitigate adverse effects, Renewable and Sustainable Energy Reviews 25 (2013) 749–758.

[35] T. R. Oke, The distinction between canopy and boundary-layer urban heat islands, Atmosphere 14 (4) (1976) 268–277.

[36] X. Liu, X.-X. Li, S. Harshan, M. Roth, E. Velasco, Evaluation of an urban canopy model in a tropical city: the role of tree evapotranspiration, Environmental Research Letters 12 (9) (2017) 094008.

[37] S. S. Pillai, R. Yoshie, Flow velocity and surface temperature effects on convective heat transfer coefficient from urban canopy surfaces by numerical simulation, Journal of Urban and Environmental Engineering 7 (1) (2013) 74–81.

[38] S. S. Pillai, R. Yoshie, Experimental and numerical studies on convective heat transfer from various urban canopy configurations, Journal of wind engineering and industrial aerodynamics 104 (2012) 447–454.

[39] Y. Qu, M. Milliez, L. Musson-Genon, B. Carissimo, Numerical study of the thermal effects of buildings on low-speed airflow taking into account 3d atmospheric radiation in urban canopy, Journal of Wind Engineering and Industrial Aerodynamics 104 (2012) 474–483.

[40] H. Kusaka, F. Kimura, Thermal effects of urban canyon structure on the nocturnal heat island: Numerical experiment using a mesoscale model coupled with an urban canopy model, Journal of applied meteorology 43 (12) (2004) 1899–1910.

[41] J. F. Barlow, Progress in observing and modelling the urban boundary layer, Urban Climate 10 (2014) 216–240.

[42] T. Ichinose, F. Matsumoto, K. Kataoka, Counteracting urban heat islands in japan, in: Urban Energy Transition, Elsevier, 2008, pp. 365–380.

[43] G. Zhang, B.-J. He, Z. Zhu, B. J. Dewancker, Impact of morphological characteristics of green roofs on pedestrian cooling in subtropical climates, International journal of environmental research and public health 16 (2) (2019) 179.

[44] M. Santamouris, L. Ding, F. Fiorito, P. F. Oldfield, P. Osmond, R. Paolini, D. Prasad, A. Synnefa, Passive and active cooling for the outdoor built environment, Solar Energy 154 (2017).

[45] C. Yu, W. N. Hien, Thermal benefits of city parks, Energy and buildings 38 (2) (2006) 105–120.

[46] N. H. Wong, C. Yu, Study of green areas and urban heat island in a tropical city, Habitat international 29 (3) (2005) 547–558.

[47] D. E. Bowler, L. Buyung-Ali, T. M. Knight, A. S. Pullin, Urban greening to cool towns and cities: A systematic review of the empirical evidence, Landscape and urban planning 97 (3) (2010) 147–155.

[48] L. Malys, M. Musy, C. Inard, Direct and indirect impacts of vegetation on building comfort: A comparative study of lawns, green walls and green roofs, Energies 9 (1) (2016) 32.

[49] F. Aram, E. Solgi, E. Higueras García, A. Mosavi, A. R Várkonyi-Kóczy, The cooling effect of large-scale urban parks on surrounding area thermal comfort, Energies 12 (20) (2019) 3904.

[50] A. Dimoudi, M. Nikolopoulou, Vegetation in the urban environment: microclimatic analysis and benefits, Energy and buildings 35 (1) (2003) 69–76.

[51] L. Shashua-Bar, O. Potchter, A. Bitan, D. Boltansky, Y. Yaakov, Microclimate modelling of street tree species effects within the varied urban morphology in the mediterranean city of tel aviv, israel, International Journal of Climatology: A Journal of the Royal Meteorological Society 30 (1) (2010) 44–57.

[52] G. Lobaccaro, J. A. Acero, Comparative analysis of green actions to improve outdoor thermal comfort inside typical urban street canyons, Urban Climate 14 (2015) 251–267.

[53] S. Sodoudi, P. Shahmohamadi, K. Vollack, U. Cubasch, A. Che-Ani, Mitigating the urban heat island effect in megacity tehran, Advances in Meteorology 2014 (2014).

[54] Y. Wang, H. Akbari, The effects of street tree planting on urban heat island mitigation in montreal, Sustainable Cities and Society 27 (2016) 122–128.

[55] Z. Wu, L. Chen, Optimizing the spatial arrangement of trees in residential neighborhoods for better cooling effects: Integrating modeling with in-situ measurements, Landscape and Urban Planning 167 (2017) 463–472.

[56] H. Poptani, A. Bandyopadhyay, Extensive green roofs: Potential for thermal and energy benefits in buildings in central india, in: 30th Int. PLEA Conf., 2014, pp. 1–8.

[57] D. Li, E. Bou-Zeid, M. Oppenheimer, The effectiveness of cool and green roofs as urban heat island mitigation strategies, Environmental Research Letters 9 (5) (2014) 055002.

[58] C. Y. Jim, Thermal performance of climber greenwalls: Effects of solar irradiance and orientation, Applied energy 154 (2015) 631–643.

[59] J.-M. Huang, R. Ooka, A. Okada, T. Omori, H. Huang, The effects of urban heat island mitigation strategies on the outdoor thermal environment in central tokyo–anumerical simulation–, Wind Engineering (2009).

[60] H. Chen, R. Ooka, H. Huang, T. Tsuchiya, Study on mitigation measures for outdoor thermal environment on present urban blocks in tokyo using coupled simulation, Building and Environment 44 (11) (2009) 2290–2299.

[61] K. K. Liu, A. Baskaran, Using garden roof systems to achieve sustainable building envelopes, Citeseer, 2005.

[62] H. Lin, Y. Xiao, F. Musso, Y. Lu, Green façade effects on thermal environment in transitional space: Field measurement studies and computational fluid dynamics simulations, Sustainability 11 (20) (2019) 5691.

[63] S. Tsoka, K. Tsikaloudaki, T. Theodosiou, D. Bikas, Urban warming and cities' microclimates: Investigation methods and mitigation strategies—a review, Energies 13 (6) (2020) 1414.

[64] M. Srivanit, K. Hokao, Evaluating the cooling effects of greening for improving the outdoor thermal environment at an institutional campus in the summer, Building and environment 66 (2013) 158–172.

[65] S. S. Alcazar, F. Olivieri, J. Neila, Green roofs: Experimental and analytical study of its potential for urban microclimate regulation in mediterranean–continental climates, Urban Climate 17 (2016) 304–317.

[66] C. Yu, W. N. Hien, Thermal impact of strategic landscaping in cities: A review, Advances in Building Energy Research 3 (1) (2009) 237–260.

[67] A. Niachou, K. Papakonstantinou, M. Santamouris, A. Tsangrassoulis, G. Mihalakakou, Analysis of the green roof thermal properties and investigation of its energy performance, Energy and buildings 33 (7) (2001) 719–729.

[68] W. Pompeii, Assessing urban heat island mitigation using green roofs: a hard ware scale modeling approach, Shippensburg University (2010).

[69] J. Wu, Research on the impact of green roofing on building energy conservation and urban ecological environment (2007).

[70] T. Susca, S. R. Gaffin, G. Dell'Osso, Positive effects of vegetation: Urban heat island and green roofs, Environmental pollution 159 (8-9) (2011) 2119–2126.

[71] B. Bass, R. Stull, S. Krayenjoff, A. Martilli, Modelling the impact of green roof infrastructure on the urban heat island in toronto, Green Roofs Infrastruct. Monit 4 (1) (2002) 2–3.

[72] A. Meek, N. Jayasuriya, E. Horan, R. Adams, Environmental benefits of retrofitting green roofs to a city block, Journal of Hydrologic Engineering 20 (4) (2015) 05014020.

[73] D. Chen, X. Wang, M. Thatcher, G. Barnett, A. Kachenko, R. Prince, Urban vegetation for reducing heat related mortality, Environmental pollution 192 (2014) 275–284.

[74] A. Sharma, P. Conry, H. Fernando, A. F. Hamlet, J. Hellmann, F. Chen, Green and cool roofs to mitigate urban heat island effects in the chicago metropolitan area: Evaluation with a regional climate model, Environmental Research Letters 11 (6) (2016) 064004.

[75] T. Zölch, J. Maderspacher, C. Wamsler, S. Pauleit, Using green infrastructure for urban climate-proofing: An evaluation of heat mitigation measures at the micro-scale, Urban Forestry & Urban Greening 20 (2016) 305–316.

[76] Y. Wang, U. Berardi, H. Akbari, Comparing the effects of urban heat island mitigation strategies for toronto, canada, Energy and Buildings 114 (2016) 2–19.

[77] C. Huynh, R. Eckert, Reducing heat and improving thermal comfort through urban design-a case study in ho chi minh city, International Journal of Environmental Science and Development 3 (5) (2012) 480.

[78] A. Maleki, A. Mahdavi, Evaluation of urban heat islands mitigation strategies using 3dimentional urban micro-climate model envi-met (2016).

[79] A. Synnefa, A. Dandou, M. Santamouris, M. Tombrou, N. Soulakellis, On the use of cool materials as a heat island mitigation strategy, Journal of Applied Meteorology and Climatology 47 (11) (2008) 2846–2856.

[80] C. Georgakis, S. Zoras, M. Santamouris, Studying the effect of "cool" coatings in street urban canyons and its potential as a heat island mitigation technique, Sustainable Cities and Society 13 (2014) 20–31.

[81] S. Zoras, A. Tsermentselis, P. Kosmopoulos, A. Dimoudi, Evaluation of the application of cool materials in urban spaces: A case study in the center of florina, Sustainable Cities and Society 13 (2014) 223–229.

[82] G. Kyriakodis, M. Santamouris, Using reflective pavements to mitigate urban heat island in warm climates-results from a large scale urban mitigation project, Urban Climate 24 (2018) 326–339.

[83] P. Gandhidasan, Simplified model for the behaviour of a roof-spray cooling system, Applied Energy 34 (1) (1989) 69–77.

[84] S. Jain, K. Rao, Experimental study on the effect of roof spray cooling on unconditioned and conditioned buildings, Building Science 9 (1) (1974) 9–16.

[85] A. Urano, T. Ichinose, K. Hanaki, Thermal environment simulation for three dimensional replacement of urban activity, Journal of Wind Engineering and Industrial Aerodynamics 81 (1-3) (1999) 197–210.

[86] R. A. Memon, D. Y. Leung, C.-H. Liu, Effects of building aspect ratio and wind speed on air temperatures in urban-like street canyons, Building and Environment 45 (1) (2010) 176–188.

[87] Y. Hu, M. White, W. Ding, An urban form experiment on urban heat island effect in high density area, Procedia Engineering 169 (2016) 166–174.

[88] J.-J. Kim, J.-J. Baik, A numerical study of thermal effects on flow and pollutant dispersion in urban street canyons, Journal of applied meteorology 38 (9) (1999) 1249–1261.

[89] J. Seinfeld, S. Pandis, Atmospheric chemistry and physics. 1997, New York (2008).

[90] J.-J. Baik, Y.-S. Kang, J.-J. Kim, Modeling reactive pollutant dispersion in an urban street canyon, Atmospheric Environment 41 (5) (2007) 934–949.

[91] J. Baker, H. L. Walker, X. Cai, A study of the dispersion and transport of reactive pollutants in and above street canyons—a large eddy simulation, Atmospheric Environment 38 (39) (2004) 6883–6892.

[92] M. Moradpour, H. Afshin, B. Farhanieh, A numerical investigation of reactive air pollutant dispersion in urban street canyons with tree planting, Atmospheric Pollution Research 8 (2) (2017) 253–266.

[93] M. Moradpour, H. Afshin, B. Farhanieh, A numerical study of reactive pollutant dispersion in street canyons with green roofs, in: Building Simulation, Vol. 11, Springer, 2018, pp. 125–138.

[94] S. Kotake, T. Sano, Simulation model of air pollution in complex terrains including streets and buildings, Atmospheric Environment (1967) 15 (6) (1981) 1001–1009.

[95] S.-J. Park, W. Choi, J.-J. Kim, M. J. Kim, R. J. Park, K.-S. Han, G. Kang, Effects of building–roof cooling on the flow and dispersion of reactive pollutants in an idealized urban street canyon, Building and Environment 109 (2016) 175–189.

[96] P. Ouro, B. Fraga, N. Viti, A. Angeloudis, T. Stoesser, C. Gualtieri, Instantaneous transport of a passive scalar in a turbulent separated flow, Environmental Fluid Mechanics 18 (2) (2018) 487–513.

[97] A. Angeloudis, T. Stoesser, D. Kim, R. A. Falconer, Modelling of flow, transport and disinfection kinetics in contact tanks, in: Proceedings of the Institution of Civil Engineers-Water Management, Vol. 167, Thomas Telford Ltd, 2014, pp. 532–546.

[98] C. Gualtieri, Rans-based simulation of transverse turbulent mixing in a 2d geometry, Environmental Fluid Mechanics 10 (1-2) (2010) 137–156.

[99] W. B. Rauen, A. Angeloudis, R. A. Falconer, Appraisal of chlorine contact tank modelling practices, Water research 46 (18) (2012) 5834–5847.

[100] J. Zhang, A. E. Tejada-Martínez, Q. Zhang, Developments in computational fluid dynamics-based modeling for disinfection technologies over the last two decades: a review, Environmental Modelling & Software 58 (2014) 71–85.

[101] J.-J. Baik, K.-H. Kwak, S.-B. Park, Y.-H. Ryu, Effects of building roof greening on air quality in street canyons, Atmospheric Environment 61 (2012) 48–55.

[102] J.-J. Baik, J.-J. Kim, H. J. Fernando, A cfd model for simulating urban flow and dispersion, Journal of Applied Meteorology 42 (11) (2003) 1636–1648.

[103] K. Abhijith, P. Kumar, J. Gallagher, A. McNabola, R. Baldauf, F. Pilla, B. Broderick, S. Di Sabatino, B. Pulvirenti, Air pollution abatement performances of green infrastructure in open road and built-up street canyon environments–a review, Atmospheric Environment 162 (2017) 71–86.

[104] Z. Li, T. Ming, S. Liu, C. Peng, R. de Richter, W. Li, H. Zhang, C.-Y. Wen, Review on pollutant dispersion in urban areas-part a: Effects of mechanical factors and urban morphology, Building and Environment (2020) 107534.

[105] S. Janhäll, Review on urban vegetation and particle air pollution–deposition and dispersion, Atmospheric environment 105 (2015) 130–137.

[106] B. De Maerschalck, B. Maiheu, S. Janssen, J. Vankerkom, Cfd-modelling of complex plant-atmosphere interactions: Direct and indirect effects on local turbulence, in: Proceedings of the CLIMAQS Workshop 'Local Air Quality and its Interactions with Vegetation', Antwerp, Belgium, 2010, pp. 21–22.

[107] J. Salmond, D. Williams, G. Laing, S. Kingham, K. Dirks, I. Longley, G. Henshaw, The influence of vegetation on the horizontal and vertical distribution of pollutants in a street canyon, Science of the total environment 443 (2013) 287–298.

[108] B. future team, The best trees to reduce air pollution, Available online: `https://www.bbc.com/future/article/20200504-which-trees-reduce-air-pollution-best` (accessed on 01/06/2021). (2019).

[109] P. E. Vos, B. Maiheu, J. Vankerkom, S. Janssen, Improving local air quality in cities: to tree or not to tree?, Environmental pollution 183 (2013) 113–122.

[110] A. Wania, M. Bruse, N. Blond, C. Weber, Analysing the influence of different street vegetation on traffic-induced particle dispersion using microscale simulations, Journal of environmental management 94 (1) (2012) 91–101.

[111] W. N. Hien, M. Ignatius, A. Eliza, S. K. Jusuf, R. Samsudin, Comparison of steve and envi-met as temperature prediction models for singapore context, International Journal of Sustainable Building Technology and Urban Development 3 (3) (2012) 197–209.

[112] Y. Ayyad, S. Sharples, Envi-met validation and sensitivity analysis using field measurements in a hot arid climate, in: IOP Conference Series: Earth and Environmental Science, Vol. 329, IOP Publishing, 2019, p. 012040.

[113] B. Blocken, Computational fluid dynamics for urban physics: Importance, scales, possibilities, limitations and ten tips and tricks towards accurate and reliable simulations, Building and Environment 91 (2015) 219–245.

[114] N. Dunnett, N. Kingsbury, et al., Planting green roofs and living walls, Timber press Portland, OR, 2008.

[115] A. B. Besir, E. Cuce, Green roofs and facades: A comprehensive review, Renewable and Sustainable Energy Reviews 82 (2018) 915–939.

[116] G. Perez, L. Rincon, A. Vila, J. M. Gonzalez, L. F. Cabeza, Green vertical systems for buildings as passive systems for energy savings, Applied energy 88 (12) (2011) 4854–4859.

[117] B. Raji, M. J. Tenpierik, A. van den Dobbelsteen, The impact of greening systems on building energy performance: A literature review, Renewable and Sustainable Energy Reviews 45 (2015) 610–623.

[118] M. Manso, I. Teotónio, C. M. Silva, C. O. Cruz, Green roof and green wall benefits and costs: A review of the quantitative evidence, Renewable and Sustainable Energy Reviews 135 (2021) 110111.

[119] N. H. Wong, A. Y. K. Tan, Y. Chen, K. Sekar, P. Y. Tan, D. Chan, K. Chiang, N. C. Wong, Thermal evaluation of vertical greenery systems for building walls, Building and environment 45 (3) (2010) 663–672.

[120] T. Safikhani, A. M. Abdullah, D. R. Ossen, M. Baharvand, A review of energy characteristic of vertical greenery systems, Renewable and Sustainable Energy Reviews 40 (2014) 450–462.

[121] U. Berardi, A. GhaffarianHoseini, A. GhaffarianHoseini, State-of-the-art analysis of the environmental benefits of green roofs, Applied energy 115 (2014) 411–428.

[122] J. Yang, Q. Yu, P. Gong, Quantifying air pollution removal by green roofs in chicago, Atmospheric environment 42 (31) (2008) 7266–7273.

[123] T. Theodosiou, Green roofs in buildings: Thermal and environmental behaviour, Advances in building energy research 3 (1) (2009) 271–288.

[124] H. Qin, B. Hong, R. Jiang, Are green walls better options than green roofs for mitigating pm10 pollution? cfd simulations in urban street canyons, Sustainability 10 (8) (2018) 2833.

[125] M. Manso, J. Castro-Gomes, Green wall systems: A review of their characteristics, Renewable and sustainable energy reviews 41 (2015) 863–871.

[126] M. Weinmaster, Are green walls as "green" as they look? an introduction to the various technologies and ecological benefits of green walls, Journal of Green Building 4 (4) (2009) 3–18.

[127] T. Stathopoulos, Pedestrian level winds and outdoor human comfort, Journal of wind engineering and industrial aerodynamics 94 (11) (2006) 769–780.

[128] T. van Druenen, T. Van Hooff, H. Montazeri, B. Blocken, Cfd evaluation of building geometry modifications to reduce pedestrian-level wind speed, Building and Environment 163 (2019) 106293.

[129] B. Blocken, T. Stathopoulos, J. Van Beeck, Pedestrian-level wind conditions around buildings: Review of wind-tunnel and cfd techniques and their accuracy for wind comfort assessment, Building and Environment 100 (2016) 50–81.

[130] B. Blocken, T. Stathopoulos, Cfd simulation of pedestrian-level wind conditions around buildings: Past achievements and prospects, Journal of Wind Engineering and Industrial Aerodynamics 121 (2013) 138–145.

[131] S. Murakami, R. Ooka, A. Mochida, S. Yoshida, S. Kim, Cfd analysis of wind climate from human scale to urban scale, Journal of Wind Engineering and Industrial Aerodynamics 81 (1-3) (1999) 57–81.

[132] A. Mochida, I. Y. Lun, Prediction of wind environment and thermal comfort at pedestrian level in urban area, Journal of wind engineering and industrial aerodynamics 96 (10-11) (2008) 1498–1527.

[133] T. Stathopoulos, Computational wind engineering: Past achievements and future challenges, Journal of Wind Engineering and Industrial Aerodynamics 67 (1997) 509–532.

[134] B. Blocken, 50 years of computational wind engineering: past, present and future, Journal of Wind Engineering and Industrial Aerodynamics 129 (2014) 69–102.

[135] B. Blocken, Les over rans in building simulation for outdoor and indoor applications: a foregone conclusion?, in: Building Simulation, Vol. 11, Springer, 2018, pp. 821–870.

[136] J. Franke, C. Hirsch, A. Jensen, H. Krüs, M. Schatzmann, P. Westbury, S. Miles, J. Wisse, N. Wright, Recommendations on the use of cfd in wind engineering: Jpaj van beeck, in: Proc. Int. Conf. Urban Wind Engineering and Building Aerodynamics. COST Action C, Vol. 14.

[137] J.-W. Wang, H.-J. Yang, J.-J. Kim, Wind speed estimation in urban areas based on the relationships between background wind speeds and morphological parameters, Journal of Wind Engineering and Industrial Aerodynamics 205 (2020) 104324.

[138] C. A. Arkon, Ü. Özkol, Effect of urban geometry on pedestrian-level wind velocity, Architectural Science Review 57 (1) (2014) 4–19.

[139] H. Mittal, A. Sharma, A. Gairola, A review on the study of urban wind at the pedestrian level around buildings, Journal of Building Engineering 18 (2018) 154–163.

[140] R. team, Wind effects and tall buildings guidelines and best practice for assessing wind effects and tall buildings in the city of london, Available online: https://www.cityoflondon.gov.uk/services/environment-and-

planning/planning/design/Documents/wind-and-tall-buildings-pan (accessed on 01/07/2021).

[141] M. H. Salim, K. H. Schlünzen, D. Grawe, Including trees in the numerical simulations of the wind flow in urban areas: should we care?, Journal of Wind Engineering and Industrial Aerodynamics 144 (2015) 84–95.

[142] windtech consults, 20 seriously effective wind mitigation strategies for your next project, Available online: https://windtechconsult.com/20-seriously-effective-wind-mitigation-strategies-for-your-next-project/ (accessed on 01/06/2021). (2019).

[143] T. Rofail, Developing habitable wind environment, CTBUH 2008 8th World Conference (2008).

[144] K. M. Lam, Wind environment around the base of a tall building with a permeable intermediate floor, Journal of Wind Engineering and Industrial Aerodynamics (1992) 2313.

[145] Y. Uematsu, M. Yamada, H. Higashiyama, T. Orimo, Effects of the corner shape of high-rise buildings on the pedestrian-level wind environment with consideration for mean and fluctuating wind speeds, Journal of Wind Engineering and Industrial Aerodynamics 44 (1-3) (1992) 2289–2300.

[146] T. Stathopoulos, R. Storms, Wind environmental conditions in passages between buildings, Journal of Wind Engineering and Industrial Aerodynamics 24 (1) (1986) 19–31.

[147] F. Kardan, O. Baverel, F. P. Agel, Assessment of rans turbulence models in urban environments: Cfd simulation of airflow around idealized high-rise morphologies, in: Humanizing Digital Reality, Springer, 2018, pp. 259–269.

[148] A. Ricci, I. Kalkman, B. Blocken, M. Burlando, M. Repetto, Impact of turbulence models and roughness height in 3d steady rans simulations of wind flow in an urban environment, Building and Environment 171 (2020) 106617.

[149] M. Auvinen, S. Boi, A. Hellsten, T. Tanhuanpää, L. Järvi, Study of realistic urban boundary layer turbulence with high-resolution large-eddy simulation, Atmosphere 11 (2) (2020) 201.

[150] O. Reynolds, On the dynamical theory of incompressible viscous fluids and the determination of the criterion, cambridge phil, Trans 123–164.

[151] C. adapco team, STARCCM+ - CFD Toolbox - User's Guide, Available online: `http://www.cd-adapco.com/` (accessed on 01/01/2019). (2019).

[152] B. E. Launder, D. B. Spalding, The numerical computation of turbulent flows, in: Numerical prediction of flow, heat transfer, turbulence and combustion, Elsevier, 1983, pp. 96–116.

[153] T.-H. Shih, W. W. Liou, A. Shabbir, Z. Yang, J. Zhu, A new k-ε eddy viscosity model for high reynolds number turbulent flows, Computers & fluids 24 (3) (1995) 227–238.

[154] F. R. Menter, Two-equation eddy-viscosity turbulence models for engineering applications, AIAA journal 32 (8) (1994) 1598–1605.

[155] J. Franke, A. Hellsten, K. Schlünzen, B. Carissimo, Best practice guideline for the cfd simulation of flows in the urban environment-a summary, in: 11th Conference on Harmonisation within Atmospheric Dispersion Modelling for Regulatory Purposes, Cambridge, UK, July 2007, Cambridge Environmental Research Consultants, 2007.

[156] D. Lakehal, W. Rodi, Calculation of the flow past a surface-mounted cube with two-layer turbulence models, Journal of Wind Engineering and Industrial Aerodynamics 67 (1997) 65–78.

[157] W. Reynolds, Fundamentals of turbulence for turbulence modeling and simulation, Tech. rep., Stanford Univ CA Dept of Mechanical Engineering (1987).

[158] D. C. Wilcox, et al., Turbulence modeling for CFD, Vol. 2, DCW industries La Canada, CA, 1998.

[159] D. C. Wilcox, Formulation of the k ω turbulence model revisited, AIAA journal 46 (11) (2008) 2823–2838.

[160] D. C. Wilcox, Reassessment of the scale-determining equation for advanced turbulence models, AIAA journal 26 (11) (1988) 1299–1310.

[161] P. Moin, K. Mahesh, Direct numerical simulation: a tool in turbulence research, Annual review of fluid mechanics 30 (1) (1998) 539–578.

[162] E. Zheng, M. Rudman, J. Singh, S. Kuang, Direct numerical simulation of turbulent non-newtonian flow using openfoam, Applied Mathematical Modelling 72 (2019) 50–67.

[163] C.-H. Moeng, P. P. Sullivan, Large-eddy simulation, Encyclopedia of atmospheric sciences 1140 (2002) 1150.

[164] A. Abba, A. Cercignani, L. Valdettaro, Analysis of subgrid scale models, Computers & Mathematics with Applications 46 (4) (2003) 521–535.

[165] J.-L. Guermond, J. T. Oden, S. Prudhomme, Mathematical perspectives on large eddy simulation models for turbulent flows, Journal of Mathematical Fluid Mechanics 6 (2) (2004) 194–248.

[166] C. Moeng, P. Sullivan, Large eddy simulation. encyclopedia of atmospheric sciences 2nd edition, eds. g. north, f. zhang and j. pyle (2011).

[167] Y. Zhiyin, Large-eddy simulation: Past, present and the future, Chinese journal of Aeronautics 28 (1) (2015) 11–24.

[168] D. D. Qi, L. L. Wang, R. Zmeureanu, Large eddy simulation of thermal comfort and energy utilization indices for indoor airflows., Ashrae Transactions 119 (2) (2013).

[169] J. Liu, J. Niu, Cfd simulation of the wind environment around an isolated high-rise building: An evaluation of srans, les and des models, Building and Environment 96 (2016) 91–106.

[170] J. Liu, J. Niu, Y. Du, C. Mak, Large eddy simulation on the pedestrian level wind around a building community: Evaluation of influencing factors, in: Proceedings of the 4th International Conference on Building Energy, Environment, Melbourne, Australia, 2018, pp. 5–9.

[171] V. Rodrigues, I. Calmet, M. Francis, D. Maro, D. Hébert, O. Connan, P. Laguionie, M. Maché, T. Piquet, P. Kéravec, et al., Large-eddy simulation of flow and dispersion in an heterogeneous urban area: comparison with field data, in: 15th International Conference on Harmonisation within Atmospheric Dispersion Modelling for Regulatory Purposes HARMO, 2013, pp. 6–9.

[172] W. Wang, Y. Xu, E. Ng, Large-eddy simulations of pedestrian-level ventilation for assessing a satellite-based approach to urban geometry generation, Graphical Models 95 (2018) 29–41.

[173] V. Masson, A physically-based scheme for the urban energy budget in atmospheric models, Boundary-layer meteorology 94 (3) (2000) 357–397.

[174] H. Kondo, Y. Genchi, Y. Kikegawa, Y. Ohashi, H. Yoshikado, H. Komiyama, Development of a multi-layer urban canopy model for the analysis of energy consumption in a big city: Structure of the urban canopy model and its basic performance, Boundary-Layer Meteorology 116 (3) (2005) 395–421.

[175] T. R. Oke, Boundary layer climates, Routledge, 2002.

[176] D. Sailor, Energy buildings and urban environment, in: Climate Vulnerability: Understanding and Addressing Threats to Essential Resources, Elsevier Inc., 2013, pp. 167–182.

[177] P. Shahmohamadi, A. Che-Ani, K. Maulud, N. Tawil, N. Abdullah, The impact of anthropogenic heat on formation of urban heat island and energy consumption balance, Urban Studies Research 2011 (2011).

[178] C. Grimmond, The suburban energy balance: Methodological considerations and results for a mid-latitude west coast city under winter and spring conditions, International Journal of Climatology 12 (5) (1992) 481–497.

[179] J.-J. Kim, J.-J. Baik, Urban street-canyon flows with bottom heating, Atmospheric Environment 35 (20) (2001) 3395–3404.

[180] C. Gromke, B. Blocken, W. Janssen, B. Merema, T. van Hooff, H. Timmermans, Cfd analysis of transpirational cooling by vegetation: Case study for specific meteorological conditions during a heat wave in arnhem, netherlands, Building and environment 83 (2015) 11–26.

[181] S. Green, Modeling turbulent air flow in a stand of widely spaced trees, PHOENICS Journal Computational Fluid Dynamics and its Applications 5 (1992) 294–312.

[182] J. Liu, J. Chen, T. Black, M. Novak, E-ε modelling of turbulent air flow downwind of a model forest edge, Boundary-layer meteorology 77 (1) (1996) 21–44.

[183] C. Sanz, A note on k-ε modelling of vegetation canopy air-flows, Boundary-Layer Meteorology 108 (1) (2003) 191–197.

[184] A. P. Jeanjean, G. Hinchliffe, W. McMullan, P. S. Monks, R. J. Leigh, A cfd study on the effectiveness of trees to disperse road traffic emissions at a city scale, Atmospheric Environment 120 (2015) 1–14.

[185] G. G. Katul, L. Mahrt, D. Poggi, C. Sanz, One-and two-equation models for canopy turbulence, Boundary-layer meteorology 113 (1) (2004) 81–109.

[186] C. Gromke, R. Buccolieri, S. Di Sabatino, B. Ruck, Dispersion study in a street canyon with tree planting by means of wind tunnel and numerical investigations–evaluation of cfd data with experimental data, Atmospheric Environment 42 (37) (2008) 8640–8650.

[187] J.-J. Kim, J.-J. Baik, A numerical study of the effects of ambient wind direction on flow and dispersion in urban street canyons using the rng k–ε turbulence model, Atmospheric Environment 38 (19) (2004) 3039–3048.

[188] A. P. Jeanjean, R. Buccolieri, J. Eddy, P. S. Monks, R. J. Leigh, Air quality affected by trees in real street canyons: The case of marylebone neighbourhood in central london, Urban Forestry & Urban Greening 22 (2017) 41–53.

[189] G. Jiang, T. Hu, H. Yang, Effects of ground heating on ventilation and pollutant transport in three-dimensional urban street canyons with unit aspect ratio, Atmosphere 10 (5) (2019) 286.

[190] J. Mattai, D. Hutchinson, G. L. Authority, London atmospheric emissions inventory.

[191] B. Blocken, J. Carmeliet, T. Stathopoulos, Cfd evaluation of wind speed conditions in passages between parallel buildings—effect of wall-function roughness modifications for the atmospheric boundary layer flow, Journal of Wind Engineering and Industrial Aerodynamics 95 (9-11) (2007) 941–962.

[192] Y. Tominaga, A. Mochida, R. Yoshie, H. Kataoka, T. Nozu, M. Yoshikawa, T. Shirasawa, Aij guidelines for practical applications of cfd to pedestrian wind environment around buildings, Journal of wind engineering and industrial aerodynamics 96 (10-11) (2008) 1749–1761.

[193] A. Parente, C. Benocci, On the rans simulation of neutral abl flows, in: Proceedings of the Fifth International Symposium on Computational Wind Engineering (CWE2010) Chapel Hill, North Carolina, USA, May, 2010, pp. 23–27.

[194] W. Yang, Y. Quan, X. Jin, Y. Tamura, M. Gu, Influences of equilibrium atmosphere boundary layer and turbulence parameter on wind loads of low-rise buildings, Journal of wind engineering and industrial aerodynamics 96 (10-11) (2008) 2080–2092.

[195] P. Jackson, On the displacement height in the logarithmic velocity profile, Journal of fluid mechanics 111 (1981) 15–25.

[196] K. Takeda, On roughness length and zero-plane displacement in the wind profile of the lowest air layer, Journal of the Meteorological Society of Japan. Ser. II 44 (2) (1966) 101–108.

[197] Z. Dong, S. Gao, D. W. Fryrear, Drag coefficients, roughness length and zero-plane displacement height as disturbed by artificial standing vegetation, Journal of Arid Environments 49 (3) (2001) 485–505.

[198] P. Richards, R. Hoxey, Appropriate boundary conditions for computational wind engineering models using the k-ε turbulence model, in: Computational Wind Engineering 1, Elsevier, 1993, pp. 145–153.

[199] S. E. Nicholson, A pollution model for street-level air, Atmospheric Environment (1967) 9 (1) (1975) 19–31.

[200] J. Wieringa, Updating the davenport roughness classification, Journal of Wind Engineering and Industrial Aerodynamics 41 (1-3) (1992) 357–368.

[201] R. Pielke, H. Panofsky, Turbulence characteristics along several towers, Boundary-Layer Meteorology 1 (2) (1970) 115–130.

[202] M. Sosnowski, J. Krzywanski, K. Grabowska, R. Gnatowska, Polyhedral meshing in numerical analysis of conjugate heat transfer, in: EPJ Web of Conferences, Vol. 180, EDP Sciences, 2018, p. 02096.

[203] Y. Tominaga, Flow around a high-rise building using steady and unsteady rans cfd: Effect of large-scale fluctuations on the velocity statistics, Journal of Wind Engineering and Industrial Aerodynamics 142 (2015) 93–103.

[204] J. Liu, J. Niu, Y. Du, C. Mak, Large eddy simulation on the pedestrian level wind around a building community: Evaluation of influencing factors.

[205] A. Keshmiri, O. Karim, S. Benhamadouche, Comparison of advanced rans models against large eddy simulation and experimental data in investigation of ribbed passages with heat transfer, in: Proceedings, Conference on Modelling Fluid Flow (CMFF'12) International Conference on Fluid Flow Technologies Budapest, Hungary, 2012, pp. 486–493.

[206] M. Zhang, W. Bae, J. Kim, The effects of the layouts of vegetation and wind flow in an apartment housing complex to mitigate outdoor microclimate air temperature, Sustainability 11 (11) (2019) 3081.

[207] J. Santiago, F. Martin, A. Cuerva, N. Bezdenejnykh, A. Sanz-Andrés, Experimental and numerical study of wind flow behind windbreaks, Atmospheric Environment 41 (30) (2007) 6406–6420.

[208] Y. Tominaga, T. Stathopoulos, Numerical simulation of dispersion around an isolated cubic building: model evaluation of rans and les, Building and Environment 45 (10) (2010) 2231–2239.

[209] J. Liu, J. Niu, Q. Xia, Combining measured thermal parameters and simulated wind velocity to predict outdoor thermal comfort, Building and Environment 105 (2016) 185–197.

[210] F. Dimitris, B. Catherine, T. Aris, B. Thomas, K. Constantinos, Cfd study of thermal comfort in urban area, Energy and Environmental Engineering 5 (1) (2017) 8–18.

[211] S. Hein, D. Winterhalter, G. Wilhelm, U. Kohnle, Wertholzproduktion mit der sandbirke (betula pendula roth): waldbauliche möglichkeiten und grenzen, Allgemeine Forst-und Jagdzeitung 180 (2009) 206–219.

[212] R. Buccolieri, J.-L. Santiago, E. Rivas, B. Sanchez, Review on urban tree modelling in cfd simulations: Aerodynamic, deposition and thermal effects, Urban Forestry & Urban Greening 31 (2018) 212–220.

[213] K. Uehara, S. Murakami, S. Oikawa, S. Wakamatsu, Wind tunnel experiments on how thermal stratification affects flow in and above urban street canyons, Atmospheric Environment 34 (10) (2000) 1553–1562.

[214] J.-J. Kim, J.-J. Baik, Physical experiments to investigate the effects of street bottom heating and inflow turbulence on urban street-canyon flow, Advances in atmospheric Sciences 22 (2) (2005) 230–237.

[215] X. Xie, C.-H. Liu, D. Y. Leung, Impact of building facades and ground heating on wind flow and pollutant transport in street canyons, Atmospheric Environment 41 (39) (2007) 9030–9049.

[216] A. A. Millward, M. Torchia, A. E. Laursen, L. D. Rothman, Vegetation placement for summer built surface temperature moderation in an urban microclimate, Environmental management 53 (6) (2014) 1043–1057.

[217] S. M. Salim, R. Buccolieri, A. Chan, S. Di Sabatino, S. C. Cheah, Large eddy simulation of the aerodynamic effects of trees on pollutant concentrations in street canyons, in: Urban Environmental Pollution 2010, 2011, pp. 17–24.

[218] X.-X. Li, R. E. Britter, T. Y. Koh, L. K. Norford, C.-H. Liu, D. Entekhabi, D. Y. Leung, Large-eddy simulation of flow and pollutant transport in urban street canyons with ground heating, Boundary-layer meteorology 137 (2) (2010) 187–204.

[219] W. Cheng, C.-H. Liu, Large-eddy simulation of turbulent transports in urban street canyons in different thermal stabilities, Journal of Wind Engineering and Industrial Aerodynamics 99 (4) (2011) 434–442.

[220] K. B. Schnelle, Atmospheric diffusion modeling, in: Encyclopedia of Physical Science and Technology, Elsevier, 2003, pp. 679–705. doi:10.1016/b0-12-227410-5/00036-3.
URL https://doi.org/10.1016/b0-12-227410-5/00036-3

[221] J. Fu, T. Zhang, M. Li, S. Li, X. Zhong, X. Liu, Study on flow and heat transfer characteristics of porous media in engine particulate filters based on lattice boltzmann method, Energies 12 (17) (2019) 3319.

[222] J.-J. Baik, J.-J. Kim, A numerical study of flow and pollutant dispersion characteristics in urban street canyons, Journal of applied meteorology 38 (11) (1999) 1576–1589.

[223] R. Cichowicz, G. Wielgosiński, W. Fetter, Effect of wind speed on the level of particulate matter pm10 concentration in atmospheric air during winter season in vicinity of large combustion plant, Journal of Atmospheric Chemistry 77 (2020) 35–48.

[224] A. Keshmiri, M. A. Cotton, Y. Addad, D. Laurence, Turbulence models and large eddy simulations applied to ascending mixed convection flows, Flow, turbulence and combustion 89 (3) (2012) 407–434.

[225] A. Keshmiri, Numerical sensitivity analysis of 3-and 2-dimensional rib-roughened channels, Heat and Mass Transfer 48 (7) (2012) 1257–1271.

[226] A. Keshmiri, K. Osman, S. Benhamadouche, N. Shokri, Assessment of advanced rans models against large eddy simulation and experimental data in the investigation of ribbed passages with passive heat transfer, Numerical Heat Transfer, Part B: Fundamentals 69 (2) (2016) 96–110.

Appendix A

Mesh independence test

Mesh independence has been tested for the accuracy of the results in Figure 4.6 and 4.7 using polyhedral grids with different mesh refinements. The velocity data for three different grid size were extracted from the middle of building passages for Test case 1 and across three vertical line for Test case 2. It must be noted that the results of Figure A.2 are for the standard k-ε turbulence model.

A.1 Test case 1

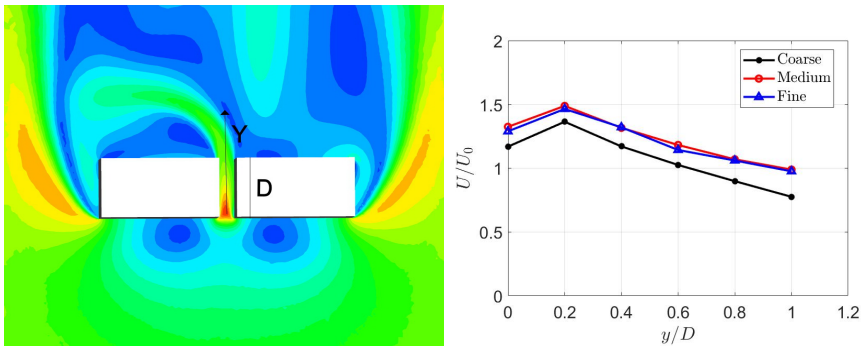

(**a**) (**b**)

Figure A.1: (**a**) Computational domain for East Village. (**b**) Wind data analysis.

A.2 Test case 2

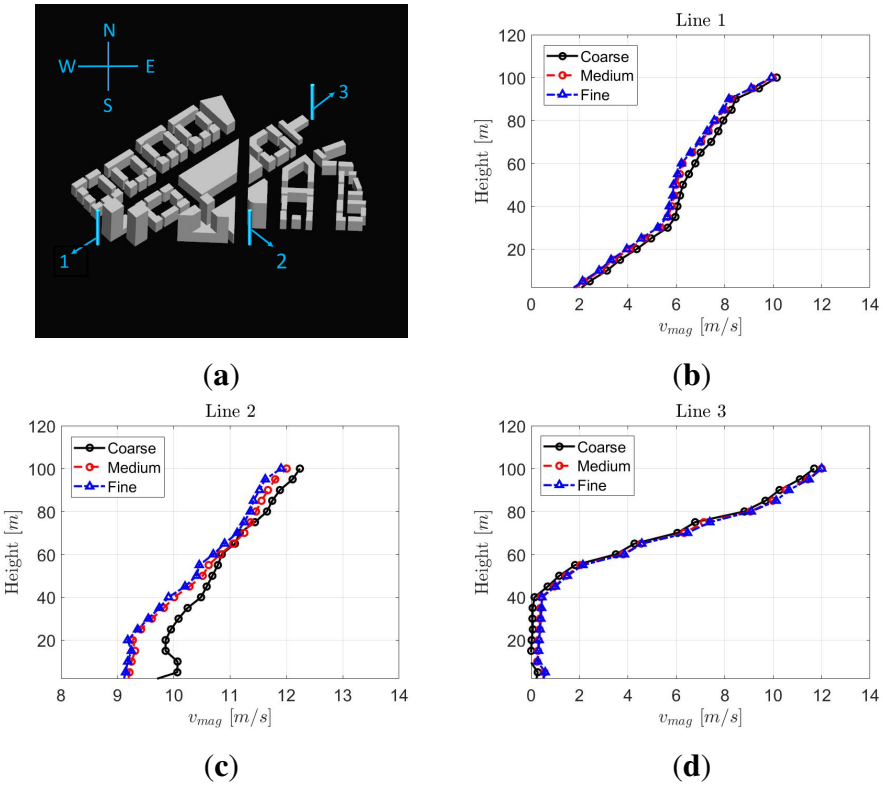

Figure A.2: Comparison of various turbulent models at different heights for 3 distinct sections of the geometry: (**b**) line 1, (**c**) line 2, (**d**) line 3.

Appendix B

Publications and presentations

Peer-reviewed

1. **A. Hosseinzadeh**, A. Keshmiri, Computational Simulation of Wind Microclimate in Complex Urban Models and Mitigation using Trees, Journal of Buildings 11(3) (2021) 112.

Conference proceedings

1. **A. Hosseinzadeh**, A. Bottacin Busolin , A. Keshmiri, Computational modelling of vegetation in urban areas and its impact on air quality, temperature and velocity, 13th ERCOFTAC symposium on engineering, turbulence, modelling and measurements conference (2021), Rhodes, Greece.

2. **A. Hosseinzadeh**, N. Shokri, A. Keshmiri, The role of turbulence modelling in simulating urban microclimate, 16th UK Heat Transfer conference, Advances in Heat Transfer and Thermal Engineering (2019), Nottingham, United Kingdom.

3. **A. Hosseinzadeh**, N. Shokri, A. Keshmiri, The role of turbulence modelling in simulating urban microclimate, MACE PGR conference (2019), Manchester, United Kingdom.